DEVELOPMENT OF CARBON-BASED NANOCOMPOSITES FOR ENERGY STORAGE AND ENVIRONMENTAL APPLICATIONS

FEI LINFENG

Ph.D

The Hong Kong Polytechnic University

2015

The Hong Kong Polytechnic University

Department of Applied Physics

Development of Carbon-based Nanocomposites for Energy Storage and Environmental Applications

FEI Linfeng

A thesis submitted in partial fulfillment of the requirements for
the degree of Doctor of Philosophy

September 2014

CERTIFICATE OF ORIGINALITY

I hereby declare that this thesis is my own work and that, to the best of my knowledge and belief, it reproduces no material previously published or written, nor material that has been accepted for the award of any other degree or diploma, except where due acknowledgement has been made in the text.

(Signed)

FEI Linfeng (Name of student)

To my dearest wife and daughter

ABSTRACT

Over the past few decades, the rapid development of various electronic and electric devices including smartphones, wearable electronics, and electric vehicles have transformed the way we live and given rise to technologies associated with energy storage. Among all energy storage devices, lithium-ion batteries have been most popular and gained much commercial success. In the configuration of a lithium-ion battery, the cathode material has far more impact than the anode, the separator, or the electrolyte on overall performance, safety, and cost of the finished battery. In order to power large-scale systems, it would be essential to develop high performance cathode materials to ensure maximum performance.

Anticipated to be one of the most promising solutions in next-generation revolutionary cathode materials for lithium-ion batteries, monoclinic $Li_3V_2(PO_4)_3$ has been frequently noted in the literature despite its low intrinsic electronic conductivity. To gain better electrochemical performance, a great deal of efforts have been made to improve its conductivity of monoclinic $Li_3V_2(PO_4)_3$ including size reduction, conductive surface coating, and lattice engineering. However, simple ways of synthesizing this electrode material with superior gravimetric/volumetric electrochemical characteristics and a robust structure has yet to be found.

In this thesis, a rational $Li_3V_2(PO_4)_3$/C composite is first engineered by making porous carbon nanoflakes highly entangled on single-crystalline $Li_3V_2(PO_4)_3$

microrods. The resulting as-synthesized composite displays a number of structural features including a hierarchical mesoporous-macroporous microstructure with ultra-high tap density. The findings of the corresponding electrochemical evaluations reveal that our designed composite show greatly improved electrochemical performances, including good cycling stability and superior rate capability, which are directly resulted from its enhanced structural stability and reduced charge-transfer resistance.

To further improve the cycling stability of the $Li_3V_2(PO_4)_3/C$ composite, we designed another novel architecture by incorporating carbon-coated $Li_3V_2(PO_4)_3$ nanospheres into a well-connected three-dimensional carbon network uniformly. Such a hierarchical porous framework combines multiple advantages including a rational mesoporous-macroporous structure to facilitate the electrolyte infiltration, a three-dimensional continuous electron pathway, and abundant porous space for accommodating volume expansion during the electrode charge/discharge. This material, as a cathode, is capable of delivering superior cycling stability with an excellent rate capability.

In addition, in pursuit of solving various energy and environmental problems, high-performance photocatalytic materials are extensively studied, especially those worked upon visible-light. In this thesis, we also described a novel nanocomposite of porous Nb_2O_5 nanofibers decorated with graphene nanoclusters on their surfaces. By utilizing such a composite, the active region of Nb_2O_5 was significantly extended from UV region to UV-Vis region and hence, the photocatalytic performance was also greatly improved. Detailed structure analysis revealed that the performance enhancement was originated from the ample existence of chemical bondings (Nb-O-C) and the unique orientation of graphene layers (perpendicular to the Nb_2O_5/C interface).

It should be noted that in the research of carbon-based composite, it has been a long-term challenge to fully understand the growth mechanism of carbon nanostructures on host particles at atomic level and in this thesis, we attempt to solve this problem by presenting one example, i.e., to document graphene growth from designed liquid-solid interface using in-situ transmission electron microscope technique coupled with a high-stable heating system. In the amorphous carbon-Pt_3Co modelling system, we discovered that the carbon first crystallized to nanoclusters at step-edges on liquid Pt_3Co surfaces before merging into graphene layers through kinetic restructuring via oriented-attachment, leading to the final formation of few-layered graphene nanostructures. The results from density-functional theory calculations further revealed that Co atoms rather than Pt atoms acted as initial nucleation centers, suggesting higher catalytic activity among transition metals than that of noble metals in this process.

LIST OF PUBLICATIONS

1. **Linfeng Fei**, Li Sun, Wei Lu, Min Guo, Haitao Huang, Jiaping Wang, Helen L. W. Chan, Shoushan Fan, Yu Wang. Stable 4 V-class Bicontinuous Cathodes by Hierarchically Porous Carbon Coating on $Li_3V_2(PO_4)_3$ Nanospheres. **Nanoscale**, 2014, 6, 12426-12433.

2. Shishun Qi,* **Linfeng Fei**,* Ruzhong Zuo, Yu Wang, Yucheng Wu. Graphene Nanocluster Decorated Niobium Oxide Nanofibers for Visible Light Photocatalytic Applications. **Journal of Materials Chemistry A**, 2014, 2, 8190-8195. (*: equal contribution)

3. **Linfeng Fei**, Tieyu Sun, Wei Lu, Xiaoqiang An, Zhuofeng Hu, Jimmy C. Yu, Renkui Zheng, Xiaomin Li, Helen L. W. Chan, Yu Wang. Direct Observation of Carbon Nanostructure Growth at Liquid-solid Interfaces. **Chemical Communications**, 2014, 50, 826-828.

4. **Linfeng Fei**, Wei Lu, Li Sun, Jiaping Wang, Jiabing Wei, Helen L. W. Chan, Yu Wang. Highly Entangled Carbon Nanoflakes on $Li_3V_2(PO_4)_3$ Microrods for Improved Lithium Storage Performance, **RSC Advances**, 2013, 3, 1297-1301.

5. **Linfeng Fei**, Yongming Hu, Xing Li, Ruobing Song, Li Sun, Haitao Huang, Haoshuang Gu, Helen L. W. Chan, Yu Wang. Electro-spun Bismuth Ferrite

Nanofibers for Potential Applications in Ferroelectric Photovoltaic Devices. **ACS Applied Materials & Interfaces** (in revising).

6. **Linfeng Fei**, Li Sun, Xiaogang Li, Wentuan Bi, Changzheng Wu, Helen L. W. Chan, Yu Wang. Strong Carbon-sulfur Binding in Graphene/sulfur nanocomposite for Improving Lithium-sulfur Batteries. Submitted.

7. Wenfei Zhang, Siu Fung Yu, **Linfeng Fei**, Limin Jin, Shusheng Pan, Peng Lin. Large-area Color Controllable Remote Carbon White-Light Light-Emitting Diodes. **Carbon**, doi:10.1016/j.carbon.2014.12.107

8. Shusheng Pan, Wei Lu, Yihua Zhao, Wei Tong, Ming Li, Limin Jin, Jin Yuk Choi, Fei Qi, Shiguo Chen, **Linfeng Fei**, Siu Fung Yu. Self-doped Rutile Titania with High Performance for Direct and Ultrafast Assay of H_2O_2. **ACS Applied Materials & Interfaces**, 2013, 5, 12784-12788.

9. Zhenjiang Shen, Yu Wang, Wanping Chen, **Linfeng Fei**, Kun Li, Helen L. W. Chan, Lina Bing. Electrospinning Preparation and High-temperature Superconductivity of $YBa_2Cu_3O_{7-x}$ Nanotubes, **Journal of Materials Science**, 2013, 48, 3985-3990.

10. Feng Feng, Shuanglin Hu, Yuqiao Guo, Jiyin Zhao, Ngai Yui Chan, **Linfeng Fei**, Wensheng Yan, Wei Ning, Jinlong Yang, Yu Wang, Yi Xie, Changzheng Wu.

Room-temperature large magnetic-dielectric coupling in new phase anatase $VTiO_4$. **Chemical Communications**, 2013, 49, 10462-10464.

11. Feng Cao, Yumin Liu, Bolei Chen, **Linfeng Fei**, Yu Wang, Jikang Yuan. Enhancement of Electrochemical Capacitive Properties Based on Complementation of Morphologies, **Electrochimica Acta**, 2012, 81, 1-7.

12. Renkui Zheng, Yu Wang, Yukuai Liu, Guanyin Gao, **Linfeng Fei**, Yong Jiang, Helen L. W. Chan, Xiaomin Li, Haosu Luo, Xiaoguang Li. Epitaxial Growth and Interface Strain Coupling Effects in Manganite Film/Piezoelectric-crystal Multiferroic Heterostructures, **Materials Chemistry and Physics**, 2012, 133, 42-46.

13. Yupeng Zhang, **Linfeng Fei**, Xudong Jiang, Chunxu Pan, Yu Wang. Engineering Nanostructured Bi_2WO_6-TiO_2 toward Effective Utilization of Natural Light in Photocatalysis, **Journal of the American Ceramic Society**, 2011, 94, 4157-4161.

14. Guanyin Gao, Yu Wang, Yong Jiang, **Linfeng Fei**, Ngai Yui Chan, Helen L. W. Chan, Wenbing Wu. Epitaxial Growth and Rectification Characteristics of Double Perovskite Oxide La_2NiMnO_6 Films on Nb-$SrTiO_3$ Single Crystal Substrates, **Thin Solid Films**, 2011, 519, 6148-6150.

ACKNOWLEDGMENTS

I would like to express my most sincere gratitude, firstly to my supervisors, Dr. Yu Wang and Prof. Helen L. W. Chan, for offering me the opportunity to conduct research in such a fascinating field, and providing me valuable guidance throughout my six years of studies in the Hong Kong Polytechnic University. I will cherish the scientific thinking and method learned from them that would accompany me in my future career life.

I would like to express my thanks to my group mates, Dr. Tieyu Sun, Dr. Li Sun, Mr. Shishun Qi, Ms. Ruobing Song, and Mr. Xing Li, for their useful help and discussion in experiments. Many thanks go to my colleagues, Dr. Wenfei Zhang, Dr. Wei Lu, Dr. Shusheng Pan, and Ms. Min Guo and the entire department for their consistent support. I would also like to express my sincere appreciation to Prof. Changzheng Wu in University of Science and Technology of China and all members in his group, who gave me lots of support and help.

Finally, I give my special appreciation to my parents, wife, and daughter for being understanding, patient, supportive and for their loves, encouragement and sacrifices along the way.

TABLE OF CONTENTS

LIST OF ABBREVIATIONS

Abbreviation	**Description**
0D	Zero Dimension(al)
2D	Two Dimension(al)
3D	Three Dimension(al)
CB	Conduction Band
CV	Cyclic Voltammetry
DFT	Density-functional Theory
DSC	Differential Scanning Calorimetry
EDS	Energy Dispersed Spectrum
EIS	Electrochemical Impedance Spectroscopy(e)
EVs	Electrical Vehicles
FFT	Fast Fourier Transform
FWHM	Full Width at Half Maximum
HAADF	High-angle Annular Dark Field
HN-LVP@C	Hierarchical Nanostructured $Li_3V_2(PO_4)_3$/Carbon
HRTEM	High Resolution Transmission Electron Microscopy(e)
ICP-OES	Inductively Coupled Plasma-Optical Emission Spectrometry
LCO	$LiCoO_2$
LFP	$LiFePO_4$
LIB(s)	Lithium Ion Battery(Batteries)
LMO	$LiMn_2O_4$
LVP	$Li_3V_2(PO_4)_3$
LVP/C	$Li_3V_2(PO_4)_3$/Carbon
MO	Methyl Orange
NFs	Nanofibers

NMC	$LiNi_{1/3}Mn_{1/3}Co_{1/3}O_2$
OA	Oriented Attachment
PEG	Polyethylene Glycol
PL	Photoluminescence
PVP	Polivinilpirrolidone
SAED	Selected Area Electron Diffraction
SEI	Solid Electrolyte Interface
SEM	Scanning Electron Microscopy(e)
STEM	Scanning Transmission Electron Microscopy(e)
TEM	Transmission Electron Microscopy(e)
TG	Thermogravimetric Analysis
UV-Vis	Ultraviolet-Visible
VB	Valence Band
XPS	X-ray Photoelectron Spectroscopy(e)
XRD	X-Ray Diffractions

CHAPTER 1 INTRODUCTION

1.1 Foreword

Energy is of great importance in the process of human civilization. The continuous consumption of fossil fuels (e.g. oil, coal, and natural gas) in the past few decades has led to a number of undesirable consequences such as global warming and environmental issues, giving to “green” energies (including solar, wind, nuclear, geothermal, and hydropower, etc.) that are renewable, clean, and cost-effective. To integrate and widen the applications of these new energies into daily life, energy storage devices are essential. So far, rechargeable (or secondary) batteries have shown to be the most efficient energy storage devices as they are capable of converting electrical energy into chemical energy, and release it in the form of electricity again. Today most advanced rechargeable battery technologies rely on lead-acid, nickel-metal hydride, lithium-ion, and redox flow cells. Among them, lithium-ion batteries (LIBs) has been most popular because of its mobility in powering all kinds of portable electronic devices (e.g. cell phones, digital cameras, notebooks, and wearable electronics) and even electrical vehicles (EVs). The primary reasons for using a LIB to power electrical vehicles originates from its high voltage, high energy density (both volumetric and gravimetric), lack of memory effect, low self-discharge, long cycling life, and environmental friendliness.

On the other hand, as fossil fuels are still, and will continue to be the primary energy source for humanity, the associated environmental problems have become a major global concern. The rapid development of industrialization, urbanization, and modernization have made modern life more convenient but at the same time, also created various pollutants at an alarming level. In response to this, extensive research have been conducted to develop advanced analytical, biochemical, and physicochemical methods to degrade hazardous chemical compounds in air, water, and soil. In particular, photocatalysts (or semiconductor photocatalysts to be precise) have found to be effective in treating wastewater for the past few decades as this method offers several advantages over other alternatives such as complete mineralization without waste disposal problem, low cost, and operable at mild conditions.

1.2 General Description of LIB

A typical LIB generally consists of a cathode (positive electrode), an anode (negative electrode), a separator between them (allows the migration of Li^+ while forbidding the migration of electron), and an electrolyte (Figure 1.1).[1] The first generation of LIB employs graphite as anode, while layered $LiCoO_2$ (LCO) as cathode, and a mixture of $LiPF_6$/ethylene carbonate/dimethylene carbonate as electrolyte. During its charging process, Li^+ exits the LCO structure and migrates to the graphite via the electrolyte; meanwhile, driven by the external electric field, the associated electron flows from cathode to anode. Upon discharging, the migration paths for both Li^+ and electron are reversed.

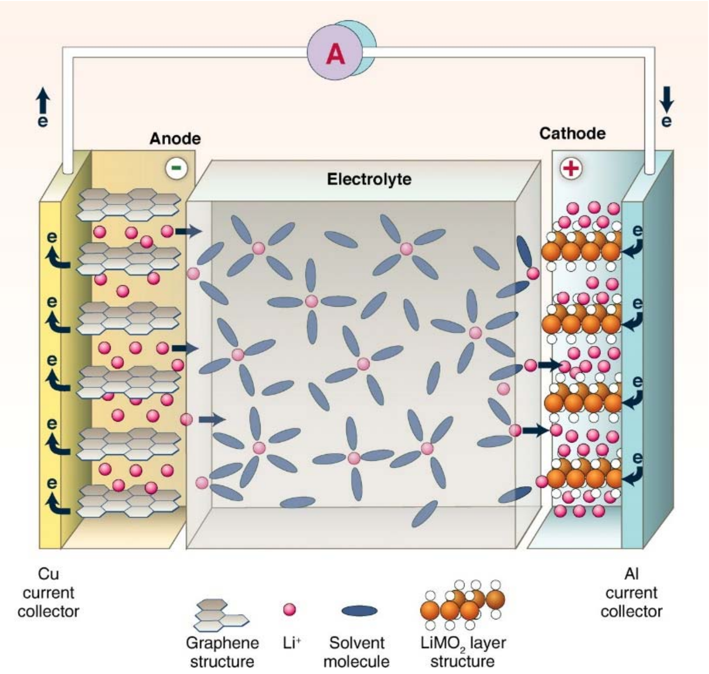

Figure 1.1 Schematic illustration of a typical LIB.[1]

Table 1.1 Comparison of performance between LIB and traditional secondary batteries.

	Lead-acid	**Ni-Cd**	**Ni-MH**	**Li-ion**
Voltage (V)	2.0	1.2	1.2	3.6
Specific energy (Wh kg^{-1})	30-40	40-50	70-80	120-150
Cycle life (times)	200-500	500	500	500-1000
Self-discharging rate per month (%)	5	25-30	30-35	6-9
Price (HKD Wh^{-1})	1-2	——	7.2	4
Memory effect	YES	YES	YES	No
Pollution	YES	YES	No	No

In comparison with traditional secondary batteries, LIB possesses unbeatable advantages at an acceptable price (see Table 1.1).[2] The performance of LIB performance is highly dependent on the intrinsic physiochemical properties of positive and negative electrode materials. The criteria for selecting effective electrode materials include: (1) high specific density; (2) high (cathode) and low (anode) redox potential; (3) good compatibility with electrolyte; (4) simple electrode kinetic mechanism; (5) high degree of reversibility; (6) good environmental benignity; (7) absolute safety; and (8) low price.[3–5] Recently, significant progress has been made in anode materials by developing Si,[6,7] Sn,[8,9] Ge,[10–12] and metal oxides (SnO_2,[13,14] Fe_2O_3,[15,16] CuO,[17] etc.), which are capable of providing much higher specific capacities than that of conventional graphite anode (372 mAh g^{-1}). Meanwhile, as the choice of cathode material does not only determine a battery's price (which can take up 30-40% of its commercial cost), but could also greatly impact the battery's performance,[18] the search for new-fashioned cathode materials to satisfy the increasing demand has, thus, become very important.

1.3 Cathode Materials for LIB

An ideal cathode material for LIB should satisfy the following requirements:

1. High redox potential to ensure high cell voltage;
2. Reversible Li^+ insertion/removal to guarantee stable cycling;
3. Ability to accommodate a large number of Li^+ per unit cell to achieve high capacity;
4. A fast Li^+ transfer kinetic mechanism to acquire high conductivity;
5. Stable in electrolyte;
6. Simple to obtain and inexpensive.

Currently, the most popular cathode materials mainly include layered lithiated transition metal oxides (LCO and $LiNi_{1-x-y}Co_xMn_yO_2$), spinels ($LiMn_2O_4$), vanadium oxides, and polyanion compounds (phosphates, borates, and silicates).

1.3.1 $LiCoO_2$

LCO was initially proposed as a cathode material for LIBs by Goodenough et. al in 1980.[19] The material was then commercialized by SONY in 1991 and has gained huge success in a wide range of application scenes from cell phones to EVs. Under ambient conditions, LCO belongs to the R3m point group with an α-$NaFeO_2$ structure in hexagonal symmetry (as sketched in Figure 1.2). Although in theory, LCO possesses a theoretical capacity as high as 274 mAh g^{-1} upon complete removal of Li^+ from its unit cell, the $Li_{1-x}CoO_2$ structure tends to become unstable at high levels of delithiation (x exceeds 0.5)[20] and therefore, the upper cut-off voltage for charging a LCO LIB is generally limited to ~4.2 V (vs. Li/Li^+), which corresponds to a practical capacity of ~140 mAh g^{-1} (which equals ~0.5 Li per unit cell of LCO). Another concern is that elemental cobalt is very costly and highly toxic, which limit its applications and prompt scientists to look for other candidates for energy applications.

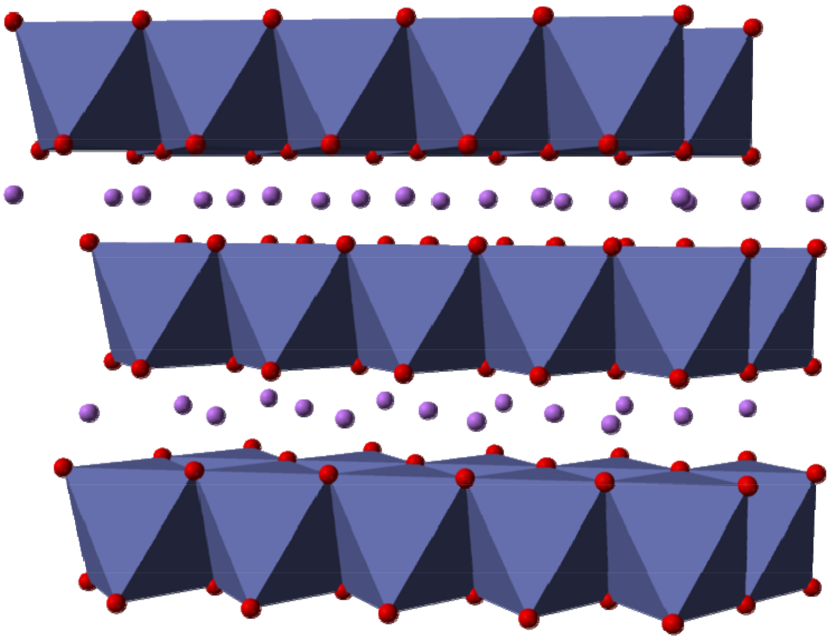

Figure 1.2 Lattice structure of LCO.

In view of the above, layered oxide $LiNi_{1/3}Mn_{1/3}Co_{1/3}O_2$ (NMC), isotypic with LCO, has been regarded as a promising cathode material because of its enhanced structural stability, lower price, and better environmental compatibility when compared with LCO.[21] However, NMC suffers from rapid capacity loss during repeated cycling, and further development is essential to address this shortcoming.

1.3.2 $LiMn_2O_4$

$LiMn_2O_4$ (LMO), as introduced by Trackeray et. al in 1983,[22] owns the Fd3m point group with a spinal structure in cubic symmetry (as sketched in Figure 1.3). LMO has a theoretical capacity of 148 mAh g^{-1} (~120 mAh g^{-1} in practice) with a potential of ~4 V, thus, offering an inexpensive and non-toxic substitute for cathode in LIBs offering high thermal stability and acceptable rate capability.[23–25] However, a number of factors have hindered the application of LMO on a large-scale: (1) poor electrolyte compatibility owing to its slow dissolution of manganese into the electrolyte; (2) fast capacity loss due to the John-Teller distortion of Mn^{3+} in deep charge-discharge, especially at elevated temperatures (> 50 ˚C); and (3) loss of oxygen during the charging process.[26–28] Currently, efforts have been made to improve the cathodic performance of LMO for future commercial applications via size reduction or doping.[29]

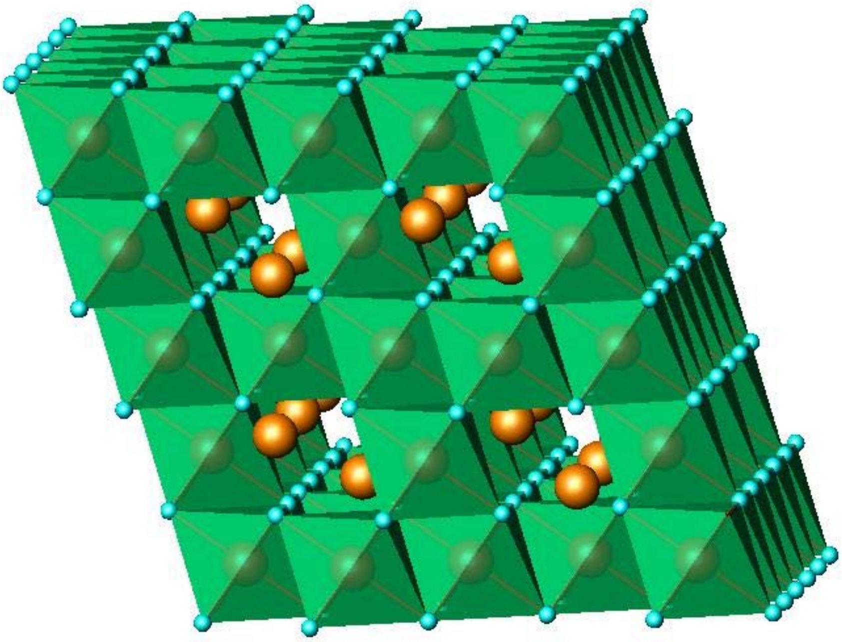

Figure 1.3 Lattice structure of $LiMn_2O_4$.

1.3.3 $LiFePO_4$

In search of next-generation cathode materials for LIBs, special attention has been drawn to polyanion compounds (eg. $LiFePO_4$ (LFP),[30] $LiFeBO_3$,[30] $LiFeSO_4F$,[31,32] Li_2FeSiO_4,[33–35] etc.) because of their excellent thermal stability and outstanding electrochemical performance. Among these compounds, phosphates (such as LFP and $Li_3V_2(PO_4)_3$ (LVP)) possess better structural stability due to the confining effect of oxygen atoms in PO_4 tetrahedrons. Because their delithiated products ($FePO_4$ and $V_2(PO_4)_3$) share exactly the same crystal structure and space group with that of LFP and LVP, respectively, there is little volume/structure change during charging/discharging. Both LFP and LVP also exhibit high theoretical capacity with high operating voltage, and are environmentally friendly, and thus, showing great potential as future large-scale cathode materials.

Olivine LFP (orthorhombic structure, point group Pnma, as sketched in Figure 1.4) was suggested to serve as a cathode material in 1997 by Goodenough.[36] LFP can deliver a theoretical capacity of 170 mAh g^{-1} at a single voltage plateau of ~3.4 V (vs. Li/Li^+). However, one fatal disadvantage associated with LFP is its low intrinsic electrical conductivity (σ, 10^{-10} – 10^{-9} S cm^{-1}), a result of the modulating arrangement of FeO_6 octahedrons separated by insulating PO_4 tetrahedrons (as can be seen in Figure 1.4). In order to enhance the practical application of LFP, modifications would be essential.

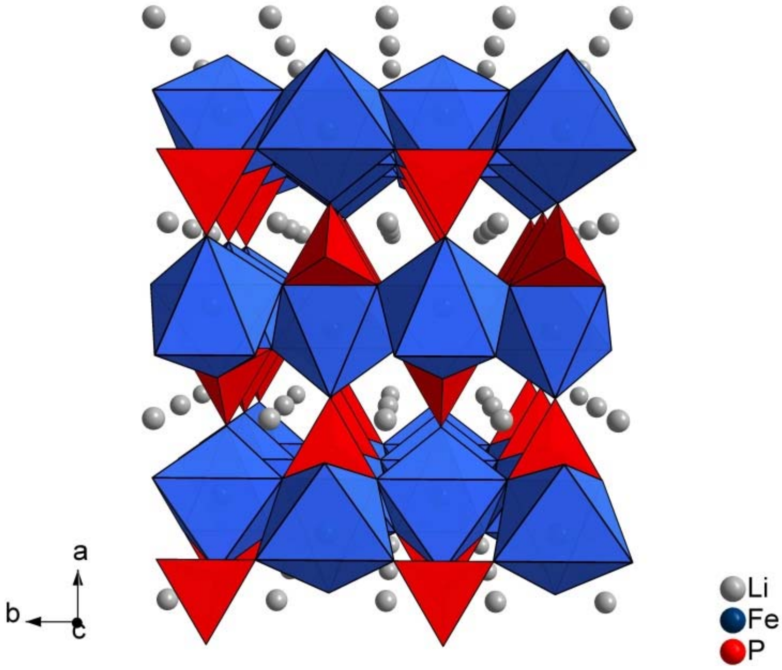

Figure 1.4 Lattice structure of $LiFePO_4$.

To improve the performance of LFP, a number of approaches have been developed and they can be categoried into three types:[37–42] conductive surface coating, size reduction to nanoscale, and doping with metal ions. In conductive surface coating, the mostly commonly used coating material is carbon (amorphous carbon, graphite carbon, carbon nanotubes, graphene), while metal nanoparticles (Cu, Ag), metal oxides (SiO_2, CeO_2, V_2O_3, ZnO, CuO, ZrO_2), and conductive polymers have all been proved to be useful in improving the electrochemical performance of LFP.[43–46] Reducing the particle size of LFP towards nanometer scale is another effective method to improve LFP performance as it can reduce the diffusion distance of Li^+ in LFP, resulting in better utilization of LFP's theoretical capacity.[47] Controlling the morphology of LFP nanoparticles is also helpful in achieving better LFP performance. For example, the nanoporous structure in LFP particles is quite beneficial for the infiltrating on of electrolyte that accelerates the electrochemical process.[48–50] The method of metal ions doping aims to produce lattice defects to promote the diffusion of Li^+, which is the only method to increase the conductivity of LFP, and a number of ions (eg.: Ti^{4+}, Nb^{5+}, W^{6+}, Zr^{4+}, V^{5+}, Mg^{2+}, Mn^{2+},Cu^{2+}, etc.) have been introduced to modify LFP system towards better performance.[40,51–54] Although most of these ions were found to be effective, the mechanism remains controversial. [43,45,46,55–58]

Despite the continuous development of LFP, redox potential of LFP remains rather low (showing comparable gravimetric energy density to LCO). Subsequently scientists have turned their attention to other phosphates with high operating voltages, such as $LiMnPO_4$ (~4.1 V vs. Li/Li^+)[59], $LiNiPO_4$ (~5.2 V vs. Li/Li^+)[60], and $Li_3V_2(PO_4)_3$ (~4.0 V vs. Li/Li^+)[61,62].

1.4 $Li_3V_2(PO_4)_3$

LVP possesses the highest theoretical capacity (197 mAh g^{-1}) among all high-voltage phosphate cathode materials. Other desirable qualities of LVP include abundant resources, high level of safety, and rapid ionic diffusion;[63] thus, it is particularly suitable for the next-generation high-energy LIBs for large-scale application such as EVs.

1.4.1 Lattice Structure

LVP possesses two individual crystal structures: the rhombohedral structure (NASICON type, sodium superionic conductor), and the thermally more stable monoclinic structure (shown in Figure 1.5).[64,65] These two structures can be differentiated by the interconnecting ways of their "lantern" units (the $V_2(PO_4)_3$ unit). The rhombohedral LVP (a = 8.316(1) Å, c = 22.484(1) Å; space group $R\bar{3}$)[66] consists of VO_6 octahedra and PO_4 tetrahedra connected via vertex oxygen atoms, forming "lantern" units along the [100] direction and the lithium atom is located on a unique 4-fold coordinated crystallographic site.[66]

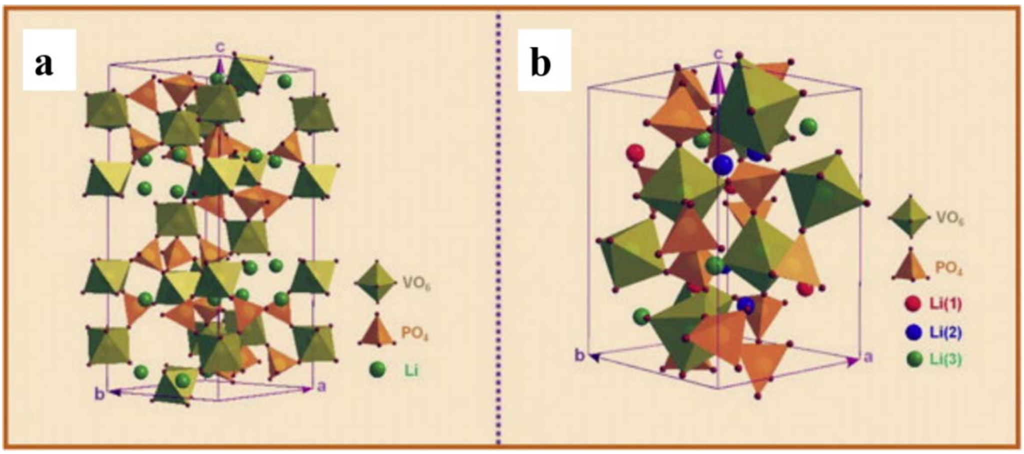

Figure 1.5 Polyhedral representation of (a) a rhombohedrally structured LVP and (b) a monoclinically structured LVP.[62]

The monoclinic LVP (a = 8.605(1) Å, b = 8.591(1) Å, c = 12.038(1) Å, and β = 90.60(1)° with space group P21/n) crystallizes into a slightly more complex structure. Both VO_6 octahedra and PO_4 tetrahedra are distorted and the vanadium atoms occupy two different positions: V(1) and V(2) with average V-O bond lengths of 2.003 and 2.006 Å, respectively.[64] Lithium atoms has three distinct sites in the interstitial voids. According to the Li solid-state nuclear magnetic resonance (NMR) spectrum analysis by Nazar et. al, Li(1) sits in the tetrahedral site whereas Li(2) and Li(3) occupy two pseudo-tetrahedral sites (five-coordinate Li-O sites) with an additional long Li-O bond (~2.6 Å).[64,67] These three lithium sites have a microsecond mobility as revealed by two-dimensional exchange spectroscopy (2D EXSY),[68] which is far faster than the millisecond lithium hoping dynamics in LMO structure.[69]

As extracted by differential scanning calorimetry (DSC), temperature-dependent X-ray diffraction (XRD), and Raman spectra, monoclinic LVP also undergoes three structural changes upon continuous heating: monoclinic α-phase at room temperature, monoclinic β-phase at middle-temperature (ca. 400-460 K), and orthorhombic γ-phase at high-temperature (ca. 460-573 K).[70–73] These phase transitions are reversible upon cooling to room temperature. It should be noted that monoclinic LVP could become unstable and V(III) could be oxidized under elevated temperature of above 800 K in air.[73]

1.4.2 (De)Lithiation Mechanism

The voltage-composition behaviors of rhombohedral LVP and monoclinic LVP are highly distinct from each other due to their structural differences. Rhombohedral LVP, which can only be synthesized via ion exchange from its corresponding sodium analogue ($Na_3V_2(PO_4)_3$), displays one flat voltage plateau at ~3.7 V vs Li/Li^+ based on the V^{3+}/V^{4+} redox couple, associated with a two-phase transition between the compositions of $Li_1V_2(PO_4)_3$ and $Li_3V_2(PO_4)_3$.[66,74–76] In comparison, the monoclinic LVP exhibits a much better electrochemical properties than those of rhombohedral LVP in which every Li^+ can be reversibly removed/inserted. The theoretical capacity for monoclinic LVP could reach as high as 197 mAh g^{-1},[67] the best among all reported lithium transition metal phosphates and therefore, our work particularly focuses on the monoclinic phase of LVP.

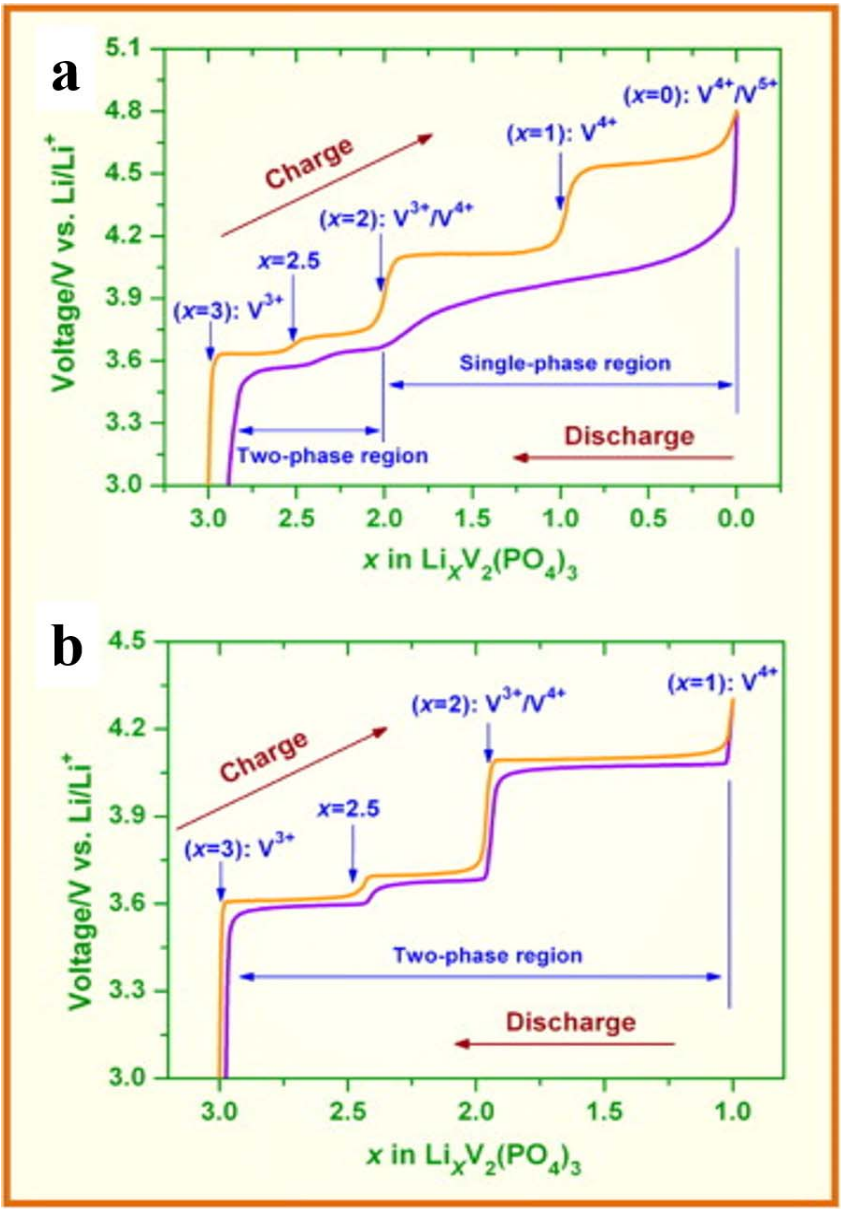

Figure 1.6 The electrochemical voltage-chemical composition profiles of LVP in the voltage range of 3.0-4.8 V (a) and 3.0-4.3 V (b) vs. Li/Li$^+$.[62]

The electrochemical voltage vs. chemical composition profiles for lithiation/delithiation is sketched in Figure 1.6. In a range of 3.0 – 4.8 V vs. Li/Li$^+$

(Figure 1.6a), there are four plateaus in the oxidation curve, locating at about 3.6, 3.7, 4.1, and 4.6 V vs Li/Li$^+$, corresponding to a sequence of phase transition for the single phase $Li_xV_2(PO_4)_3$ (x = 3.0, 2.5, 2.0, 1.0, and 0).[64,75,77–79] Li(3) (see Figure 1.5b), the highest energy site, is firstly extracted during the oxidation.[79] This process can be divided into two stages: ($Li_3V_2(PO_4)_3 \rightarrow Li_{2.5}V_2(PO_4)_3 \rightarrow Li_2V_2(PO_4)_3$) due to the existence of the ordered and stable $Li_{2.5}V_2(PO_4)_3$ phase, corresponding to the voltage plateaus at 3.6 and 3.7 V vs Li/Li$^+$. The following Li$^+$ (Li(1)) is extracted via a two-phase process ($Li_2V_2(PO_4)_3 \rightarrow LiV_2(PO_4)_3$) as well as the full oxidation from V^{3+} to V^{4+}. The last Li$^+$ (Li(2)) is extracted through a similar two-phase process ($LiV_2(PO_4)_3 \rightarrow V_2(PO_4)_3$) at a voltage of 4.6 V, together with the full oxidation from V^{4+} to V^{5+}, which is kinetically the most difficult step due to the reduced ionic/electronic conductivity from the completely empty "lantern" units ($V_2(PO_4)_3$).[64] The overall volume contraction after removal of all three Li$^+$ is 7.8%, which is a result comparable to that of $LiFePO_4$ (6.6% volume reduction from $LiFePO_4$ to $FePO_4$);[80] therefore, the monoclinic symmetry is reserved in the $V_2(PO_4)_3$ structure. It should be noted that in the $V_2(PO_4)_3$ product, two vanadium atoms exhibit almost the same bond distances and thus, possess the same oxidation state (+ 4.5),[80] suggesting there is little difference between the lithiation process and the above delithiation process. The initial lithiation shows a typical solid-state behavior (single-phase reaction, as can be identified by the "S" curve); consequently, a two-step lithiation ($Li_2V_2(PO_4)_3 \rightarrow Li_{2.5}V_2(PO_4)_3 \rightarrow Li_3V_2(PO_4)_3$) is evidenced by two obvious voltage plateaus, locating at 3.65 and 3.58 V, respectively.

The overall mechanism for charge/discharge reactions can be written as follows:

Charge:

$$Li_3V_2^{3+}(PO_4)_3 - 0.5Li^+ - 0.5e \rightarrow Li_{2.5}V^{3+}V_{1/2}^{4+}(PO_4)_3$$

$$Li_{2.5}V^{3+}V_{1/2}^{4+}(PO_4)_3 - 0.5Li^+ -0.5e \rightarrow Li_2V^{3+}V^{4+}(PO_4)_3$$

$$Li_2V^{3+}V^{4+}(PO_4)_3 - Li^+ - e \rightarrow LiV_2^{4+}(PO_4)_3$$

$$LiV_2^{4+}(PO_4)_3 - Li^+ - e \rightarrow V_2^{4.5+}(PO_4)_3$$

Discharge:

$$V_2^{4.5+}(PO_4)_3 + 2Li^+ + 2e \rightarrow Li_2V^{3+}V^{4+}(PO_4)_3$$

$$Li_2V^{3+}V^{4+}(PO_4)_3 + 0.5Li^+ + 0.5e \rightarrow Li_{2.5}V^{3+}V_{1/2}^{4+}(PO_4)_3$$

$$Li_{2.5}V^{3+}V_{1/2}^{4+}(PO_4)_3 + 0.5Li^+ + 0.5e \rightarrow Li_3V_2^{3+}(PO_4)_3$$

Specifically, when the cut-off voltage is limited to 3.0 – 4.3 V vs. Li/Li^+ (Figure 1.6b), no solid-state region is presented. The electrode exhibits three charge plateaus and three corresponding discharge plateaus, associating with the two-phase transition ($Li_3V_2(PO_4)_3 \xrightarrow{3.6V} Li_{2.5}V_2(PO_4)_3 \xrightarrow{3.7V} Li_2V_2(PO_4)_3 \xrightarrow{4.1V} LiV_2(PO_4)_3$); therefore, the material becomes fully reversible with a theoretical capacity of 133 mAh g^{-1}.

Table 1.2 Comparison of performance between cathode materials for LIBs.

	$LiCoO_2$	$LiMn_2O_4$	$LiFePO_4$	$Li_3V_2(PO_4)_3$
D_{Li+} (cm^2 S^{-1})	10^{-8} -10^{-7}	10^{-10} -10^{-8}	10^{-16} – 10^{-14}	10^{-12} – 10^{-10}
Electronic conductivity (S cm^{-1})	10^{-3}	10^{-5}	10^{-10}	10^{-8}
Voltage (V)	3.7	4.0	3.4	4.0
Specific capacity (mAh g^{-1})	274 (140)	148 (100)	170	197
Power density (Wh kg^{-1})	518	400	578	788

As can be seen from Table 1.2, although LVP presents similar voltage plateaus as those of LCO and LMO, it possesses much higher energy density, thermal stability, and environmental benignity. Compared with LFP, monoclinic LVP offers higher diffusion constant, discharge voltage and energy density. As for the toxicity of vanadium, Nazar et. al. have clearly stated that vanadium is safe to many animals.[67] Because of the factors above, LVP is generally considered as the best candidate for next-generation cathode materials, especially for EVs application. However, analogue to LFP, the separated arrangement of conducting VO_6 octahedra by insulating PO_4 tetrahedra in LVP's lattice leads to poor conductivity of this material and it would be essential to modify LVP before they can be applied into real cells.

1.4.3 LVP Structural Modifications

Previous studies have proposed a number of methods that contribute to the improved electrochemical performance of LVP products with various morphologies (summarized in Figure 1.7). In general, the modification of LVP is directly inspired by the development of LFP and the methods used to modify LVP are similar to those of LFP, i.e., size reduction, carbon/oxide coating, and metal ions doping.

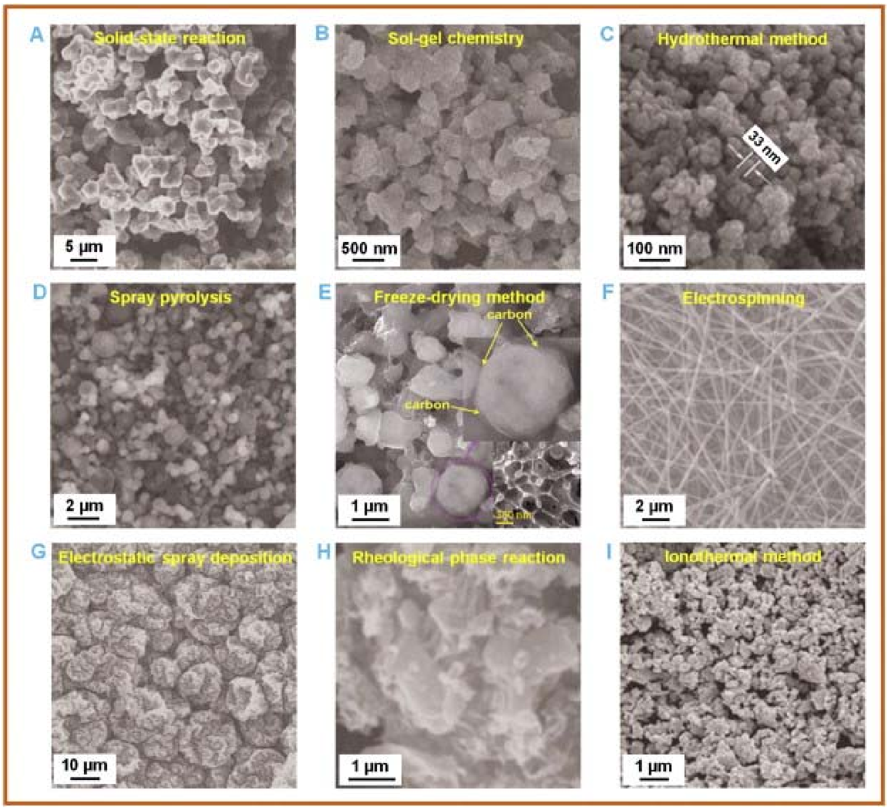

Figure 1.7 The morphology of LVP cathode materials prepared by different methods.[62] (a) Solid-state reaction. (b) Sol–gel chemistry. (c) Hydrothermal method. (d) Spray pyrolysis. (e) Freeze-drying method. (f) Electrospinning. (g) Electrostatic spray deposition. (h) Rheological phase reaction. (i) Ionothermal method.

1.4.3.1 Size Reduction

The "mosaic model" in LFP proposed by Andersson et al.[47] is also suitable for the lithiation/delithiation process of LVP materials. The "dead space" throughout the whole particle that cannot be accessed by Li^+ would become larger together with the increase of particle size, resulting in higher capacity loss. A reduction in particle size can therefore effectively shorten the Li^+ diffusion distance and simplify the lithiation/delithiation as well as decrease the inaccessible "dead space" greatly to boost the LVP utilization in the electrode. Li et al. adopted a sol-gel method and obtained a LVP-carbon (LVP/C) composite with an average size of ~70 nm.[81] The reduced particle size increased the inter-particle electrical contact, thus, improving its electrochemical performance (when compared with conventional solid-state sample). The initial discharge capacity reached 155.3 mAh g^{-1} at the current density of 28 mA g^{-1} in the voltage range of 3.0 – 4.8 V, and the capacity retained as 143.6 mAh g^{-1} after 50 cycles. Pan et al. synthesized LVP/C composite with an average diameter of <50 nm from a special carbon source (KB carbon),[82] and the resulting composite exhibited an superior rate capability and capacity retention. The initial discharge capacity of this composite was 122 mAh g^{-1} at 1C, and 83 mAh g^{-1} at 32C in the voltage range of 3.0 - 4.3 V. Du et al. synthesized mesoporous LVP/C microspheres using Baker's yeast cells as both mesoporous structure templates and amorphous carbon sources.[83] These microspheres are composed of densely aggregated nanoparticles (20 – 40 nm) as well as interconnected nanopores (2 – 15 nm), which are beneficial for the infiltration of electrolyte and diffusion of Li^+. The discharge capacity of the mesoporous LVP/C microspheres was high (about 126.7 mAh g^{-1}) with only 2% capacity loss of the initial value at the 50th cycle at a current density of 0.2 C, and a high rate capacity of 100.5 mAh g^{-1} at 5 C in the region of 3.0–4.3 V.

1.4.3.2 Carbon/oxide Coating

So far, carbon coating has been regarded as the simplest and most effective method to improve the performance of LVP. This approach does not only improve the electronic conductivity of the electrode material as a result of the construction of conductive “bridges” between insulating particles, but also prevent the direct contact between LVP and electrolyte to avoid the dissolution of V^{3+} into electrolyte. In 2002, Huang et al. were first to report the success of using carbon coating on LVP to achieve excellent electrochemical performance,[67] and this discovery has triggered the research of applying carbon coating on LVP for enhanced performance. For example, Chang et al. used glucose as carbon source and synthesized carbon-coated LVP via a hydrothermal method.[84] The resulting material exhibited a high initial discharge capacity of 178, 173 and 172 mAh g^{-1} at 0.1C, 0.2C and 0.5C between 3.0 and 4.8 V, respectively. Moreover, it displayed good fast rate performance, by which discharge capacities of 136, 132 and 127 mAh g-1 can be delivered after 100 cycles between 3.0 and 4.8 V at a different rate of 1C, 2C and 5C, respectively. Subsequently, Rui et al. studied the effects of different carbon sources (citric acid, glucose, PVDF and starch), and found that LVP/C composite from citric acid performed the best (with almost no capacity fade after 100 cycles in 0.2C).[84] Wang et al. prepared a LVP/C film via electrostatic spray deposition, and obtained capacities of 118 (1C) and 80 (24C) mAh g^{-1} when using the film as cathode.[85] Zhou et al. also studied the effects of carbon sources (humic acid, glucose, and carbon), and the sample from humic acid showed the best cyclic performance (during the 200th cycle, the capacity of the sample from humic acid remains at 145.2 mAh g^{-1} at 1C.).[86] A number of materials have been used as carbon sources in synthesizing LVP/C composites, including: sucrose,[87] maltose,[88,89] polyvinyl alcohol,[90–92] stearic acid,[93] oxalic acid,[94] glycine[95] etc. Although the enhanced electrochemical performance brought by carbon coating is already confirmed by several individual works, its applications in LVP systems remain relatively limited when compared with LFP, and the interfacial chemistry between LVP-C requires further optimization for better performance.

A great deal of studies have found that metal oxide coating could also enhance the electrochemical performance of cathode materials for LIBs.[96–100] One possible reason for this is that metal oxide forms a protective layer on active material to prevent its contact with electrolyte, thus, slowing the dissolution of active material to gain extra structural/cycling stability. Another factor leading to the enhanced performance could be that the introduction of metal oxide in proper concentration improves the conductivity of the active material and hence, reduces the charge-transfer resistance as well as the activation energy for Li^+ transfer. This boosts the kinetic process of electrode reaction that results in improved electrochemical performance. So far, the most effective metal oxides used in cathode for LIBs include SiO_2, ZnO, CeO_2, TiO_2, ZrO_2, and Al_2O_3. For example, Zhai et al.[101] found that MgO nanocoating (thickness: 2.0 – 2.5 nm) stabilized the structure of LVP, decreased the interface charge transfer resistance and enhanced the reversibility of electrode reaction. In this study, enhanced initial discharge capacity, cyclability and rate performance were studied. The initial discharge capacity is 194.4 mAh g^{-1} at 40 mA g^{-1} current density, close to the theoretical discharge capacity, and the discharge capacity remains 137.5 mAh g^{-1} after 100 cycles with a capacity retention of 70.73% which is higher than that of pristine LVP/C (43.7%). The initial discharge capacity maintains at 157.81 mAh g^{-1}, 157.29 mAh g^{-1} and 144.64 mAh g^{-1} at 1C, 1.5C, 2C rates, respectively.

Conductive polymers (polypyrrole, polyamine, etc.) have also been introduced to LVP system,[102] but the development of their applications are still in an early stage due to the lack of conductive polymeric material with proper and stable electrochemical window.

1.4.3.3 Metal Ions Doping

Similar to LFP, the carbon coating can effectively improve the electronic conductivity of LVP yet the introduction of large amount of carbon would decrease the tap density of the material and hence, decrease the volumetric energy density, an undesirable effect for large-scale applications of LVP. To address this issue, metal ions doping has been proposed to enhance the electrochemical performance of LVP as it can improve LVP’s intrinsic conductivity while maintaining its tap density.

LVP possesses two metallic positions, Li(M1) and V(M2), which can be either separately or simultaneously doped by guest ions. Morgan et al. presented combined experimental and first-principle findings to study the effects of Ti, Al, and Cr doping (on V(M2)) on the structural and electrochemical performances of LVP.[103] It was found that Ti atom could influence both the structure and electrochemical properties, whereas Al and Cr atoms seem to have little effect on conductivity . Ren et al. reported that $Li_3Fe_xV_{2-x}(PO_4)_3/C$ (x = 0.02 – 0.04) had better properties than undoped LVP because of increased electrical conductivity and structural stability derived from the incorporation of the Fe^{3+} ions.[103] Chen et al. also reported that in $Li_3V_{2-x}Cr_x(PO_4)_3/C$, although the initial specific capacity decreased with Cr content at a lower current rate, both cycle performance and rate capability have improved significantly with moderate Cr-doping content.[104] Dai and Huang both asserted the positive effects of Mg^{2+} doping on the electrochemical improvement of LVP.[105,106] The doping effects of Co^{2+},[107] Mn^{2+},[108] Ni^{2+},[109] Ca^{2+},[110] Ce^{3+},[111] Sc^{3+},[110] Sn^{4+} [112] have also been extensively examined by different research groups.

Mateyshima et al. studied the effects of substitution of Li(M1) via guest ions and found that the doping of K^+ on Li(M1) could negatively affect the electrochemical property of LVP.[113] A study from Yan et al. revealed that the $Li_3V_2(PO_4)_{2.88}Cl_{0.12}/C$ composite presented an excellent discharge capacity of as high as 106.95 mAh g^{-1} after 80 cycles at 8 C, a result of decreased polarization and reduced charge transfer resistance of electrode with a suitable Cl-doping amount.[114]

In summary, a number of studies have confirmed the introduction of metal ions could enhance the electrochemical properties (especially the high-rate and cycling performance) on LVP by reducing the particle size, decreasing the charge-transfer resistance, increasing the electronic conductivity, and enhancing the structural stability. The current research mainly focuses on property enhancement of LVP brought by guest ions. Due to a lack of reliable and specific experimental data, the concepts and/or mechanism of metal oxide coating or metal ions doping remains controversial and further research are needed in this area.

1.5 Carbon-based Photocatalysts

1.5.1 Introduction of Photocatalysts

The initial discovery of photocatalytic water splitting on TiO_2 electrodes by Fujishima & Honda in 1972 has fueled the research on semiconductor photocatalysts.[115] Since then significant progress has been made in this area and various highly active semiconductor photocatalysts have been identified for their electrochemical ability in environmental remediation and solar energy conversion. These semiconductors (e.g., ZnO, TiO_2, WO_3, CdS, BiOCl, $BiVO_4$, etc.) can act as photocatalysts for light-induced chemical transformations due to their novel electronic structure, composed of a filled valence band (VB) and an empty conduction band (CB). When the semiconductor adsorbs a photon with its energy match or exceeds the bandgap energy (E_g) of the semiconductor, an electron in the

VB will then exit to the CB, leaving a positive hole in the VB. Such photogenerated electrons and holes play an important role in pollutant degradation, photocatalytic disinfection, and solar energy conversion (including hydrogen production and solar photovoltaics). However, the photogenerated electrons and holes in their excited states are often unstable and could recombine easily (the input energy is, thus, dissipated as heat), resulting in rather low efficiency of photocatalytic reactions.[116–118]

During the past few decades, comprehensive studies have been conducted to improve the photocatalytic performance of semiconductor photocatalysts by means of: (i) extending the photoresponse of UV-activated semiconductors (especially TiO_2) into the visible region via bandgap tuning or the introduction of a photosensitizer; (ii) suppressing electron-hole recombination; and (iii) promoting the forward reaction through localizing reactants adjacent to the active sites on photocatalyst.[119] Generally, the methods adopted include coupling with a narrow bandgap semiconductor,[120–124] metallic/nonmetallic doping,[125–127] noble metal loading,[128–130] dye-sensitization,[131–134] composing carbon materials.[135–140]

1.5.2 Carbon in Photocatalysts

Today much attention has been given to the use of carbon materials to enhance the photocatalytic ability of photocatalysts. The introduction of carbon nanostructures in composite photocatalysts not only suppresses the charge recombination,[141] but also benefits a hydrophobic environment for localizing concentrated reactant surrounding the active sites.[142] Moreover, recent work has also confirmed that carbon can act as a sensitizer when it forms a complex interface with TiO_2, or as impurity energy levels through the formation of Ti-O-C bonds to extend its active region.[143,144]

Zhang et al. reported an extension of TiO_2's response into visible light region by coating thin carbon layers (~ 1 nm) on TiO_2 nanoparticles. They believed that the electron coupling, a result of d-π interaction (d-orbit of the TiO_2 conduction band and π-orbit of the graphite carbon), was responsible for the extended light adsorption.[145] In another study, Kamat and his co-workers synthesized TiO_2 nanocrystals/graphene oxide composite by sonicating TiO_2 nanoparticles and graphene oxide sheets in ethanol, and demonstrated the possibility of using reduced graphene oxide as an electron reservoir and a transfer medium in the composited photocatalyst.[146,147] Zhang et al. then synthesized graphene/TiO_2 (P25) composite from hydrothermal reaction with enhanced photocatalytic activity for the degradation of methylene blue in aqueous solution.[136] The findings of these studies show that carbon modification for semiconductor photocatalysts could be a promising technology in boosting their performance for practical applications as it facilitates electron transport and light adsorption, creates a substrate localization effect, and improves the dispersion of photocatalysts.

1.5.3 Nb_2O_5 as Photocatalyst

As a key semiconductor material with a wide range of catalytic applications (e.g. (de)hydration, hydrolysis, condensation, alkylation, dehydrogenation, and especially, photodegradation of harmful organic contaminants and photo-splitting of water to produce hydrogen), niobium oxide (Nb_2O_5, E_g = 3.4 V) is thus quite promising for both energy and environmental applications.[148] Prado et al. showed that Nb_2O_5 performed better in photodegradation of organic dyes than that of TiO_2 and ZnO after 10 catalytic cycles[149] with the advantages of easy recovery and long-term stability in photocatalytic reactions.

However, the degradation rate of Nb_2O_5 is much slower than that of TiO_2 and ZnO.[149] To improve the photocatalytic efficiency of Nb_2O_5 material, many new materials based on modified Nb_2O_5 have been created as improved photocatalysts, either by metallic (Mo, W)/nonmetallic doping (N) or by rational compositing (Pt, Au Cu, NiO, $SrNb_2O_6$, In_2O_3, chitosan, etc.).[150–156] Some research found that layered niobates ($KNbO_3$, HNb_3O_8) could also help to improve photocatalytic performance, which may be caused by their layered structures that facilitate the photoexcited charge transfer and the charge separation.[154,157]

Similar to TiO_2, Nb_2O_5 is almost inert to visible light because of its relatively large bandgap, a major osbtacle that hinders its practical applications. The majority of synthetic Nb_2O_5-based materials are only active under the illumination of ultraviolet light that constitutes only a small fraction (< 5%) of the entire solar spectrum. Generally, N-doping was found to be effective for visible light harvest due to the narrowed bandgap by mixing N2p and O2p states, an effect similar to that found in TiO_2.[158] It should be noted that recently, a weak visible light response was obtained from a Nb_2O_5/Cr_2O_3/Carbon cluster composite material by introducing carbon cluster as a visible light adsorption site and an electron transfer bed, synthesized via a high temperature calcination method.[159]

1.6 Carbon Growth Mechanism under TEM

1.6.1 Introduction of TEM

Transmission electron microscopy (TEM) is an analytical technique on microstructure investigation in material science whereby a beam of electrons is accelerated (accelerating voltage: 80-500 kV) before transmitting through an ultrathin specimen (specimen thickness: < 100 nm), and interacting with the specimen as it passes through. Therefore, an image can be formed from the sample-specimen interaction, which is then magnified and focused on an imaging device (fluorescent screen), and recorded by a sensor such as an CCD (charge-coupled device) at an atomic resolution.

Furthermore, the sample-specimen interaction is actually rather complex which produces various signals that contain information about sample morphology, chemical composition and other properties. For example, the transmitted electron beam is inversely proportional to the thickness and atomic number of specimen, thus can be used to generate mass-thickness contrast image (either bright field or dark field). The energy loss of the elastically/in-elastically scattered electrons is quite concerning with the atomic species in the sample, so can be used to analyze the chemical composition of the sample (which is sensitive to light atoms). In addition, the sample atoms also have the possibility of emitting their characteristic X-rays upon excited by the incident high energy electron beam, which can be collected to further extract the chemical composition of the sample (which is sensitive to heavy atoms). In brief, with the help of varieties of functional modifications, modern TEM is quite powerful and suitable for characterization in material science, nanotechnology, and biosciences.

Beside of simply recording static images from the sample, recently, with appropriate experimental design, scientists are trying hard to observe in real time (in-situ) how the physicochemical process (chemical reaction, material deformation, phase/morphology change upon electrical/magnetic field, etc.) happens inside TEM and are starting to gain initial successes.[160] Therefore, the traditional structure-property relationship is possible to be further extended as structure-processing-property relationship, which should be of such help for us to understand the nature.

1.6.2 Carbon Growth Mechanism Revealed by TEM

Carbon are always the most important material for human life, and carbon nanostructures are of such special perspectives that they were unprecedentedly honored two Nobel prizes (fullerenes at 1996 and graphene at 2010). The growth of various carbon nanostructures therefore has been intensively studied, and TEM has proven to be an invaluable tool in understanding the mechanism involved.[161–167]

In 2004, Helveg et al. presented the first time-resolved, high-resolution, real-time TEM work of the formation of carbon nanofibers from methane decomposition over $MgAl_2O_4$ supported nickel nanocrystals.[161] Carbon nanofibers are observed to develop through a reaction-induced reshaping of the nickel nanocrystals. Specifically, the nucleation and growth of graphene layers are found to be assisted by a dynamic formation and restructuring of mono-atomic step edges on the nickel surface. Then in 2007, Rodríguez-Manzo et al. reported for the first time the nucleation of a carbon nanotube on the spherical surface of a catalyst particle.[164] Their result shows that there is direct bonding between the tubes and the metal surface from which the tubes sprout and can be explained by bulk diffusion of carbon through the body of the catalytic particles. Furthermore, in 2014, in the climax of graphene research, Rosmi et al. published their in-situ TEM visualization of a solid phase reaction process to achieve Cu assisted growth of graphene nanoribbon.[168]

All the above works are of significant importance in understanding the mechanism behind the carbon nanostructure growth. However, for the most acceptable growth mechanisms of carbon materials, vapor-liquid-solid and solid-liquid-solid models,[169] few result can be referenced. This is generally because that, it is of extreme difficulty in introducing the decisive liquid intermediate (melting catalyst) in these processes to the high-vacuum (up to 10^{-9} Pa) TEM chambers, which is quite worthy of noting.

1.7 Motivations of the Project

With reference to the literature review and an overview of works related to using carbon-based composite cathode materials for LIBs (with our special focus on LVP/C material) and photocatalytic (Nb_2O_5) applications above, it can be summarized that it is of both scientific and technological importance together with application perspective which draw such a broad range of interest in this specific domain. Hence more than many efforts have been contributed to seek the rational and applicable composited nanostructures and try to open up the abundant connotations, either physically or chemically, so as to satisfy the final market demand. However, despite the success of synthesizing and characterizing diverse composite structures, a number of issues remain to be addressed. For instance, we have yet to find electrode materials with high specific capacity as well as long lifespan for efficient LVP/C composites. For Nb_2O_5-based photocatalysts, improved photocatalytic performance together with extended active region are still in hot pursuit. It would also be essential to develop more novel composites so that the structure-property relationship of the composite can be thoroughly understood. Few if any attempt has been made to comprehend the growth mechanism and the function of process parameters under most synthetic approaches.

In an attempt to overcome these obstacles, the first objective of this thesis is to conduct a series of experiments to synthesize a range of rationally designed carbon-based composites. The second objective is to study the electrochemical/photocatalytic performances of these composites to ensure that they have enough potential for the proposed applications. The final objective is to understand the growth mechanism of carbon on host materials. It is anticipated that our as-developed synthetic approaches could be extended for use to other materials facing similar challenges.

1.8 Scope of the Work

The overall objective of this thesis is to fully examine the rational design and facile synthesis of LVP/C and Nb_2O_5/C composites by means of structural characterizations and property measurements, as well as to understand the mechanisms behind the composite formation and electrochemical/photocatalytic behavior.

This thesis is organized as follows:

A systematic review of the recent relevant work is presented in Chapter 1 including a brief introduction on LIBs, the state-of-the-art cathode materials for LIBs, recent synthetic contributions to LVP/C composites, general descriptions of photocatalysts and Nb_2O_5 material, as well as a brief introduction to the TEM understanding of carbon growth.

In Chapter 2, a facile carbothermal reaction is utilized to produce LVP/C micro-nano composite which features porous carbon nanoflakes entangled three-dimensionally on single-crystalline LVP microrods. Such composite shows improved electrochemical performance (especially the excellent rate capability) with exceptionally high tap density, a result that may be attributed to its novel hierarchical mesoporous–macroporous structure.

In Chapter 3, LVP/C core-shell nanospheres were incorporated into porous carbon framework via simple hydrothermal reaction. The hierarchical nanocomposite exhibited superior electrochemical properties with impressive stable cycling, even at very high current rate.

In Chapter 4, a novel nanocomposite of graphene nanoclusters decorated on Nb_2O_5 nanofibers was synthesized using electrospinning technique and hydrothermal treatment. The Nb_2O_5/C composite extended the active region of Nb_2O_5 material significantly, and hence, displayed an improved photocatalytic behavior in degradation organic dyes.

Chapter 5 mainly focuses on our attempt to understand the growth mechanism of nanostructured carbon on host particles. We made direct observations on the transition of amorphous carbon into graphene nanostructures at liquid-solid interfaces through transmission electron microscopy. Amorphous carbon was found first nucleated into nanoclusters at step-edges on particle surface before merging into graphene layers through kinetic restructuring via oriented-attachment.

Important findings, achievements and implications brought by the current study are summarized and presented in Chapter 6.

CHAPTER 2 HIGHLY ENTANGLED CARBON NANOFLAKES ON LVP MICRORODS FOR IMPROVED CATHODE PERFORMANCE

As reviewed in the previous chapter, LVP is such competitive in LIB applications, however, the low intrinsic conductivity plus the practical difficulty in realizing robust structure significantly hinder its large-scale deployment. Herein, a new-concepted “core/shell” configuration is established to suggest a pragmatic solution, by making porous carbon nanoflakes three-dimensionally entangled on single-crystalline LVP microrods. The LVP/C composite performs as superior cathode material with high capacity, stable cycling, and high rate capability. Hence, our design effectively tackles several urgent technological barriers of LVP material, making it suitable to meet the emerging applications.

2.1 Introduction

In response to the growing concern about world energy crisis and greenhouse effect caused by substantial consumption of fossil fuels, LIBs have become increasingly popular over the past two decades. LIB is considered to be one of the greatest successes of modern materials electrochemistry,[1,2,56,58] yet the performance of this battery chemistry has been limited using the current electrode and electrolyte systems. One of the most urgent tasks in advancing LIB technology therefore would be to explore new-fashioned cathode material, which not only dominates the electrochemical behavior of the whole battery but also determines large the manufacturing cost.[45,55] To date, besides conventional $LiCoO_2$, scientists' focus on cathode materials switched among layered mixed metal oxides (e.g., $LiNi_{0.8}Co_{0.15}Al_{0.05}O_2$ or $LiNi_{1/3}Co_{1/3}Al_{1/3}O_2$), spinel oxides ($LiMn_2O_4$), and polyanion-based compounds ($LiMnPO_4$, $LiFePO_4$, etc.).[46,170–173] Due to its rich reserve on earth, competitive energy density and remarkable thermal stability, monoclinic LVP has emerged as one of the most promising battery materials for next-generation lithium ion batteries. Specifically, LVP holds extra advantages including stable framework, high operating voltage, and large capacity. Theoretically, LVP can reversibly deliver $3Li^+$ when completely charged/discharged within a potential window of 3.0-4.8 V vs. Li^+, yielding a maximum discharge capacity of 197 mAh g^{-1}. It also possesses a reversible capacity of 133 mAh g^{-1} between 3.0-4.3 V based on V^{3+}/V^{4+} redox couple and thus, LVP has been frequently proposed to be used in newly emerging applications including EVs and portable electronics.[174–176]

However, like other lithiated transition metal phosphates, the intrinsic electronic conductivity of LVP is rather low, a fatal drawback that greatly hinders its practical applications.[176] To improve the electrochemical performance of LVP as in the case of $LiFePO_4$, conductive coating (carbon, RuO_2, conductive polymers, graphene, etc.)[174,177–182] or doping (Fe, Cr, Mg, Al, Ti, etc.)[179,183–185] has become essential.[43] Apparently, carbon coating is among the most economical and the most effective approaches.[44] According to the literature, ordinary core-shell carbon coating, i.e. by homogeneously distributing a thin carbon layer on the surface of the host material particles, can efficiently improve the electrochemical performance.[174,177,182,186–189] However, such process often puts a stranglehold on the specific surface area of the active material and is likely to make perfect coating impossible.[44] On the other hand, although highly porous carbon/LVP heterostructures could generally hold large specific surface areas and hence, facilitate the electrode/electrolyte contacts, these structures inevitably yield low tap density and therefore low volumetric/gravimetric energy density, an essential consideration for industrialization.[178,180,190] In view of all these an ideal composite structure for LVP/C should therefore primarily consist of reasonably sized LVP crystallites to ensure high tap density and integrated with a secondary nano-architectured carbon coating to assure stable solid electrolyte interface (SEI).

Inspired by the above discussions, we would like to contribute here in this chapter a rational engineering of LVP/carbon micro-nano composite as a pragmatic solution for positive electrode in lithium ion batteries. Superior cathode material was obtained by making porous carbon nanoflakes grown erectly on well-crystallized LVP microrods, namely, a completely new style “core-shell” structure. In view of its facility in terms of facile synthesis and rational structure, our method is noticeably more effective than other methods, i.e. by either directly coating active materials with thin carbon layers or simply enwrapping active materials into carbon networks. The power of our designing was grounded on the hierarchical porosity derived from three-dimensionally entangled porous carbon nanoflakes in “shell” part, together with excellent manageability and high tap density stemmed from single-crystalline LVP microrods in “core” part. In particular, the highly entangled carbon nanoflakes not only contact with electrolyte effectively to maintain SEI for stable cycling, but also the void volumes between flakes further serve as electrolyte containers for high-rate charging/discharging. It is because of the dual functional carbon nanoflakes and the reasonably sized LVP crystallites that the as-designed composite displayed great improvements in electrochemical characteristics when it is used as the cathode material

2.2 Experimental Section

2.2.1 Synthesis of LVP/C Composite

A facile ball-milling procedure followed by a solid-state carbothermal reduction reaction synthesis route was applied to prepare LVP microrods/carbon nanoflakes composite. Typically, stoichiometric amounts of raw materials including $CH_3COOLi \cdot 2H_2O$ (15 mmol), NH_4VO_3 (10 mmol), $NH_4H_2PO_4 \cdot 2H_2O$ (10 mmol), and sucrose ($C_{12}H_{22}O_{11}$, 17.5 mmol) were homogeneously mixed in ethanol (100 mL) by high-energy planetary ball-milling for 12 h then aged for another 12 h in tanks after operations. After being dried in an electronic oven at 80 °C for 24 h, the gel remains was grounded thoroughly before it was delivered to heating process. To form the LVP/C composite, the gel precursor was first heated (heating rate 5 °C/min) in a tube furnace at 450 °C for 2 h, followed by milling then heated at 850 °C for 12 h. The whole process was protected by a constant argon flow (see following). After cooling (10 °C/min) to room temperature, the products were obtained by collecting the as-heated powder.

Simultaneous thermogravimetric analysis & differential scanning calorimetry (TG-DSC) profile of as-dried gel precursor under protective argon atmosphere is presented in Figure 2.1. A major weight loss segment accompanied by a clear endothermic process took place before 400 °C, suggesting the decomposition of various raw materials. The weight loss continued until about 750 °C together with a series of evident exothermic phenomena, implying the end of carbothermal reaction beyond 750 °C. In this case, a decomposition temperature of 450 °C and an annealing temperature of 850 °C were applied in our synthesis process to obtain well-crystallized LVP/C composite.

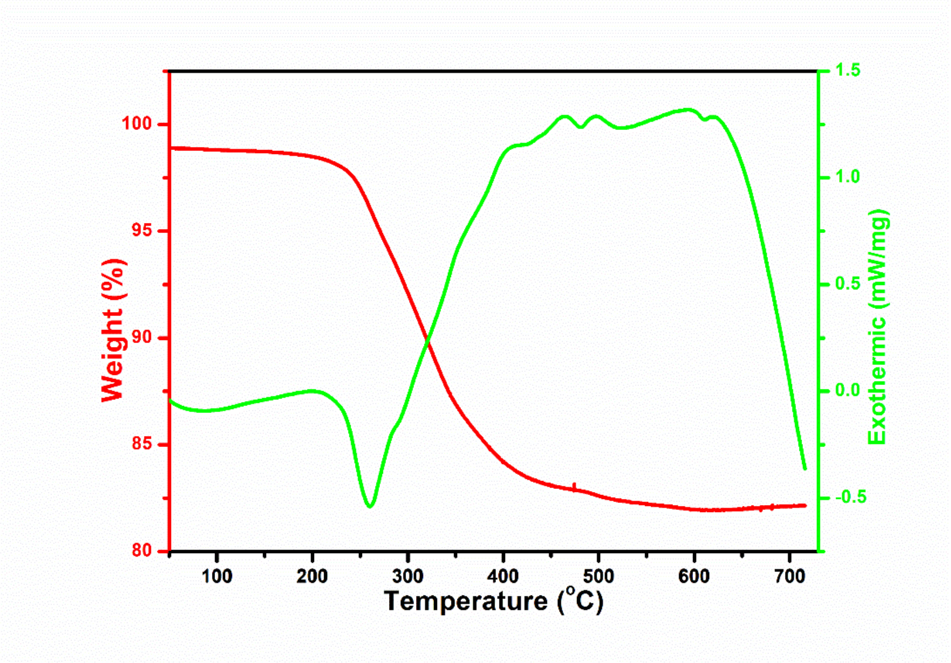

Figure 2.1 TG-DSC profiles of as-dried gel precursor under flowing argon.

2.2.2 Structural Characterization Methods

TG-DSC analysis was performed on a NETZSCH STA 449 C Jupiter® system under flowing argon/oxygen. XRD measurements were taken using a Rigaku SmartLab Intelligent X-ray Diffraction System with filtered Cu Kα radiation (λ = 1.5406 Å, operating at 45 kV and 200 mA). Rietveld refinement of XRD profiles were calculated by an integrated X-ray Powder Diffraction Software Package (PDXL Ver. 1.8.1.0, Rigaku). Raman measurements were taken using a Horiba Jobin Yvon LabRAM HR800 System with a laser wavelength of 480 nm. Scanning electron microscopy (SEM) observations were made on a JEOL 6335F system (operating at

10 kV). Transmission electron microscopy (TEM) images and energy dispersive X-ray spectrums (EDS) were obtained through JEM 2100F (field emission) transmission electron microscopes equipped with an Oxford INCA x-sight EDS Si(Li) detector at an acceleration voltage of 200 kV. Inductively coupled plasma-optical emission spectrometry (ICP-OES) was conducted on a PerkinElmer Optima 7300 V Spectrometers. The nitrogen adsorption and desorption isotherms at 77.3 K were obtained with a Micromeritics ASAP 2020 M+C Physisorption system. The tap density of the $Li_3V_2(PO_4)_3/C$ composite was measured by placing 5 g of sample into a small glass vial before tapping it by hand for 30 minutes until there was no visible volume reduction. The tap density was then determined from the tapped volume and its original mass.[191,192]

2.2.3 Electrochemical Measurements

Electrochemical performance measurements were taken using 2016 coin-type half-cells which were assembled in a glove box filled with protective argon gas. The cathodes of the test cells were made from the active material, conductive Super P, and a poly(vinyl difluoride) binder (HSV900) in a weight ratio of 80 : 10 : 10. The cathode slurry was prepared by thoroughly mixing a N-methyl-2-pyrrolidine solution with the active material, Super P, and a poly(vinyl difluoride) binder. Consequently, the resulting slurry was deposited on aluminum foil (20 μm) and roll-pressed before the entire assembly was dried in a vacuum oven at 120 °C overnight The average loading of the electrode is around 4.0 – 4.5 mg cm^{-2}. Pure lithium foil was used as the anode, and a polypropylene separator (Celgard, 25 μm) was used to separate the cathode and the anode. A 1 M $LiPF_6$ solution in ethylene carbonate and diethyl carbonate mixed at a weight ratio of 1:1 was adopted as electrolyte in the test cells. The cyclic voltammetry performances were tested on the CHI 660B electrochemical workstation. The discharge and charge measurements were made on a Land battery test system in a voltage window of 3-4.3 V at room temperature at different rates.

2.3 Structural Characterizations

The LVP/C composite was synthesized via a facile method, combining both the ball-milling procedure and the solid-state carbothermal reduction reaction as shown in Figure 2.2 (see also the Experimental Section).

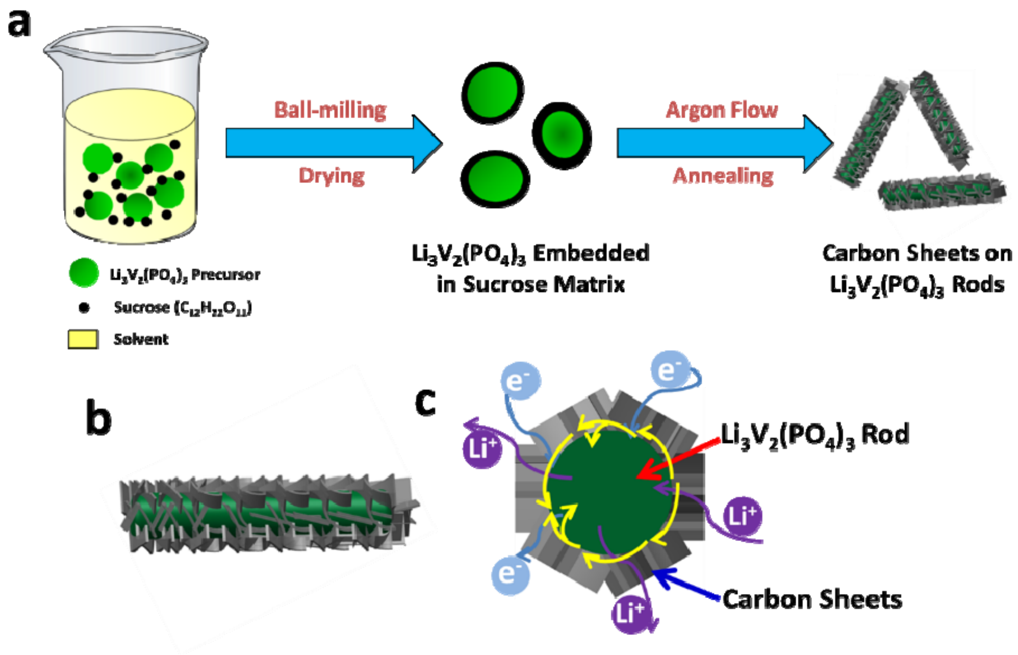

Figure 2.2 Schematic illustration of (a) formation process of carbon nanoflakes on LVP microrods heterostructured composite, (b) sketched morphological features and (c) proposed cross-sectional Li^+/e^- transfer mechanism in LVP/C composite.

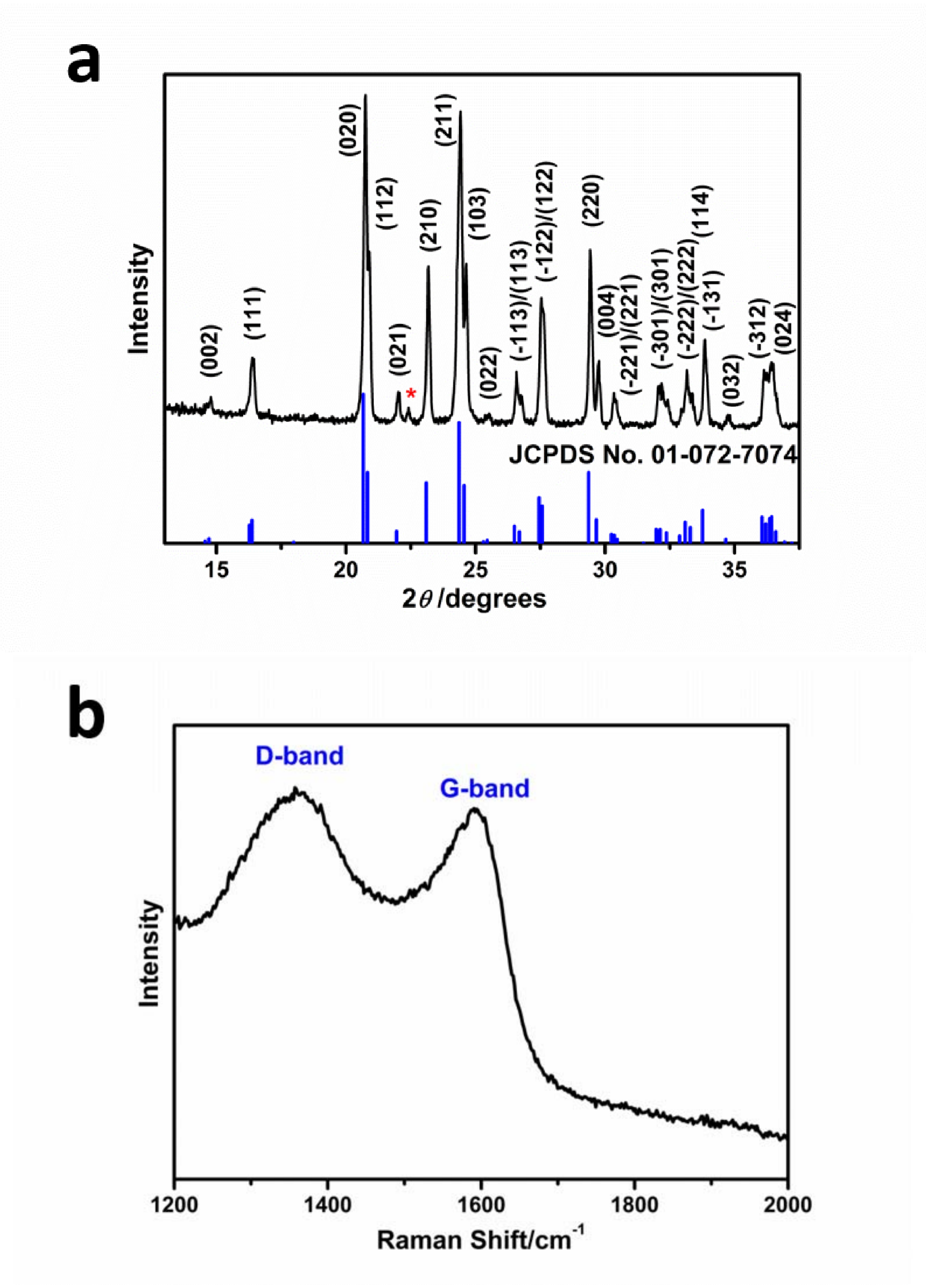

Figure 2.3 (a) XRD profile and (b) Raman spectrum of the as-prepared LVP/C composite.

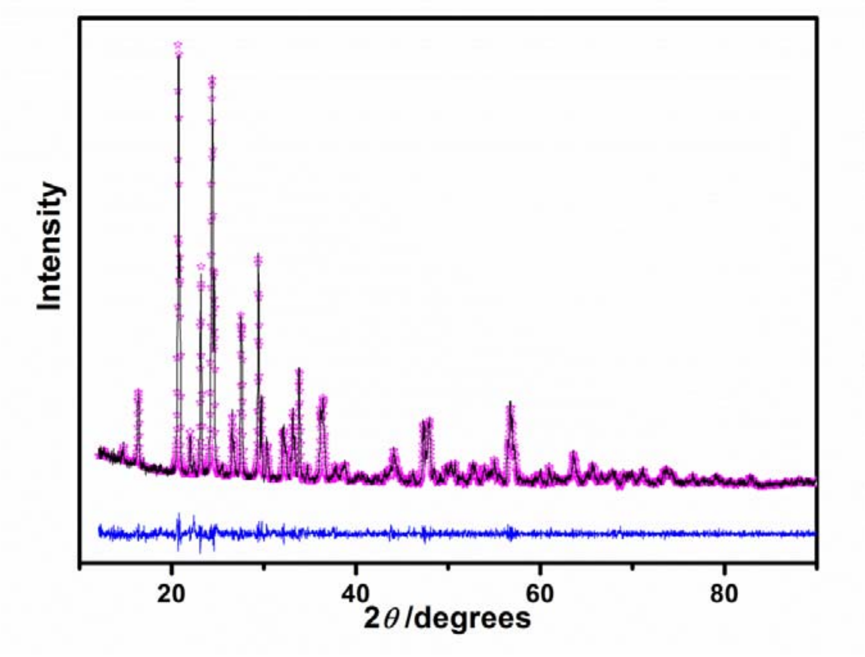

Figure 2.4 Rietveld refinement of XRD profile for LVP/C composite. The observed and calculated intensities were indicated by black line and purple stars, respectively. The bottom blue line represents the fitting residual difference.

Table 2.1 The lattice constants of LVP calculated by a Whole Powder Pattern Fitting (WPPF) method.

a (ang.)	b (ang.)	c (ang.)	α (deg)	β (deg)	γ (deg)
8.6106(5)	8.5951(5)	12.0423(7)	90.000000	90.565(3)	90.000000

Table 2.2 Atomic sites and fractional coordinates of LVP/C:

Atom	**x**	**y**	**z**
Li1	0.202000	0.781000	0.182000
Li2	0.934000	0.312000	0.226000
Li3	0.576000	0.429000	0.207000
V1	0.251030	0.459350	0.109360
V2	0.753070	0.474510	0.390380
P1	0.106900	0.099600	0.158600
P2	0.607800	0.114900	0.355200
P3	0.039500	0.250900	0.488500
O1	0.927600	0.116300	0.146300
O2	0.148200	0.976900	0.240400
O3	0.172700	0.051600	0.034600
O4	0.161800	0.260900	0.184500
O5	0.422900	0.091200	0.326700
O6	0.695900	1.004500	0.284100
O7	0.641600	0.087600	0.477200
O8	0.643700	0.293300	0.314300
O9	0.950900	0.128400	0.569500
O10	0.930700	0.319400	0.402800
O11	0.172500	0.163000	0.431400

O12	0.105900	0.366200	0.576100

* The reliable factors are Rwp=9.22%, Rp=6.94%, and Re=7.77%.

Figure 2.3a & 2.4 shows the powder XRD profile of the as-synthesized LVP/C composite which can be well indexed into the monoclinic space group $P2_1/n$ (a=8.0106 Å, b=8.5951 Å, c=12.0423 Å, and β=90.565° from Rietveld refinement, see Table 2.1 & 2.2). The intense reflection peaks corroborate high crystallinity. A trace of Li_3PO_4 impurity phase was observed (denoted by red star) due to possible loss of vanadium during heat treatment. No obvious peaks corresponding to graphite can be found, implying the carbon content in the sample is not well crystallized. In order to study the nature of the carbon content in the composite, the Raman spectrum was captured and is presented in Figure 2.3b. As can be seen, the characteristic signatures located at ~1360 and ~1600 cm^{-1} are attributed to the D-band (disorder-induced phonon mode) and G-band (E_{2g} vibrations of graphite) of carbon, respectively.[193] These results reveal that the as-synthesized product is composed of LVP crystallites together with partially graphitized carbon.

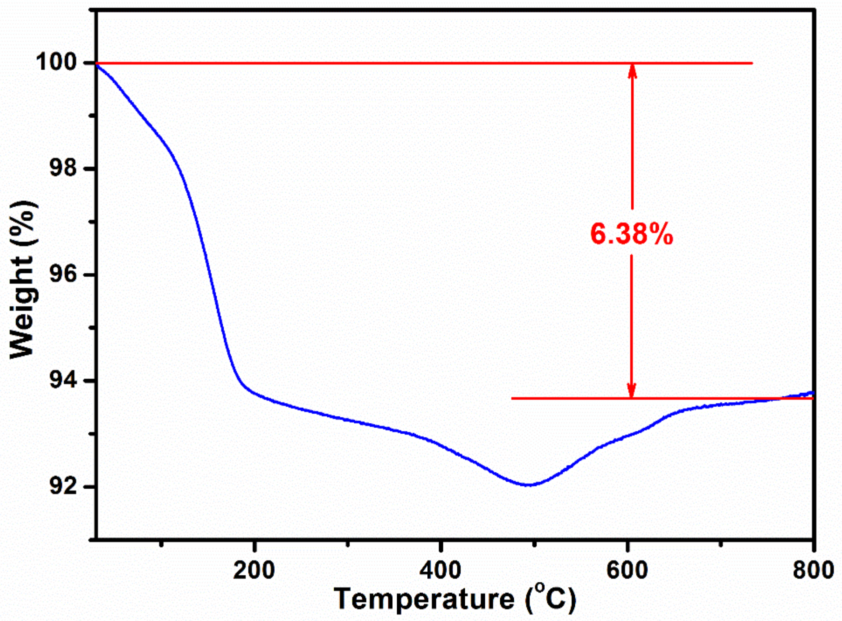

Figure 2.5 Thermogravimetric profile of the LVP/C composite heated in synthetic air.

ICP-OES was employed to disclose the exact elemental composition of the product and the result suggested that the chemical composition of the composite contains 86.33 wt% LVP and 13.67 wt% carbon. Thermogravimetric analysis was also adopted to confirm this result. In order to completely remove the carbon content, the LVP/C composite was heated in synthetic air flow within the temperature range from room temperature to 900 °C. Meanwhile, thermogravimetric profile was recorded as shown in Figure 2.5. The weight loss is a result of the complete removal of carbon and oxidation of vanadium elements in the composite (from V^{3+} to V^{5+}). Thus the carbon content is estimated to be about 13.19% according to the reported method,[194] and is consistent with the ICP-OES result.

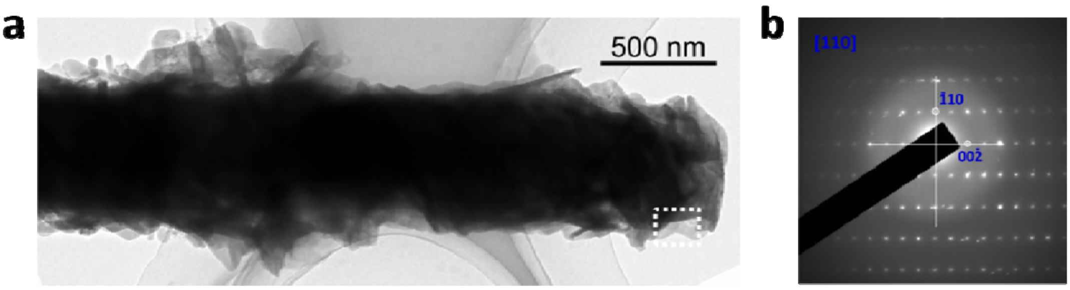

Figure 2.6 Typical (a) TEM micrograph, (b) the corresponding SAED pattern from an isolated LVP/C microrods.

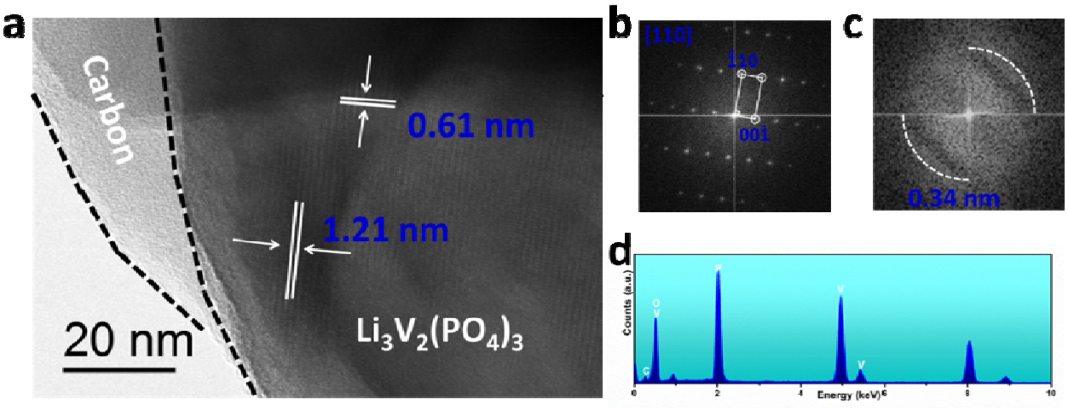

Figure 2.7 (a) HRTEM image of the LVP/C composite. (b) and (c) are associated FFT patterns from the LVP part and the carbon part in (a), respectively. (d) The EDS profile acquired from the LVP/C composite. (a) – (d) are all acquired from an unsupported region as guided by the white dashed box in Figure 2.6(a).

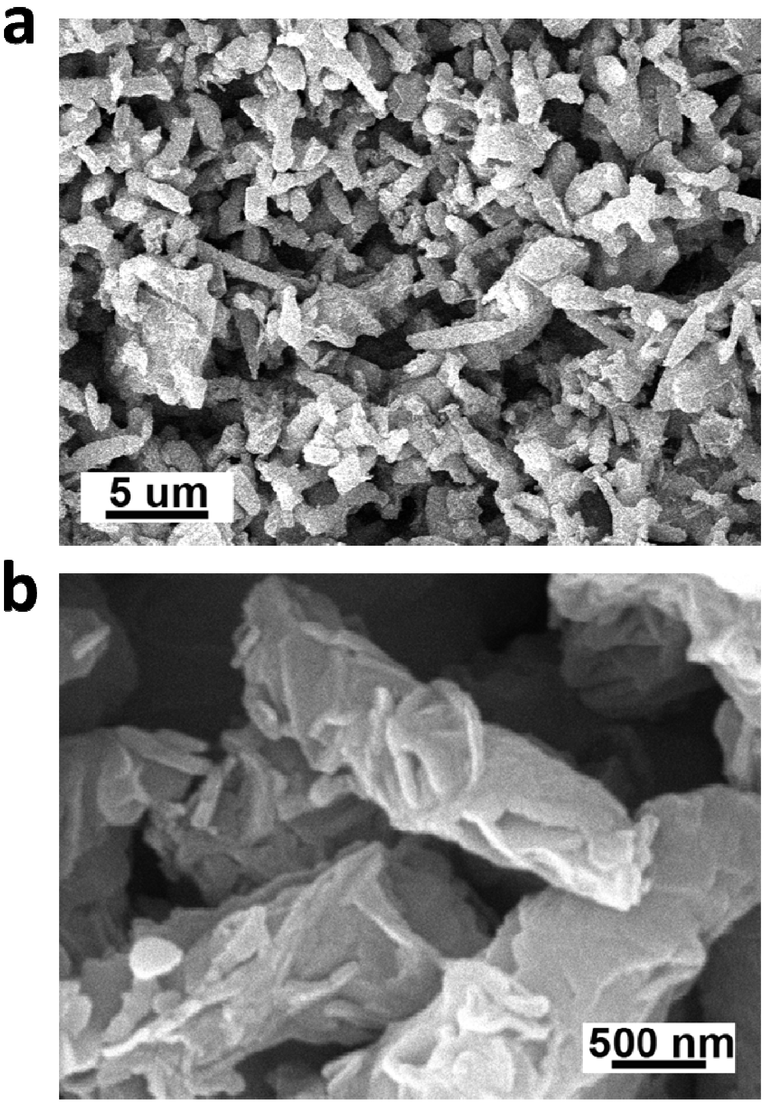

Figure 2.8 Typical (a) low-magnification and (b) high-magnification SEM micrographs of LVP/C composite.

The morphological and microstructural information of as-synthesized product was then characterized by high-resolution transmission electron microscopy (HRTEM) and SEM. As shown in the TEM images in Figure 2.6a and 2.7a, the nearlyorthogonal 1.21/0.61 nm lattice fringes correspond to the $(00\bar{1})/(\bar{1}10)$ planes of monoclinic LVP, respectively. These results clearly show that the product is made up of a LVP microrod acting as the "core" part with the many porous carbon nanoflakes randomly standing on it as "shell" part (Figure 2.2). The associated selected area electron diffraction (SAED) pattern in Figure 2.6b is indexed to be projected along [110] zone axis from the monoclinic LVP (note: the blurry intensity of Figure 2.6b is caused by the diffuse reflection from the non-uniform carbon layer), and both fast Fourier transform (FFT) patterns as shown in Figure 2.7b and 2.7c are also well assigned to $Li_3V_2(PO_4)_3$ and weak-crystallized carbon, respectively (arc of 0.34 nm in diameter in Figure 2.7c corresponds to d-spacing of graphite (002) planes). Repeated observations among different LVP rods proved that they all belong to a single crystalline nature with the same preferential growth direction along the direction perpendicular to (001) plane as revealed in Figure 2.6b. The EDS in Figure 2.7d further verifies a rough molar ratio of 2:3 for vanadium and phosphorus elements in the composite, in accordance with its chemical formula. Combining these data with SEM micrographs in Figure 2.8, it can be concluded that the product is of high yield and has high uniformity made up of well-dispersed LVP microrods (300-500 nm in diameter and 4-5 μm in length) integrated with irregular porous carbon nanoflakes (tens of nanometer in thickness and hundreds of nanometer in height) densely grown on the microrods. These anisotropic-shaped microsized LVP rods and the irregular entangled carbon flakes on these rods' surfaces could effectively prohibit the aggregation of the LVP/C particles (Figure 2.8a & 2.8b); thus, making this composite suitable for mixing with conductive additives or binders during the process of manufacturing real batteries. A tap density of as high as 1.4 g cm^{-3} was also reported from our composite structure, a figure far higher than that of previous micro-/nanocrystallites of LVP/C composites (typically reported as 0.6-0.9 g cm^{-3} for microcrystallites and 0.3-0.6 g cm^{-3} for nanocrystallites) and almost comparable with that of pure LVP microparticles from conversional solid-state reactions.[174,190,195]

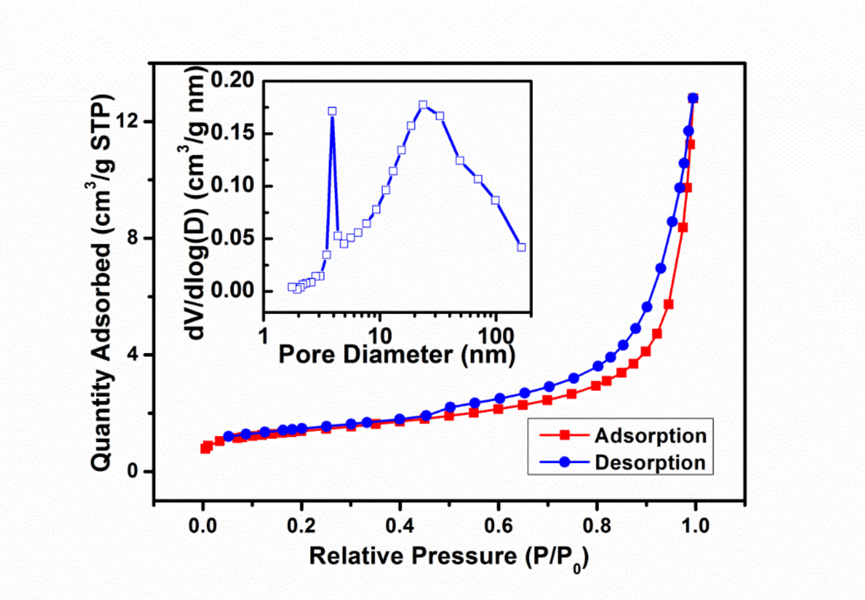

Figure 2.9 Nitrogen adsorption/desorption isotherms of the LVP/C composite. Inset is the pore-size distribution plot calculated by the BJH formula in the desorption branch isotherm.

In order to further examine the pore structure of the as-synthesized composite, a nitrogen isothermal-adsorption technique was employed. Figure 2.9 shows the results from adsorption-desorption isotherms and the corresponding Barrett-Joyner-

Halenda (BJH) pore-size distribution curves of the sample. Typical hysteresis of nanoporous system can be identified within the relative pressure range of 0.5~1.0 according to the International Union of Pure and Applied Chemistry Regulation,[196] resulting in a comparable surface area to that of conventional carbon coated-LVP materials.[197] The BJH pore-size distribution, as shown in the inset, suggests that the composite has mesopores of about 3.9 nm and 23.6 nm in diameter. By comparing analysis of Figure 2.9 and TEM investigation (Figure 2.6a & 2.6c), it can be concluded that these two kinds of pores can be respectively attributed to porous carbon flakes themselves and the void spaces between flakes.

2.4 Electrochemical Performances

Take the above into accounts, our LVP/C composite is expected to perform well as cathode material in lithium cells. To verify this assumption, the electrochemical characteristics of our composite with respect to Li^+ insertion/extraction were thoroughly evaluated at room temperature from a coin-type half-cell by using Li foil as anode, and the results are presented in Figure 2.10, 2.11 & 2.12. The findings show that the cyclic voltammetry (CV) curve for the first cycle at a scanning rate of 0.1 mV s^{-1} (see Figure 2.10) displays a typical behavior of LVP-based electrode containing three pairs of oxidation/reduction peaks in the potential range of 3.0-4.3 V.[175] As can be seen, three pairs of oxidation and reduction peaks appear in the first cycle. The first two anodic peaks at 3.64 and 3.72 V agreed with the removal of first Li^+ through two steps, corresponding to an ordered $Li_{2.5}V_2(PO_4)_3$ intermediate phase and a $Li_2V_2(PO_4)_3$ phase.[175,180] Then the second Li^+ was extracted by one step at 4.16 V to form $LiV_2(PO_4)_3$. The three cathodic peaks located at 3.46, 3.54, and 3.89 V are associated with the reinsertion of the two Li^+, resulting from the $V^{4+}/^{V3+}$ redox couple.

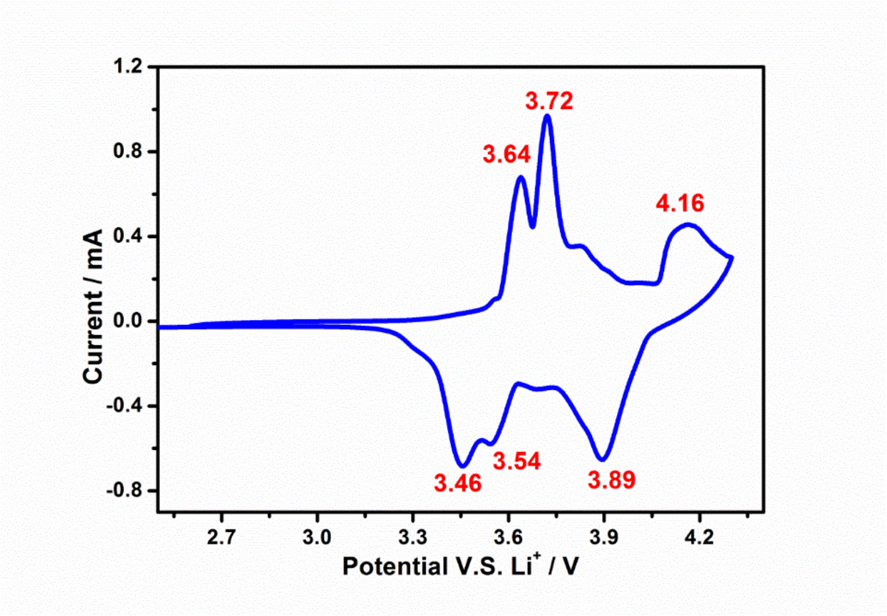

Figure 2.10 Cyclic voltammetry curve of synthesized LVP/C composite for the first cycle at a scan rate of 0.1 mV/s in the cell potential range of 2.5-4.3 V.

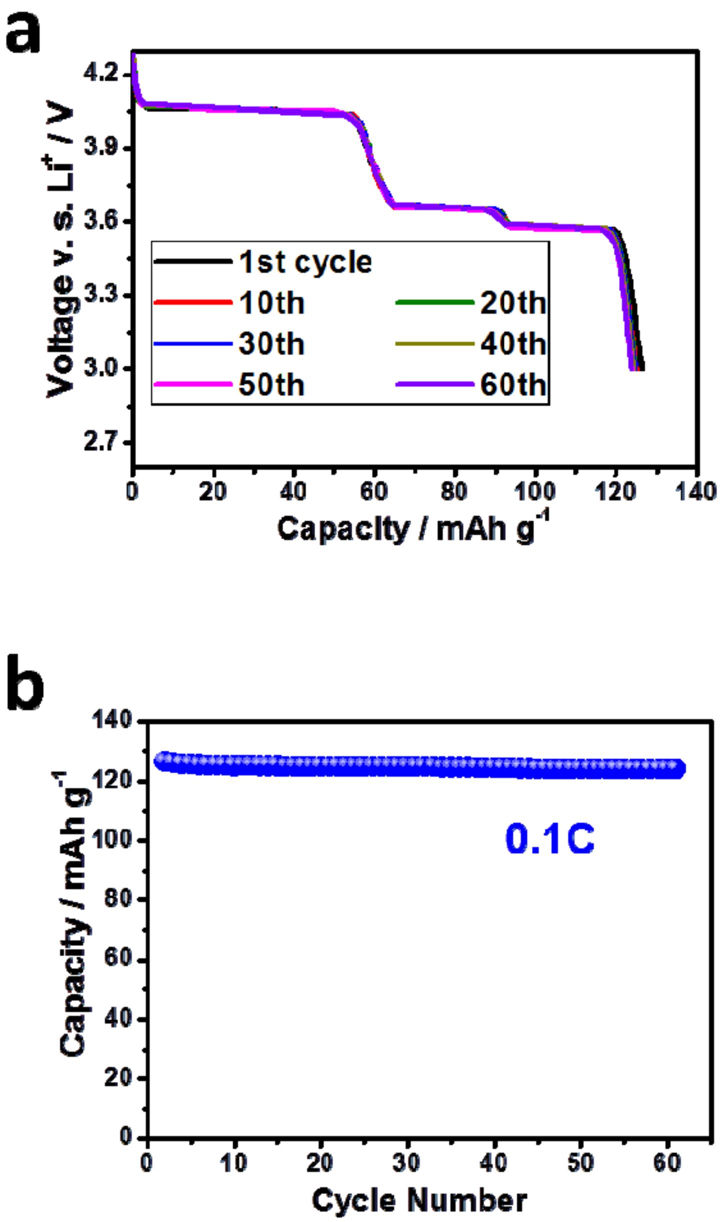

Figure 2.11 Electrochemical characteristics of LVP/C composite tested between 3.0 V and 4.3 V at room temperature. (a) Discharge voltage profiles plotted of the 1st, 10th, 20th, 30th, 40th, 50th and 60th cycles at a rate of 0.1. (b) Cycling performance of the composite at rate of 0.1C.

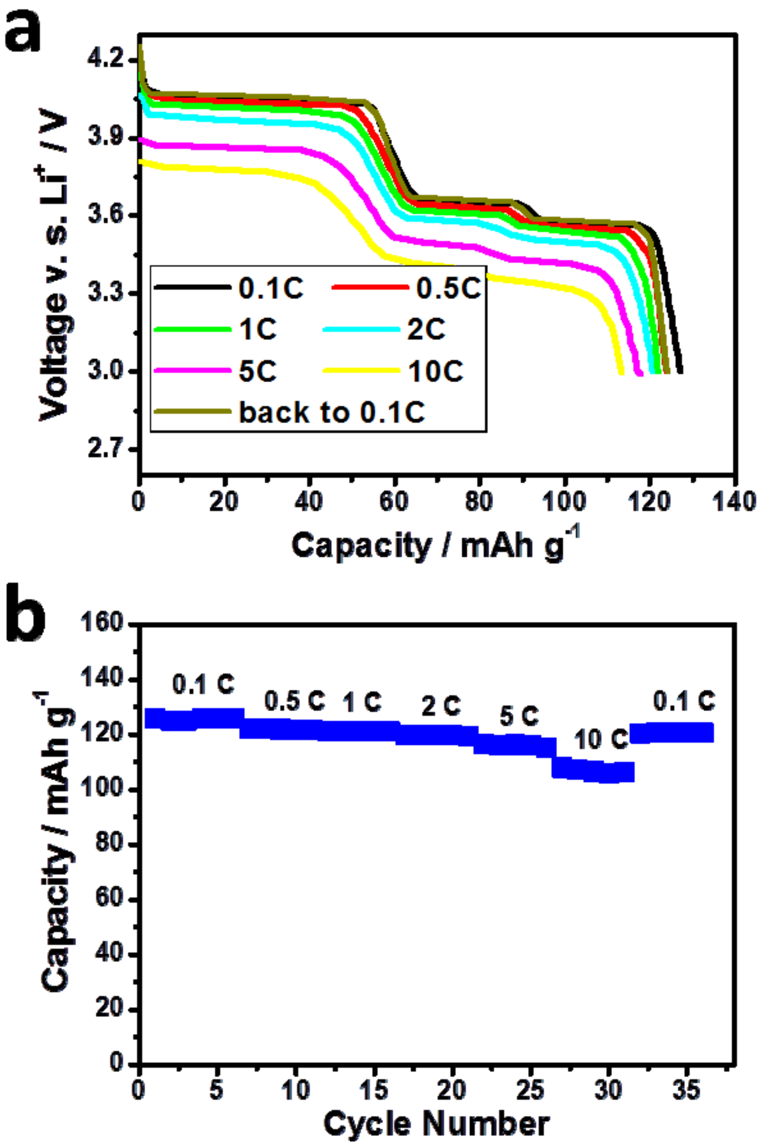

Figure 2.12 Electrochemical characteristics of LVP/C composite tested between 3.0 V and 4.3 V at room temperature. (a) Rate capabilities of the composite with increasing rates from 0.1C, 0.5C, 1C, 2C, 5C and 10C at first cycle, then back to 0.1C. (b) Galvanostatic cycling behavior at various rates from 0.1C to 10C.

Subsequently, the representative discharge voltage profiles of the LVP/C cathode at a current rate of 0.1C (1C = 1 h^{-1} × 133 mAh g^{-1} = 133 mA g^{-1}) in the voltage window of 3.0-4.3 V were recorded and presented in Figure 2.11a. It can be seen that three clear plateaus were located at around 3.5, 3.6 and 3.9 V in each profile and are in good agreement with the CV results. The battery exhibited a discharge capacity of 126.5, 125.2, 125.0, 124.8, 124.4, 124.1, 124.0 mA h g^{-1} for cycles 1, 10, 20, 30, 40, 50, 60, respectively. The cycling performance tested at rate of 0.1C and in the potential range of 3.0-4.3 V is shown in Figure 2.11b. The results show a superior cycling stability with a final specific capacity retention of 98% (0.1C after 60 cycles). To fully examine the electrochemical performance of our LVP/C cathode at higher current rates, the as-fabricated cells were then cycled at different rates ranging from 0.1C to 10C (Figure 2.12). As shown in Figure 2.12a, the LVP/C cathode delivers an initial discharge capacity of 127.1 (0.1C), 123.8 (0.5C), 122.0 (1C), 120.6 (2C), 117.9 (5C), 113.4 (10C), and then back to 124.1 mA h g^{-1} (0.1C), respectively. Surprisingly, plateaus remain visible at high discharging current rates. Figure 2.12b shows the overall rate capability test of 0.1C–10C–0.1C, revealing a significant and reversible rate performance.

Among repeated observations, our findings reflect that the LVP/C cathode possess both outstanding cycling stability and a good rate capability, and its performance is almost comparable with recently reported LVP/Carbon or LVP/Graphene cathodes.[180–182,187] Such impressive electrochemical performance could be attributed to several factors (Figure 2.2c). Firstly, the single-crystalline nature of LVP microrods plays an important role. In contrast to polycrystalline samples, cathode materials of single crystallinity generally show higher structural stability and contain fewer defects, and hence possess better reversibility and capability.[57] Secondly, the conductive carbon coating on the LVP microrods greatly improves the electronic conductivity of the as-fabricated cathode, resulting in charge-transfer resistance reduction and therefore better electrochemical performance. The carbon shell also effectively restricts each LVP microrod during expansion and contraction caused by insertion/removal of lithium ions, bringing extra structural stability among repeating charge/discharge processes.[44] Furthermore, the featured hierarchical mesoporous-macroporous structure originated from entangled carbon nanoflakes could decisively enlarge the contact areas between electrode and electrolyte, and thus increase the active sites for lithium ions and facilitate the migration of Li^+/e^- to reach each individual LVP/C crystallite.[170] It should be noted that in comparison of nanosized counterparts of LVP cathodes,[174,181,186,197] although the gravimetric capacity or rate capability of the as-synthesized LVP/C composite has not improved greatly, its ultra-high tap density should produce a much higher volumetric capacity than that in previous works and thus making it much more suitable and practical for marketing applications, such as thinner notebooks and smaller electronics.

2.5 Summary

In summary, we succeeded in synthesizing homogeneous LVP microrods with three-dimensionally entangled carbon nanoflakes on their surfaces at a high yield via a facile ball-milling process with carbothermal reaction. The battery based on this LVP/C cathode exhibited high cycling stability and high rate capability, two unique microstructural qualities of LVP/C hierarchical composite. In addition, the as-synthesized LVP/C composite possesses remarkably high tap density, leading to a substantial improvement in this promising material's volumetric capacity. It is worth noting that the methodology adopted in this work could be easily extended to other lithiated metal phosphates such as $LiMnPO_4$ and $LiFePO_4$, and is ready to be scaled up for industrial production.

CHAPTER 3 HIERARCHICALLY POROUS CARBON COATING ON LVP NANOSPHERES FOR STABLE CATHODE

On the basis of the previous study, we further optimize LVP/C composite for practical applications in LIBs, especially for high-power scenarios. Another hierarchical nanocomposite, LVP/C core-shell nanospheres embedded in porous carbon frameworks, is designed and realized. The novel nanocomposite exhibits significantly improved electrochemical performance, such as long-term stability upon cycling, superior rate capability, and high discharge capacity when compared to previous LVP-based materials. Furthermore, the exceptional cycle stability and power capability of the nanocomposite is directly attributed to its unique nanoscale architecture by our detailed microstructural analysis. Therefore, we believe that our findings suggest a potential candidate for future 4 V-class batteries.

3.1 Introduction

LIBs have proved themselves one of the most successful energy storage systems for a wide range of modern applications, including electrical vehicles and consumer electronics, resulting from their high energy density, high power, and long lifespan.[1,2,56] At present, a plethora of efforts are unprecedentedly encouraged and supported by a majority of nations on seeking of new-fashioned cathode materials, which are of critical importance in determining the whole battery performance.[55] Amongst the prospective cathode materials for next-generation LIBs, LVP with Na super-ionic conductor (NASICON) framework exhibits its extra fascination due to the excellent structural stability brought by a three-dimensional polyanion $(PO_4)^{3-}$ framework as well as a high redox potential (average potential of ~4 V vs. Li^+) compared with that of well-developed LFP (~3.4 V).[102,176,180,186,198] Notably, LVP is one of only a few 4 V-class polyanion-based cathode materials,[46,58,182] and there is such an increasing pursuit of 4 V-class electrode materials to replace the current LCO cathode across the world due to the serious safety, toxicity and price concerns on the latter. However, the charming vista of LVP applications is significantly obstructed by its inferior electronic conductivity (σ, 2.0 x 10^{-8} S cm^{-1}) arising from the inherently separated VO_6 octahedral arrangement in the crystal structure.[176,180,198] Consequently, in practice, LVP-based LIBs usually deliver limited high-rate capability and undergo severe capacity fading among repeated charging/discharging cycles.

Current strategies to conquer the above issue and therefore to enhance the electrochemical performance of polyanion-based materials mainly focus on particle size reduction and conductive surface coating. [43,46,56] Size reduction to nanosize dimension simultaneously shortens the distance for Li^+ transport across the particulate electrode and increases the electronic contact area between the electrode and the electrolyte, leading to fully access of the theoretical capacity plus a long cycle life.[199] Nevertheless, nanosized materials are generally synthesized via low-temperature methods, which results in a relatively poor quality of crystallinity and hence reduces the electrochemical stability.[43] Moreover, owing to the high surface energy, nanomaterials are always favored to be self-aggregated in ordinary batteries, yielding a giant surface area loss, therefore remaining a remarkable challenge to fully utilize the advantages of nanosized active materials. Alternatively, conductive coating (carbon, RuO_2, graphene, conductive polymers, etc.) on active material is also a feasible technique to improve its cathodic performance by virtue of modifying the surface chemistry and constructing efficient electron pathways.[44,102,197] Among them, a vast majority of work has been concentrated on carbon coating due to its unique economical and practical advantages (good electrical conductivity, excellent chemical/electrochemical stability, low cost, etc.) which was also frequently applied on LVP.[102,174,180–182,198,200–203] An ideal core-shell carbon coating (i.e. to homogeneously distribute a thin carbon layer on the surface of the host material particles) has repeatedly proved its effective enhancement to the electrochemical performance of cathode materials, but an inevitable drawback associated with such a process is the difficulty to achieve perfect coating and the costly coating process, which seriously hinders its potential of scalable manufacturing.[44]

To mitigate the above-mentioned challenges, we are strongly expecting a rational design of LVP-based cathode material complying with several aspects, which include: i) fine-sized and highly-crystallized LVP particles to guarantee stable cathodic performance. ii) A conductive coating on LVP particles to improve its electronic conductivity and to prevent structure degradation upon cycling. iii) A conductive matrix to ensure dispersive distribution (to avoid self-aggregation) of LVP particles and to offer three-dimensional (3D) continuous electron pathway. iv) Sufficient porosity in the matrix to benefit electrolyte infiltration. v) A facile synthesizing approach is preferred for its future large-scale applications. However, to the best of our knowledge, the attractive cathode material for LIBs satisfying the above aspects has never been reported before. Herein, we make our contribution in this chapter that such a novel LVP-carbon composite material is created by combining the advantages of hierarchical porous carbon and nanometer-sized $Li_3V_2(PO_4)_3$ active particles. Superior hybrid material is obtained by incorporating conformally carbon-coated, well-crystallized LVP nanospheres (LVP/C core-shell nanospheres) inside micrometer-sized 3D porous carbon networks. This hierarchical nanostructured LVP/C (hereafter abbreviated as HN-LVP@C) configuration smartly unites multiple advantageous features, including highly-crystallized and single-crystalline LVP nanospheres to stabilize the electrochemical cycling, a 3D well-connected conducting framework, a reasonable meso-macroporous microstructure to facilitate the electrolyte infiltration, and abundant porous spaces for accommodation of volume expansion during the electrode charge/discharge. The HN-LVP@C nanocomposite derived a discharge capacity of ca. 130 mAh g^{-1}, approaching its theoretical value (133 mAh g^{-1}). Furthermore, at high current rate (10C), it displayed impressive long cycle life and remarkable capacity retention (90% after 1200 cycles) together with high Coulombic efficiency (> 99%).

3.2 Experimental Section

3.2.1 Synthesis of HN-LVP@C Nanocomposite

A facile hydrothermal reaction followed by a solid-state carbothermal reduction synthesis was adopted here in this work. Typically, a V_2O_5 powder (4 mmol) and 40 ml H_2O were mixed under vigorous magnetic stirring at room temperature, and then 10 ml 30% H_2O_2 was slowly dropped to this mixture and kept continuously stirring for 30 min to form a transparent burgundy solution. After that, $CH_3COOLi \cdot 2H_2O$ (12 mmol), $NH_4H_2PO_4 \cdot 2H_2O$ (12 mmol) and polyethylene glycol (PEG-600, 3 ml) were then sequentially added to the solution, forming a light-yellow solution. Consequently, the resultant solution was adjusted to a volume of 80 ml by H_2O before transferred to a 100 ml autoclave. The autoclave was sealed, kept at 200 °C for 4 days, and then cooled down to room temperature naturally. The resulting brown gel-like remainder was dried in an electronic oven at 100 °C overnight, and then grounded thoroughly before it was delivered to heating process.

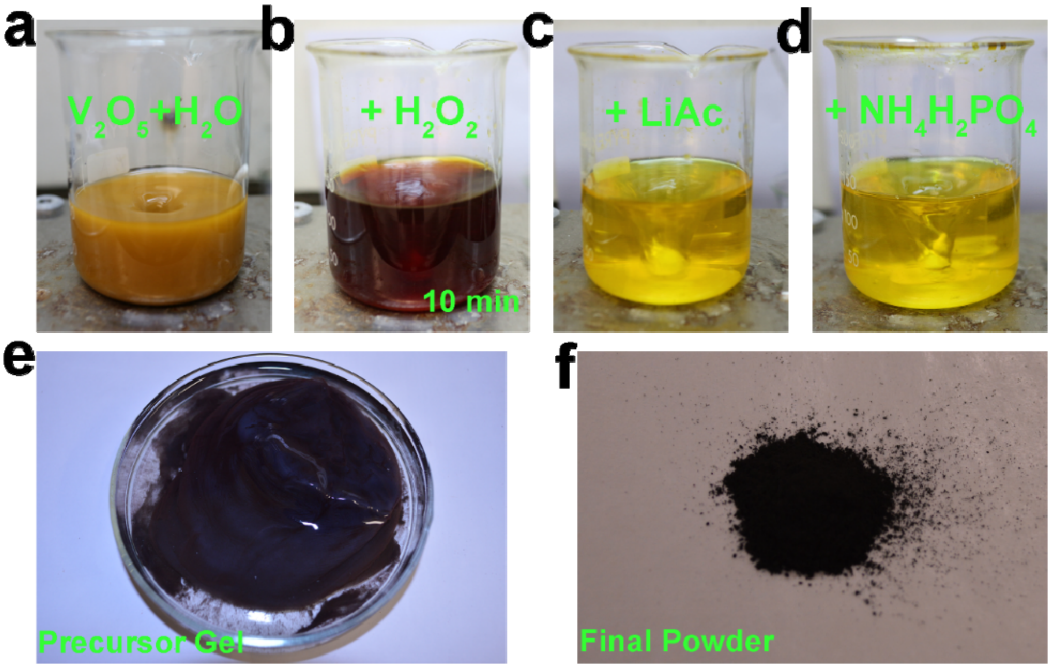

Figure 3.1 Digital images of the color evolution during the whole synthesis process.

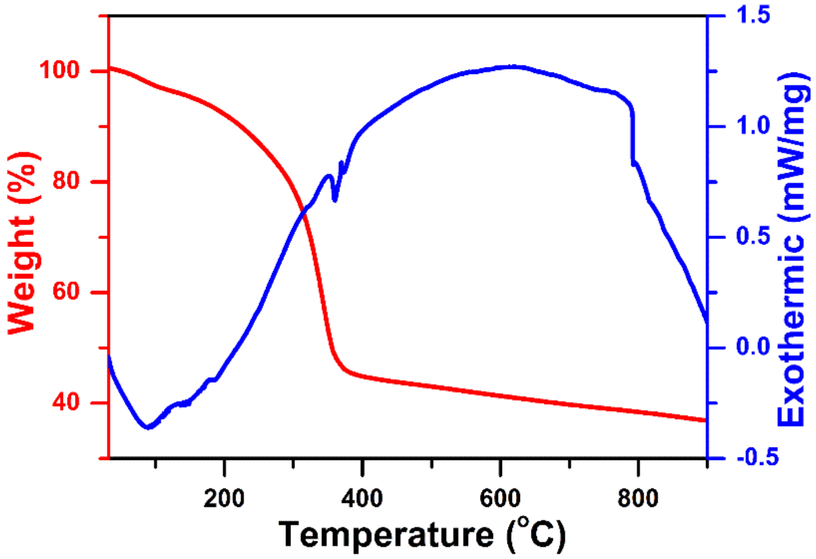

Figure 3.2 TG-DSC profiles of as-dried gel precursor under flowing argon.

Simultaneous TG-DSC profiles of as-dried gel precursor under protective argon atmosphere were utilized for determining the heating conditions, as shown in Figure 3.2. A major weight loss segment accompanied by an obvious endothermic process took place before 400 ^{o}C, suggesting the decomposition of the precursor. The weight loss didn't stop until about 800 ^{o}C together with a series of evident exothermic peaks, indicating the ending of carbothermal reaction beyond 800 ^{o}C. Upon this situation, a decomposition temperature of 450 ^{o}C and an annealing temperature of 850 ^{o}C were adopted in our synthesis process to obtain well-crystallized HN-LVP@C nanocomposite. Therefore, the precursor was first heated (heating rate 5 °C/min) in a tube furnace at 450 °C for 2 h, followed by milling then heated at 850 °C for 12 h. The whole process was protected by a constant argon flow. After cooling (10 °C/min) to room temperature, the products were obtained by collecting the as-heated powder (The whole process is recorded as image sequence in Figure 3.1).

3.2.2 Structural Characterization Methods

TG-DSC analysis was performed on a NETZSCH STA 449 C Jupiter® system under flowing argon. Powder XRD measurement was taken using a Rigaku SmartLab Intelligent X-ray Diffraction System with filtered Cu Kα radiation (λ = 1.5406 Å, operating at 45 kV and 200 mA). Rietveld refinement of XRD profile was calculated by an integrated X-ray Powder Diffraction Software Package (PDXL Ver. 1.8.1.0, Rigaku). Raman measurement was taken using a Horiba Jobin Yvon LabRAM HR System with a laser wavelength of 488 nm. X-ray photoelectron spectroscopy (XPS) measurement was performed on an ESCALab 250 (Thermo-VG Scientific) X-ray photoelectron spectrometer with an Al Kα excitation source. ICP-OES was conducted on a PerkinElmer Optima 7300 DV Spectrometer. TEM images and EDS were obtained through a JEM 2100F (field emission) scanning transmission electron microscope equipped with an Oxford INCA x-sight EDS Si(Li) detector at an acceleration voltage of 200 kV. SEM observations were made on a JEOL 6335F system (operating at 5 ~ 10 kV). The nitrogen adsorption and desorption isotherms at 77.3 K were obtained with a Micromeritics TriStar II 3020 M Physisorption system.

3.2.3 Electrochemical Measurements

Electrochemical performance measurements were taken using 2016 coin-type half-cells which were assembled in a glove box filled with protective argon gas (M. Braun inert gas systems Co. Ltd., Germany). The cathodes of the test cells were made from the active material, conductive Super P, and a poly(vinyl difluoride) binder in a weight ratio of 80 : 10 : 10. The cathode slurry was prepared by thoroughly mixing a N-methyl-2-pyrrolidine solution with the active material, Super P, and a poly(vinyl difluoride) binder. Consequently, the resulting slurry was deposited on aluminum foil (20 μm) and pressed before the entire assembly was dried in a vacuum oven at 120 °C overnight. The average loading of the electrode is around 3.8 - 5.1 mg cm^{-2}. A pure lithium foil was used as the anode, and a polypropylene separator (Celgard 2400) was used to separate the cathode and the anode. A 1 M $LiPF_6$ solution in ethylene carbonate and diethyl carbonate mixed at a weight ratio of 1:1 was adopted as electrolyte in the test cells. The electrochemical impedance spectroscopy (EIS) and CV performances were tested using a Potentiostat/Galvanostat (EG&G Princeton Applied Research 273A). The discharge and charge measurements were made on a Land battery test system (Wuhan Land Electronic Co., China) in a voltage window of 3.0 - 4.3 V at room temperature at different rates.

3.3 Structural Characterizations

The fabrication process and detailed structure of HN-LVP@C nanocomposite is schematically illustrated in Figure 3.3. The HN-LVP@C nanocomposite was synthesized via a surfactant-assisted hydrothermal reaction plus a carbothermal reduction technique. Polyethylene glycol (PEG), a non-ionic surfactant, was adopted as surfactant in hydrothermal reaction,[204] and subsequently acted as both reducing agent and carbon source in the carbothermal reaction. The hydrothermal treatment generated a PEG-capped LVP precursor, leaving some PEG content redundant due to its highly excessive amount in the start solution (Figure 3.4). Consequently, in the following carbothermal reaction, LVP precursor crystallized into nanosphered “core” and the surface-adsorbed PEG carbonized into carbon “shell”; meanwhile, the redundant PEG formed surrounding 3D porous carbon matrix (The carbonization of chaos PEG chains led to highly porous carbon networks.) to give the final HN-LVP@C nanocomposite. It is of noting that our hybrid synthesis route efficiently coupled the advantages of classical hydrothermal and carbothermal reactions. In our case, the growth of LVP crystal was significantly restricted by the carbon shell, resulting in nanosized spheres with high crystallinity, which is impossible to obtain from either low-temperature hydrothermal approaches or ordinary solid-state reactions.

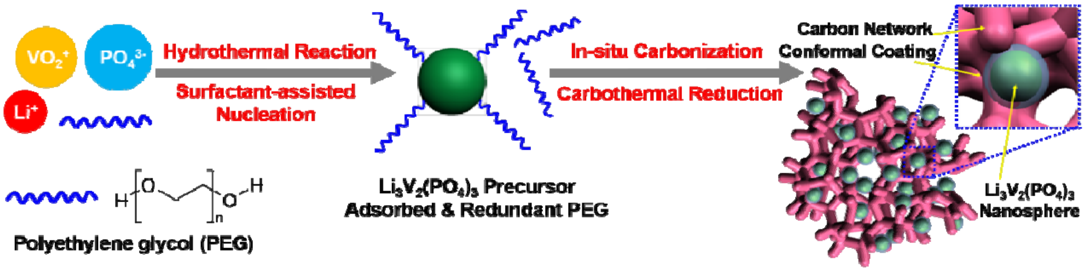

Figure 3.3 Schematic illustration of the formation of HN-LVP@C nanocomposite.

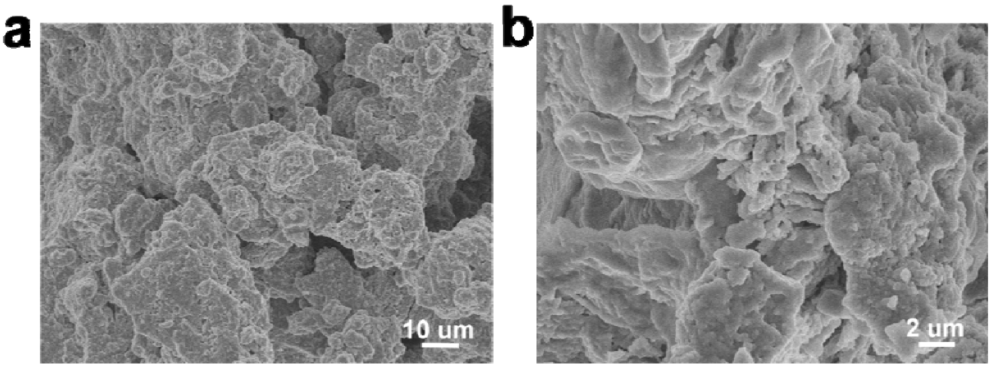

Figure 3.4 SEM images of as-dried gel precursor at (a) low and (b) high magnifications.

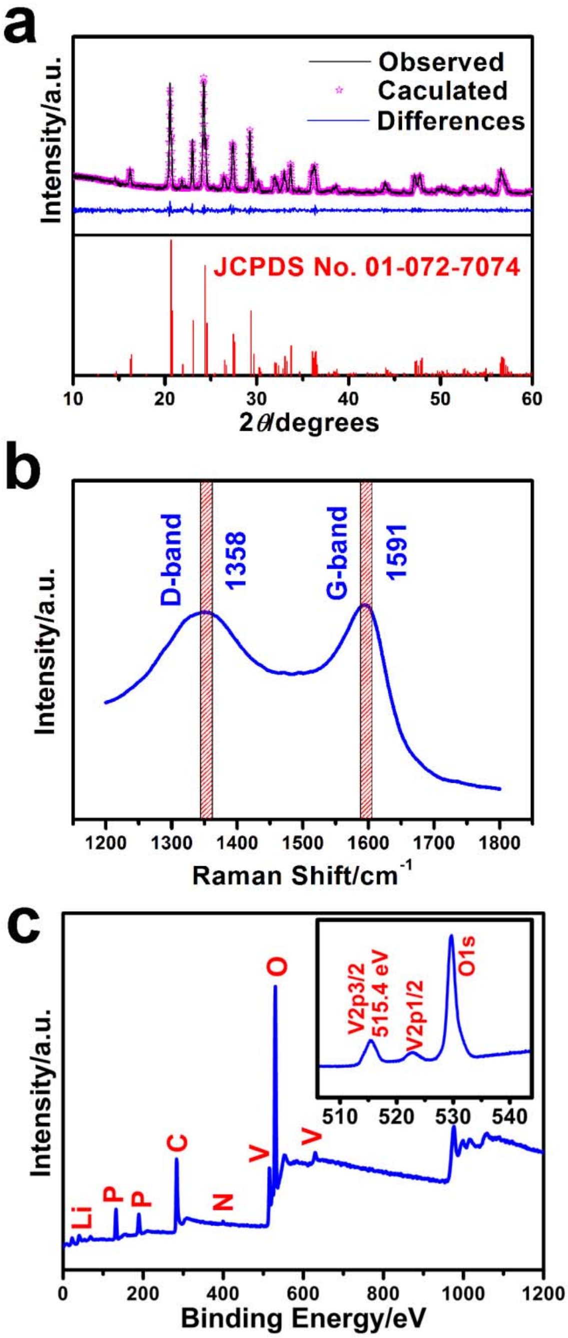

Figure 3.5 (a) Rietveld refined XRD pattern, (b) Raman spectrum, and (c) Survey XPS spectrum (inset: enlarged V 2p and O 1s region) of HN-LVP@C nanocomposite.

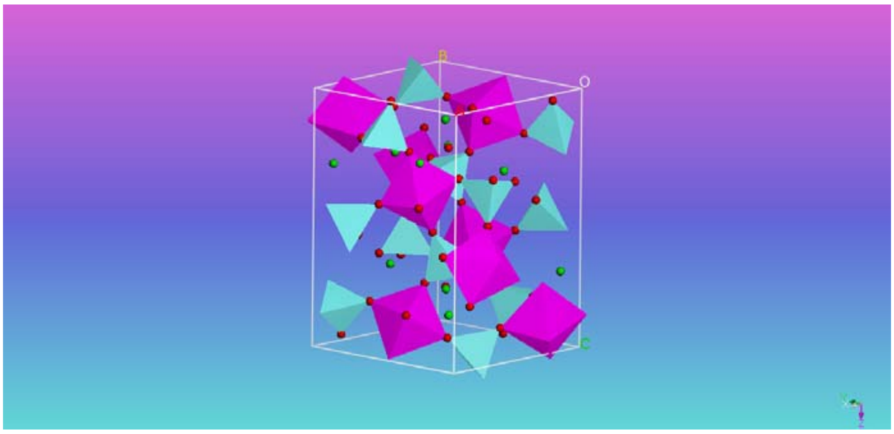

Figure 3.6 Sketch of the crystal structure of LVP based on the data from Rietveld refinement. Lithium atoms: green spheres; oxygen atoms: red spheres; phosphate tetrahedrons (PO_4): cyan blocks; and vanadium oxide octahedrons (VO_6): pink blocks.

Figure 3.5a shows the Rietveld refinement of the XRD data of HN-LVP@C nanocomposite. All visible peaks in the spectrum can be readily assigned to the monoclinic $Li_3V_2(PO_4)_3$ (JCPDS Card No. 01-072-7074, space group $P2_1/n$(14)), and the intense reflection peaks corroborate its high crystallinity. The calculated profile matches well with the observed one, with refined lattice parameters as a = 8.648 Å, b = 8.634 Å, c= 12.096 Å, and β = 90.609° (reliable factors R_{wp} = 7.44%, and S = 1.173). The average crystallite size of LVP is ~50 nm, estimated from the major diffraction peaks by Scherrer's formula. LVP possesses a 3D framework consisting of slightly distorted metal octahedral and phosphorous tetrahedral linked via common apical oxygen atoms, therefore there are three independent lithium sites as indicated by green spheres in Figure 3.6.[175,176] This unique arrangement enables 3D pathways for lithiation/delithiation, which is obviously better than that of $LiFePO_4$ structure where only one dimensional pathway is permitted.[205] However, the separated arrangement of transition metal cations (VO_6) by phosphate tetrahedrons (PO_4) results in very poor electron conductivity, even poorer than pure water.

Then the existence of carbon content in the nanocomposite was verified by Raman measurements. As shown in Figure 3.5b, the characteristic signatures at ~ 1358 cm^{-1} and ~ 1591 cm^{-1} are attributed to the D-band (disorder-induced phonon mode) and G-band (E_{2g} vibrations of graphite) of carbon, respectively.[193] In addition, the peak intensity ratio of D and G bands (I_D/I_G) reflects the degree of crystallinity of various carbon materials. In our case, an I_D/I_G value of ~ 1 demonstrates that the carbon content partially belongs to the sp^2 type, thereby implying good electron conductivity.[206] The combining consideration of XRD and Raman results reveals that the HN-LVP@C nanocomposite is composed of LVP nanocrystals and fairly ordered carbon.

Important information concerning about chemical composition and electronic structure, as well as elemental valences, was further extracted by XPS, as shown in Figure 3.5c. The binding energy obtained in the XPS survey was corrected for specimen charging by referencing the C 1s line to 284.60 eV.[207] The V 2p core-level spectrum (inset in Figure 3.5c) confirms that the observed value of binding energies for V $2p_{3/2}$ and V $2p_{1/2}$ is consistent with the literature values for V^{3+} in bulk.[208] Furthermore, a rough atomic ratio of Li:V:P:O of about 3:2:3:12 is acquired on the basis of the quantification of corresponding peaks, while the carbon content in the composite is determined to be ~ 26 wt%. Similar elemental composition was also obtained from ICP-OES measurement.

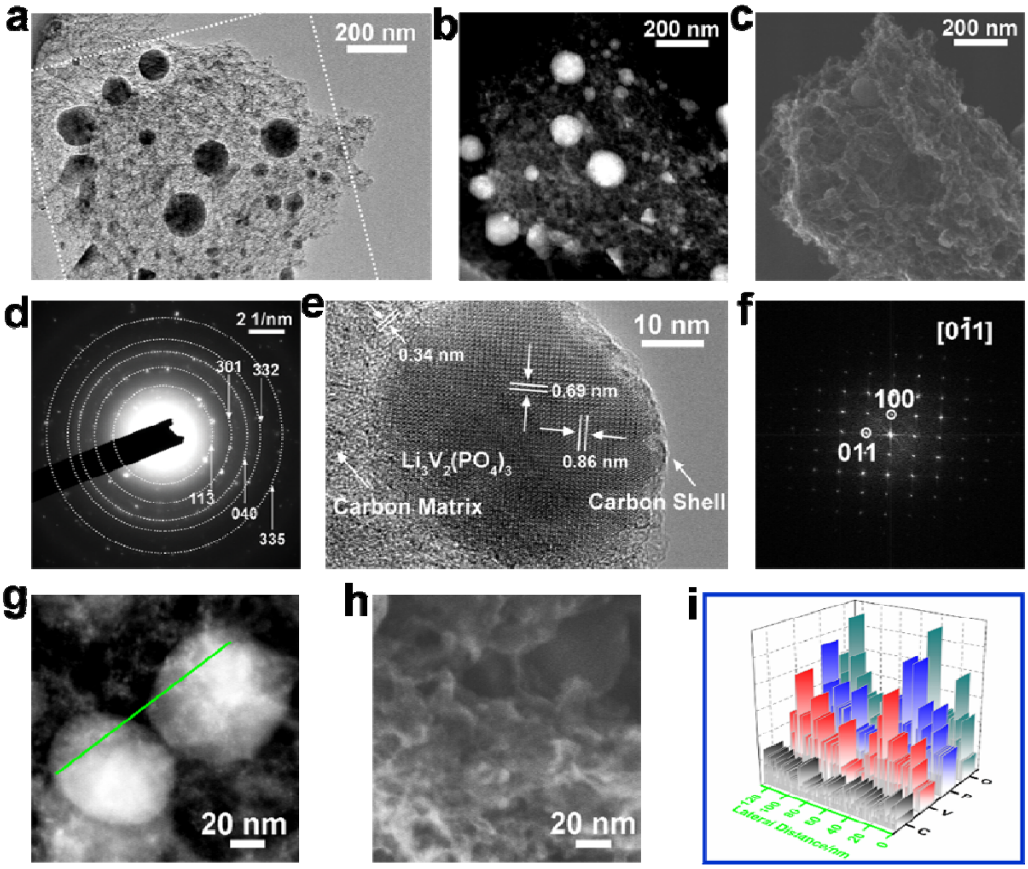

Figure 3.7 (a) TEM micrograph, (b), (c), and (d) are corresponding HAADF image, SEI image and SAED pattern, respectively. ((b) and (c) were both acquired from the white-dashed square in (a)). (e) High-resolution TEM image of a single nanospheres, and (f) the associated FFT pattern. (g) HAADF image from two adjacent nanospheres, (h) the corresponding SEI image, and (i) the cross-sectional EDS line profiles along the green line in (g).

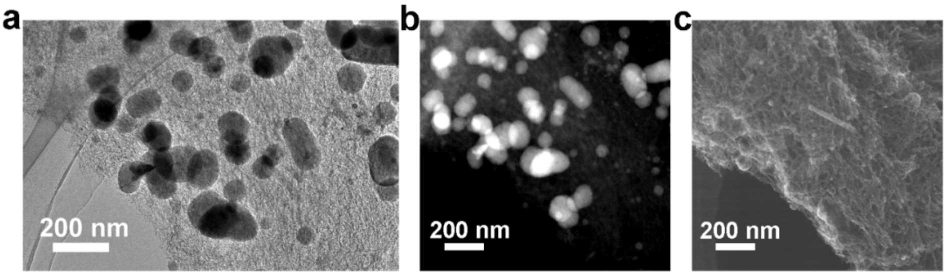

Figure 3.8 (a) TEM image, (b) and (c) are corresponding HAADF and SEI images, respectively. (b) and (c) were captured from the same region as (a).

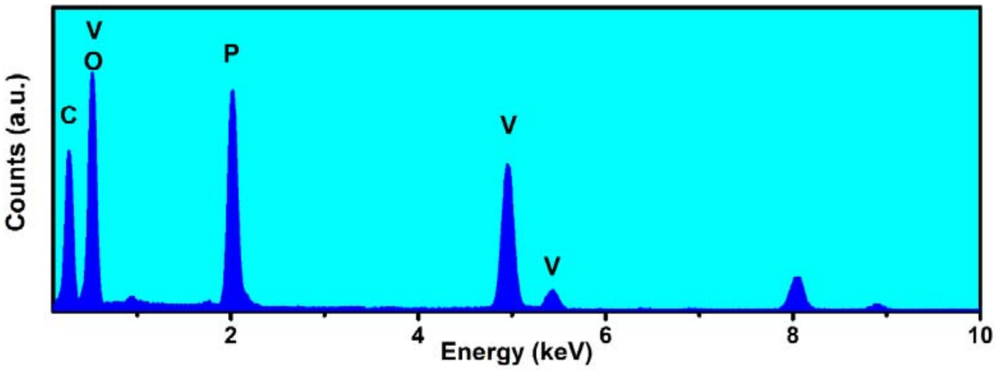

Figure 3.9 The EDS profile acquired from the HN-LVP@C nanocomposite.

The morphological and microstructural feature of the HN-LVP@C nanocomposite was then characterized by TEM and SEM. Firstly, bright-field TEM image, high-angle annular dark field (HAADF, Z-contrast image) image, and secondary electron image (SEI) at STEM mode were sequentially captured from the same area, as shown in Figure 3.7a – 3.7c (also see Figure 3.8). These images clearly evidence that uniform nanospheres (30 ~ 100 nm) are evenly distributed inside a highly porous matrix (pore size: 3 ~ 20 nm). Following, the SAED pattern in Figure 3.7d is well indexed to monoclinic LVP (note: the multi-ring pattern is caused by the collective diffractions from many nanospheres, and the blurry intensity is brought by the diffuse reflection from the carbon matrix.). Upon examining a single nanospheres as in Figure 3.7e, mutual-orthogonal 0.69/0.86 nm lattice fringes corresponding to the (011)/(100) planes (also see Figure 3.7f, the associated FFT pattern) from LVP nanosphere can be indexed, as well as partially ordered 0.34 nm lattice fringe (correspondings to the d-spacing of graphite (002) planes) from the surrounding carbon matrix. Notably, each LVP nanosphere possesses its conformal carbon coating (ca. 1 - 2 nm in thickness) among repeated observations (also see Figure 3.8).

Consequently, EDS spectrum was utilized to check the elemental distribution in the composite. The quantitative EDS spectrum (Figure 3.9) confirmed the existences of C, V, O and P elements in the nanocomposite, and further verified a rough molar ratio of 2 : 3 for vanadium and phosphorus elements, in accordance with the chemical formula as well as the XPS result. No obvious peaks corresponded to other impurity elements can be observed (The element Li cannot be identified by EDS detector). The cross-sectional EDS line profiles (Figure 3.7i) over two adjacent nanospheres (the green line in Figure 3.7g. Figure 3.7h from SEI with the same area as Figure 3.7g also proves that nanospheres are embedded inside the highly porous matrix.**)** suggest a synchronized fluctuation of vanadium, phosphorus, and oxygen contents, remaining the carbon content almost unchanged. In brief, all the TEM analysis confirmed a hierarchical composited structure composed of porous carbon networks with embedding LVP/C core-shell nanospheres.

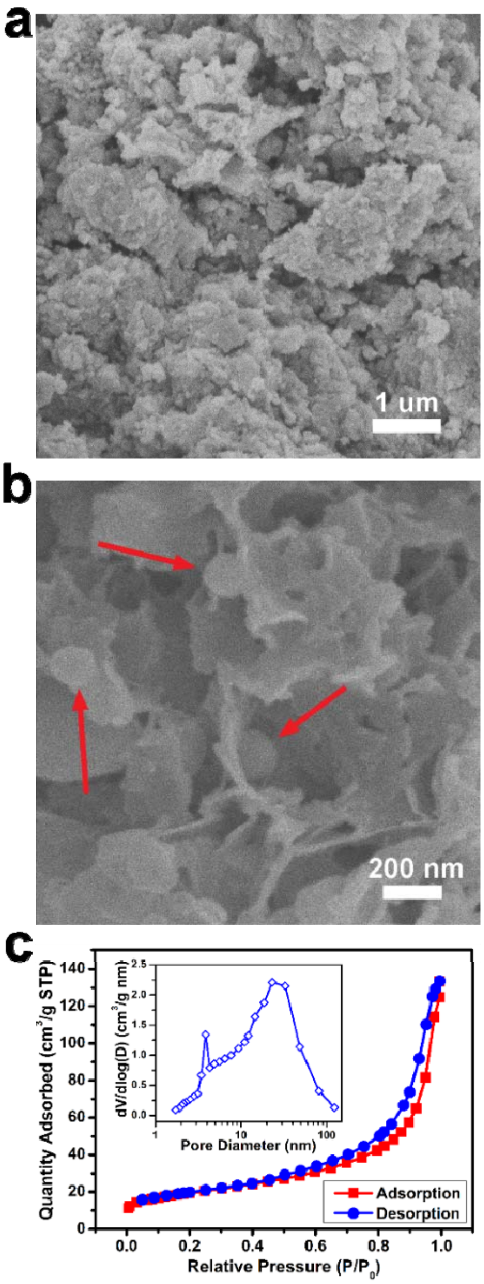

Figure 3.10 Typical (a) low-magnification and (b) high-magnification SEM micrographs of HN-LVP@C nanocomposite. (c) Nitrogen adsorption–desorption isotherms of the HN-LVP@C nanocomposite. Inset: the plot of pore-size distribution calculated by the BJH formula in the desorption branch isotherm.

Combining the TEM results with the SEM micrographs as shown in Figure 3.10a, it is clear that the HN-LVP@C nanocomposite appears to have a sub-micrometer or micrometer size with irregular shape. It can be also depicted that most LVP nanospheres are well embedded inside the carbon "foam", however, there are still a few nanospheres exposed to block some pores (denoted by red arrows in Figure 3.10b). To further investigate the pore structure and the Brunauer-Emmett-Teller (BET) surface area of the HN-LVP@C nanocomposite, nitrogen isothermal adsorption-desorption measurement was performed. The results are presented in Figure 3.10c, showing typical type-IV isotherm of a nanoporous characteristic with a BET surface area of 69 m^2/g. The corresponding Barrett-Joyner-Halenda (BJH) pore-size distribution (Figure 3.9c, inset) suggests a continuous existence of pores ranging from mesopores to macropores, with two peaks centered at 4 and 23 nm, which is in accordance with the TEM result. This innovative meso-macro porosity is expected to facilitate the penetration of electrolyte and to afford ample interfacial contact, thereby vigorously promote the solid state diffusion kinetics of lithium intercalation.

3.4 Electrochemical Performances

The effect of the novel hierarchical carbon coating on the electrochemical performance of LVP was thoroughly evaluated at room temperature with respect to Li^+ insertion/extraction using a coin-type half-cell, and the results are presented in Figure 3.11. Firstly, EIS of the HN-LVP@C electrode was investigated on a freshly assembled cell, again after the 1st to 4th cycle to understand the electrolyte infiltration process during the cell charge/discharge. As shown in the Nyquist plot in Figure 3.11a, a decrease in the total resistance (the resistances from the electrolyte, charge transfer and interfaces) was observed between the fresh cell and the sebsequent curves, which could be ascribed to the increasing conductivity of the cathode after electrolyte infiltration. The diameter of the semicircles remain almost unchange after the 1st cycle, indicating the formation of a stable solid electrolyte interface (SEI) due to the efficient electronic/ionic transport through the hierarchically porous electrodes upon cycling. Next, the CV profile is recorded to gain deeper understanding on the charge/discharge process of the HN-LVP@C electrode between 3.0 and 4.3 V. As can be seen in Figure 3.11b, three pairs of oxidation and reduction peaks could be clearly figured out in the first cycle, which were consistent with previous reports.[175,180] The first Li^+ was extracted via two anodic peaks at 3.62 and 3.70 V, confirming the exitance of ordered $Li_{2.5}V_2(PO_4)_3$ intermediate phase and $Li_2V_2(PO_4)_3$ phase. Then the second Li^+ was removed by one step at 4.11 V to form $LiV_2(PO_4)_3$. Three cathodic peaks located at 3.56, 3.64, and 4.02 V are observed owing to the reinsertion of the two Li^+, resulting from the $V^{4+}/^{V3+}$ redox couple.

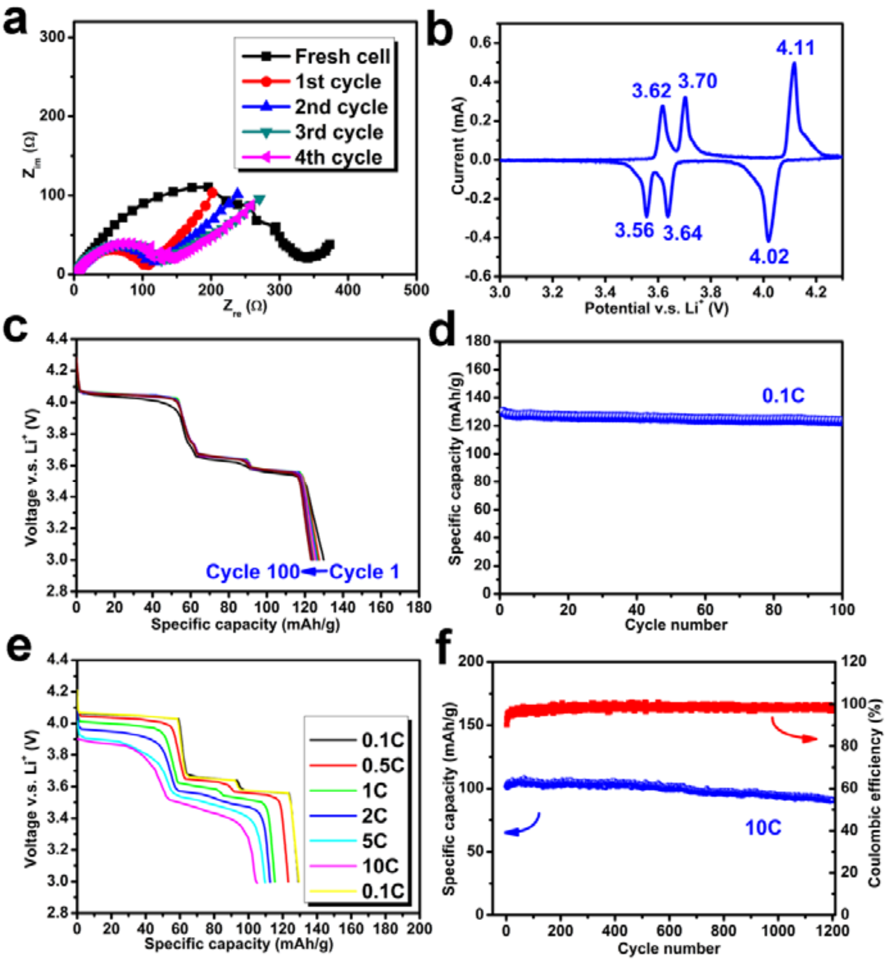

Figure 3.11 Electrochemical performance of HN-LVP@C nanocomposite tested between 3.0 and 4.3 V (versus Li/Li$^+$) at room temperature. (a) EIS spectra in the frequency range between 0.1 Hz and 100 kHz with a vibration of 2 mV. (b) A typical CV profile at a scanning rate of 0.1 mV/s. (c) Discharge voltage profiles for cycles 1, 10, 20, 30, 40, 50, 60 70, 80, 90, and 100 at 0.1C. (d) Cycling performance at a rate of 0.1C. (e) Rate capabilities with increasing rates from 0.1C, 0.5C, 1C, 2C, 5C and 10C at first cycle, then back to 0.1C. (f) Discharge capacity and Coulombic efficiency versus cycle number at a rate of 10C.

Subsequently, the representative discharge voltage profiles of the HN-LVP@C cathode at a current rate of 0.1C (1C = 133 mA g^{-1}) in the voltage window of 3.0 - 4.3 V were recorded and presented in Figure 3.11c. Three clear plateaus at 4.04 V, 3.64 V, and 3.57 V were observed in each profile and are in good agreement with the CV test. The battery delivered an initial discharge capacity of ca. 130 mAh g^{-1}, approaching its theoretical value (133 mAh g^{-1}). The corresponding cycling performance at 0.1C was shown in Figure 3.11d, which demonstrated an excellent cycling stability with a retention capacity of ca. 124 mAh g^{-1} at the 100th cycle.

Table 3.1 Comparison of electrochemical properties among LVP-based cathode materials in previous reports and current work.

	Current Rate	Cycle Number	Capacity Retention
Kim et al.[102] LVP/PEDOT	10C	100	92%
Zhang et al.[203] LVP/C/SiO_2	2C	100	77.5%
Chen et al.[200] LVP/C	20C	300	85.6%
Du et al.[178] LVP/C	5C	50	75%
Current Work	**10C**	**1, 200**	**90%**

Nowadays, superior rate capability is highly desirable for cathode materials in high power LIBs applications, such as electric vehicles and hybrid electric vehicles. Therefore the cycling responses of the nanocomposite cathode at high C rates were evaluated and shown in Figure 3.11e. The HN-LVP@C cathode delivers a discharge capacity of 129.2 (0.1C), 123.2 (0.5C), 115.4 (1C), 112.6 (2C), 109.8 (5C), 105.4 (10C), and then back to 129.4 mAh g^{-1} (0.1C), respectively, revealing an excellent and reversible rate performance. Surprisingly, the HN-LVP@C cathode possesses outstanding cycling stability at high current rate with negligible capacity fading.

After tolerating 1200 cycles at a rate of 10C (Figure 3.11f), the cathode has a capacity retention of above 90%. It is worth noting that the Coulombic efficiency was constantly high (> 99%) during the overall battery operation, indicating a good reversibility at such a high current rate. In comparison with other conductive-coated LVP cathode materials reported in previous works (Table 3.1), our HN-LVP@C nanocomposite is significantly superior, especially upon high-power usages.

3.5 Summary

In summary, we have demonstrated in this chapter that the electrochemical performance of LVP can be notably improved by simultaneous size controlling and conductive coating. The rational design and facile realizing of such a novel HN-LVP@C nanocomposite led to an exceptionally cycle stability and excellent high power capability, which can be directly ascribed to its unique microstructural merits. The remarkable performance derived from our simple and scalable synthesis proposes this 4 V-class material one of most promising candidates for future batteries.

CHAPTER 4 GRAPHENE NANOCLUSTERS DECORATED NIOBIUM OXIDE NANOFIBERS AS VISIBLE LIGHT PHOTOCATALYST

In pursuit of solving various energy and environmental problems, high-performance photocatalytic materials are extensively studied, in which carbon-based nanocomposite plays an important role. In this chapter, we report a novel nanocomposite of porous Nb_2O_5 nanofibers decorated with graphene nanoclusters on their surfaces. By utilizing such a composite, the active region of Nb_2O_5 has been significantly extended from UV region to UV-Vis region; and hence, the photocatalytic performance has also been greatly improved as demonstrated by comparing with pure Nb_2O_5 and Nb_2O_5/Carbon nanostructures. Detailed structure analysis revealed that the performance enhancement originated from the ample existence of chemical bondings and the unique orientation of graphene layers, which are quite different from classical "core-shell" composites.

4.1 Introduction

Worldwide efforts have been made to develop high-performance photocatalytic materials for energy and environmental applications, and titania (TiO_2) is probably the most widely investigated photocatalyst so far. Due to its wide bandgap, TiO_2 is active in the ultraviolet (UV) light range but relatively inert to visible light.[158,209–211] In order to fully utilize solar energy for photocatalysis, researchers attempted to enhance the visible light photocatalytic activity of TiO_2 through doping, dye sensitization, bandgap engineering and etc.[145,212–217] Among these methods, the use of sensitization could effectively extend the absorption spectrum of TiO_2 at a relatively low cost and is therefore considered to be a promising approach for its large-scale applications.[145,216,217] Functional carbonaceous materials have been utilized to improve the photocatalytic activity for various materials.[218–221] Recently, graphene are found to exhibit high level of absorption in visible-light region and could enhance charge separation along the interfaces between photocatalysts and organic pollutants.[136,222–225]

Despite the success mentioned above, there is also a growing interest in developing material systems other than TiO_2 for photocatalytic applications. For example, with a bandgap (E_g) of 3.4 eV, niobium oxide (Nb_2O_5) is a major semiconductor with great potential for water treatments.[149,226–229] One of the main advantages of Nb_2O_5 is that it shows long-term stability in photocatalytic process.[149] Analogue to TiO_2, Nb_2O_5 displays poor photocatalytic activity to visible light due to its large bandgap.[148,151,159] This issue could be partially solved by carbon modification in Nb_2O_5 nanoplates through a solvothermal method.[148] Nevertheless, there is still much room for enhancing the performance of Nb_2O_5 for photocatalytic applications.

In light of the situation discussed above, we propose to develop a new system-Nb_2O_5 nanofibers (Nb_2O_5 NFs) decorated with graphene nanoclusters. We chose to work on Nb_2O_5 nanofibers rather than nanoparticles mainly because of their better handleability.[230,231] Electrospinning was employed as a feasible and scalable technique in terms of synthesizing sub-micrometer-sized fibers by utilizing an electrical charge to draw fibers from a liquid with suitable viscosity.[232,233] Graphene, the two-dimensional macromolecular sheet of carbon, exhibits superior electrical conductivity, mechanical properties and large theoretical specific surface areas.[234,235] The introduction of graphene for decorating the surface of Nb_2O_5 nanofibers should improve the nanofibers' photocatalytic activity through (1) visible light absorption originated from the graphene; (2) enhancement of the charge separation because of the formed conjugated structure.

Herein, in this chapter, we demonstrate a successful attempt for the fabrication of graphene nanoclusters decorated Nb_2O_5 nanofibers via simple electrospinning technique plus hydrothermal method. As to be illustrated, the material exhibits significantly extended absorption spectrum and hence greatly enhanced photocatalytic activity. A possible mechanism for explaining the visible light activity is also proposed based on the detailed structure analysis of the composite nanofibers.

4.2 Experimental Section

4.2.1 Synthesis of Samples

The samples were prepared via an electrospinning process plus a hydrothermal treatment. The precursor solution for electrospinning was prepared by adding 9 wt% polivinilpirrolidone (PVP) into a 0.1 mol/L niobium ethoxide solution followed by stirring for several hours at room temperature.[236] The electrospinning parameters were: distance between the needle and the collector (Al foil) = 14 cm, applied voltage = 16 kV, precursor feeding rate = 1 mL/h. After electrospinning, the as-spun fibers were first dried in oven at 100 °C for several hours and then calcined in a muffle furnace at 500 °C for 1 hour in air. Samples thus prepared are Nb_2O_5 nanofibers, hereafter called Nb_2O_5 NFs. 0.1g Nb_2O_5 NFs together with glucose were then put into a 40 mL Teflon-lined stainless steel autoclave containing 32 mL of deionized water to produce a 0.5 g/L glucose solution. The mixture was stirred to form a milk-like suspension, sealed and hydrothermally treated at 180 °C for 4 h. After cooling, filtration, washing (using deionized water) and drying in oven at 80 °C for 2 h, grey samples were obtained. They are actually Nb_2O_5 NFs coated with carbon. A series of samples with glucose concentrations varying from 0 to 30 g/L were prepared. In this paper, we only discuss two samples prepared with a relatively low glucose concentration (0.5 g/L) and a higher glucose concentration (30 g/L).

4.2.2 Characterizations

XRD measurements were made using a X-ray diffractometer (XRD, D/Max-RB, Rigaku, Japan) with Cu Kα line of 0.1541 nm. The morphologies of the as-prepared samples were observed by means of SEM (SU8020, Hitachi, Japan) and TEM (JEM-2100F, JEOL, Japan). Ultraviolet–visible (UV–Vis) diffuse reflective spectra were measured with a UV–vis spectrometer (TU-1950, Beijing Purkinje General Instrument Co., Ltd, China). The photoluminescence (PL) spectra of the samples were detected with a Jobin Yvon HR 800 micro-Raman spectrometer using the 325 nm line from a He-Cd laser. XPS spectrum was accomplished using an X-ray photoelectron spectrometer (ESCALAB 250, Thermo, America).

4.2.3 Photocatalytic Measurement

The visible light photocatalytic activity of the samples was evaluated by degradation of Methyl Orange (MO) (at natural pH value) under irradiation of a 400 W metal-halide lamp equipped with a cut-off glass filter transmitting $\lambda > 380$ nm. The quartz reaction vessel was cooled by the circling water. For the degradation of MO, the initial concentration of MO was 20 mg/L with a photocatalyst loading of 1 g/L. Firstly, the solution was stirred in dark to reach an adsorption-desorption equilibrium between the organic molecules and the catalyst. Upon irradiation for a certain time interval, a small amount of the solution was taken and centrifuged; the concentration of MO was determined by measuring its absorbance at 464 nm.

4.3 Structural Characterizations

Microstructures of all samples were carefully examined through XRD, SEM and TEM. Figure 4.1a shows the typical SEM image of the hydrothermally treated Nb_2O_5 nanofibers, which are ~ 200 nm in diameter and several to tens of micrometers in length. As shown in Figure 4.1b, the XRD measurement indicates that all samples are well crystallized with a hexagonal structure, matching well with the database (JCPDS No. 28-0317). The XRD pattern of the sample after hydrothermal treatment is basically the same as that before the treatment. No diffraction peak was identified to belong to carbon (which should be located at $2\theta = 25.6°$) due to its low percentage.[237]

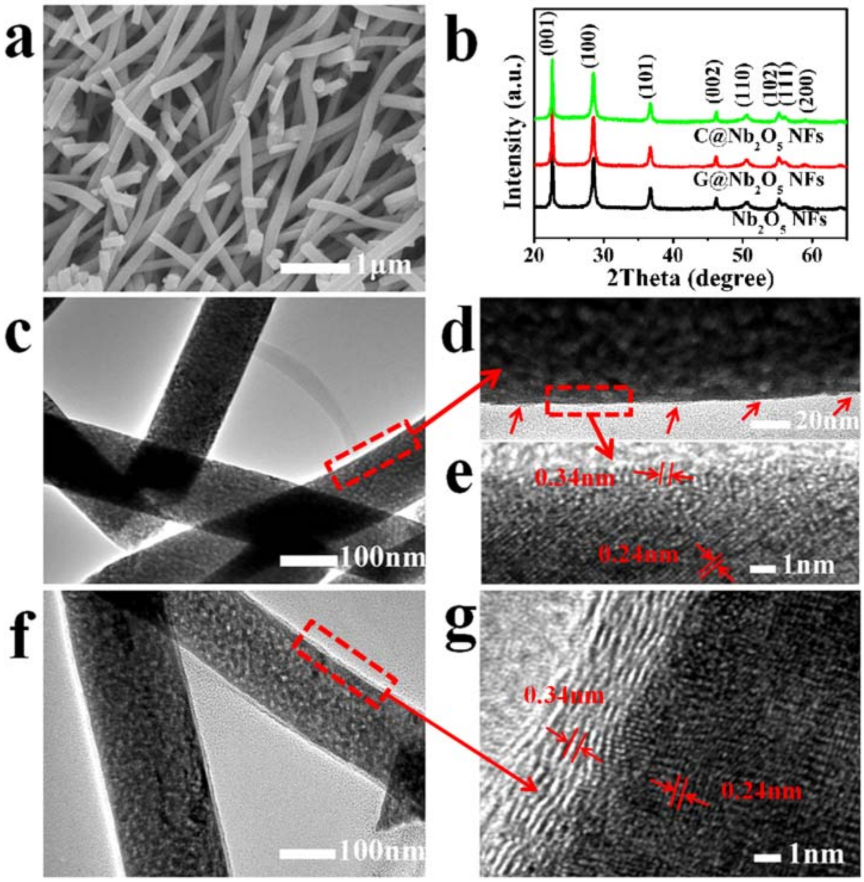

Figure 4.1 (a) SEM image of sample G@Nb$_2$O$_5$ NFs. (b) XRD patterns of Nb$_2$O$_5$ NFs, G@Nb$_2$O$_5$ NFs and C@Nb$_2$O$_5$ NFs.(c) (d) (e)TEM image of G@Nb$_2$O$_5$ NFs, Enlarged TEM image and HRTEM image for G@Nb$_2$O$_5$ NFs. (f), (g) TEM and HRTEM images for C@Nb$_2$O$_5$ NFs.

The HRTEM analysis then revealed that the morphology and structure of carbon coating on Nb$_2$O$_5$ NFs are highly dependent on the concentration of glucose in the hydrothermal step. The sample prepared with a low glucose concentration (0.5 g/L) was found to have discontinuous graphene nanoclusters formed on the surface of Nb$_2$O$_5$ NFs, as shown in Figures 4.1c to 4.1e. The fringes of the nanocluster implied that carbon was partially crystallized with a d-spacing of ~ 0.34 nm, which matched well with typical data for the interlayer distance in graphite.[216] The Nb_2O_5 NFs were well crystallized and composed of uniform nanograins. The corresponding lattice fringe was 0.24 nm, agreeing well with the lattice spacing of the $(1\bar{1}01)$ planes of hexagonal Nb_2O_5. On the basis of the structural features discussed above, this sample is hereafter called G@Nb_2O_5 NFs, meaning graphene nanoclusters decorated Nb_2O_5 NFs.

For samples prepared with higher glucose concentration (30 g/L), continuous and uniform graphite layers with a total thickness of ~ 4 nm are found on the surface of Nb_2O_5 NFs, forming a typical core-shell structure, as shown in Figure 4.1f and 4.1g. This sample is called C@Nb_2O_5 NFs, meaning carbon layer coated Nb_2O_5 nanofibers. It should be noted that the orientation of the graphene layers varied with carbon percentage. For G@Nb_2O_5 NFs, the carbon existed in the form of graphene nanoclusters with graphene layers laying almost vertical to the axial direction of Nb_2O_5 nanofibers. In contrast, for the C@Nb_2O_5 NFs, carbon existed in the form of continuous coating layers, which was parallel to its axial direction of the Nb_2O_5 nanofibers.

Figure 4.2 shows the HR-TEM images for the samples prepared at intermediate glucose concentrations. By increasing the glucose concentration from 0.5 g/L to 10 g/L, the carbon changed from graphene clusters to discontinuous carbon layers, which were consisted of randomly oriented small “carbon sheet”. The evolution could be clearly seen from Figure 4.2a to Figure 4.2c. However, the small "carbon sheets" were turned to oriented parallel to the surface of the nanofibers and typical core-shell structured composite fibers with continuously coated carbon layers could be seen as displayed in Figure 4.2d (20 g/L). And the thickness of carbon layers on the surface of the nanofibers was thinner than that of the C-Nb_2O_5 NFs (30 g/L). Based on the above images, we could conclude that the morphology of the carbon layers exhibited a close dependence on the carbon content.

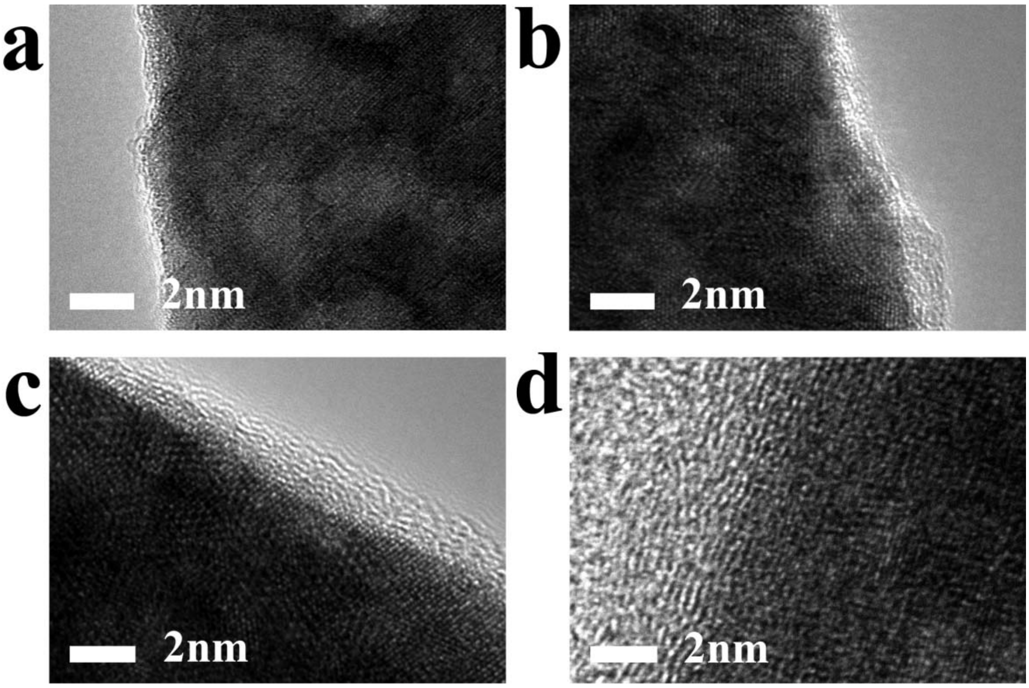

Figure 4.2 HR-TEM of samples prepared at (a) 1 g/L, (b) 5 g/L, (c) 10 g/L and (d) 20 g/L.The composite nanofibers were prepared at different intermediate glucose concentrations of 1 g/L, 5 g/L, 10 g/L and 20 g/L. Firstly, the Nb_2O_5 nanofibers were synthesized. Then, the composite nanofibers were fabricated by the hydrothermal

method by adding glucose solution of 1 g/L, 5 g/L, 10 g/L and 20 g/L. The composite nanofibers were first uniformly dispersed in ethanol, and then several drops of the solution were dipped on a copper mesh to carry out the TEM characterization.

4.4 Photocatalytic Activity

To further understand the roles played by the graphene nanocluster in the composited fibres, optical absorption properties of the samples were examined on a UV-Vis spectrometer. As shown in Figure 4.3a, the bare Nb_2O_5 nanofibers exhibit poor absorption of visible light and the absorption edge is ~ 380 nm, corresponding to a bandgap of 3.4 eV (inset of Figure 4.3a). The G@Nb_2O_5 NFs and C@Nb_2O_5 NFs, however, exhibited much higher visible light absorption up to a wavelength of 800 nm, suggesting much narrowed bandgaps. And the bandgap values were determined to be 3.1 eV and 2.9 eV, respectively. The absorption enhancement could be caused by the fact that carbon could absorb visible light and that the improved synergistic effect may have been a result of the joint electronic system at the interface formed between Nb_2O_5 and carbon.[145,238] Moreover, it has also been reported that graphene nano-ribbons could form a bandgap.[239,240] Herein, the clusters were in such a small size that a bandgap might be formed and it would be partially responsible for the visible light absorption in G@Nb_2O_5. The visible light photocatalytic activities of all samples were examined through measuring the degradation rate of MO (represented by the ratio C/C_0, where C and C_0 stand for the remnant and initial concentration of

MO) in the presence of the nanofibers under visible light irradiation with wavelength λ > 380 nm. To make the results reliable, control experiments were firstly conducted under different conditions: (1) in the presence of the photocatalyst but without the light irradiation and (2) with visible light irradiation but in the absence of photocatalyst. As shown in Figure 4.3b, the experiments reveal that there is no appreciable decrease of the MO concentration over the samples after the first 30 min, indicating an absorption-desorption equilibrium of MO. Besides, a small reduction of the MO concentration about 5% could be observed after the visible light irradiation for 5 h, confirming the negligible photodegradation in the system. Following, the result for the photocatalytic experiments is shown in Figure 4.3c. Bare Nb_2O_5 NFs displayed poor visible-light photocatalytic activity (degradation efficiency of ~ 20% for 5 h) due to the relatively large band gap.[236] Samples with carbon decoration showed a much higher visible-light photocatalytic activity: degradation efficiencies of ~ 95% for G@Nb_2O_5 NFs and ~ 65% for C@Nb_2O_5 NFs. It is interesting to note that G@Nb_2O_5 NFs showed the highest efficiency despite of its low carbon concentration.

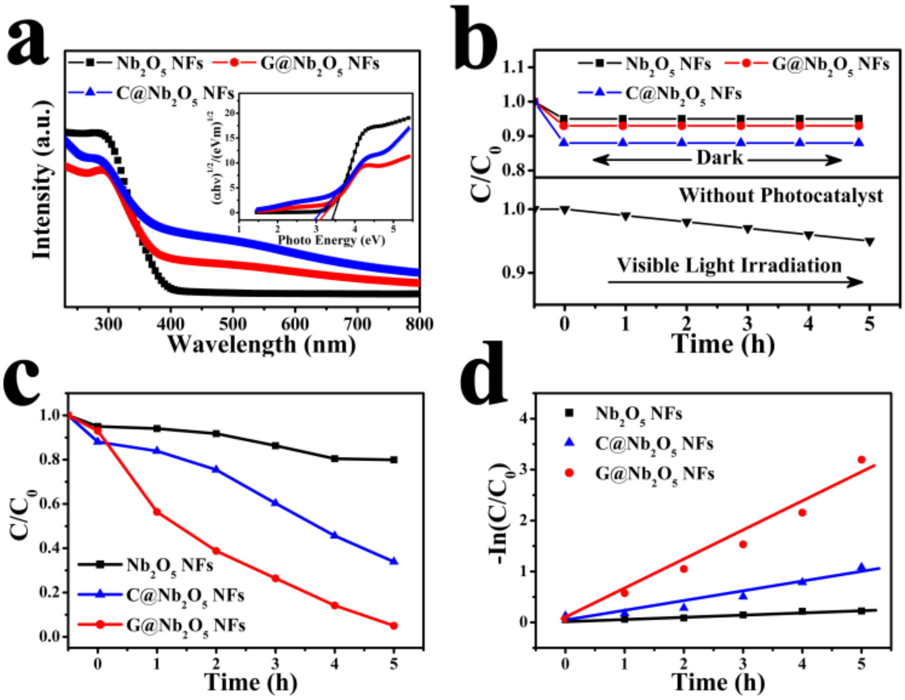

Figure 4.3 (a) UV-Vis absorption spectra of the three samples. (b) Degradation profiles of MO in the presence of the G@Nb_2O_5 NFs and C@Nb_2O_5 NFs but in the dark, and with visible light irradiation but in the absence of the nanofiber photocatalysts. (c) Photocatalytic degradation profiles of MO over the three samples. (d) Kinetic linear simulations of MO photocatalytic degradation among different samples.

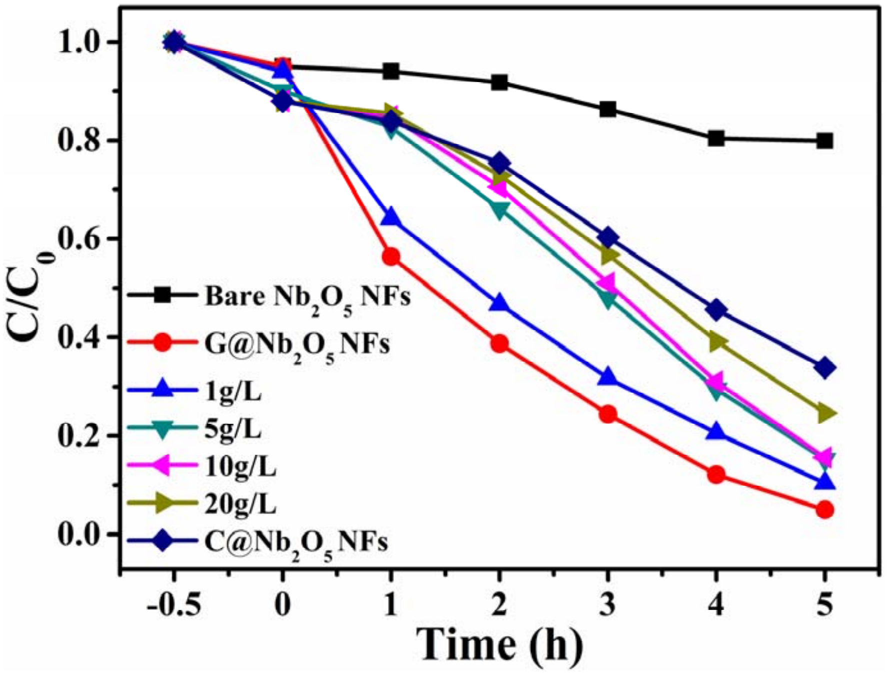

Figure 4.4 Photocatalytic degradation efficiency for G@Nb_2O_5 NFs, C@Nb_2O_5 NFs and samples prepared at intermediate concentrations ranging from 1 g/L to 20 g/L.

The photocatalytic degradation experiments were carried out for the samples of 1 g/L, 5 g/L, 10 g/L and 20 g/L following the process described above. Figure 4.4 shows the photocatalytic degradation efficiency for G@Nb_2O_5 NFs, C@Nb_2O_5 NFs and samples prepared at intermediate concentrations ranging from 1 g/L to 20 g/L. It could be clearly seen that the photo-degradation efficiency of the four samples (1 g/L to 20 g/L) decreased with the increase of the glucose concentration. And they were in the range between G@Nb_2O_5 NFs and C@Nb_2O_5 NFs. After irradiation for 5 h, samples prepared at 1 g/L, 5 g/L, 10 g/L and 20 g/L exhibited degradation efficiency of 90%, 85%, 85% and 75%, respectively. The decrease of the efficiency indicated a carbon-content dependent relationship for our composite nanofibers. With slight increase of the carbon layer's thickness, the degradation efficiency obviously decreased. Figure 4.3d shows -ln (C/C_0) v.s. reaction time profiles for the three samples. According to the results, the photocatalytic reaction constant k was 0.5470 h^{-1} for G@Nb_2O_5 NFs, which was almost three times more than that of C@Nb_2O_5 NFs ($k = 0.1950\ h^{-1}$). The high efficiency of G@Nb_2O_5 NFs was closely related with the feature of graphene nanoclusters when compared to C@Nb_2O_5 NFs with typical core-shell structures.

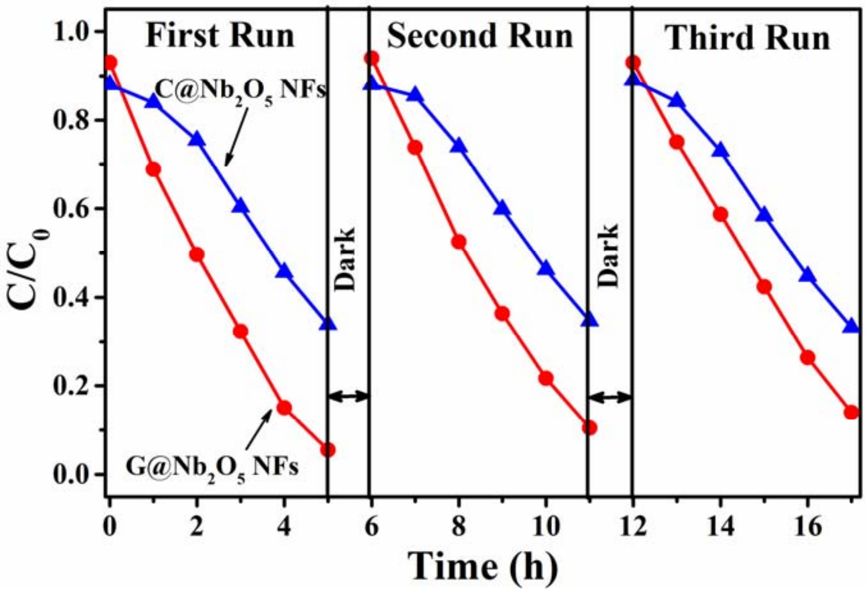

Figure 4.5 Photocatalytic degradation efficiency for G@Nb_2O_5 NFs and C@Nb_2O_5 NFs in the cycling experiment.

Cyclic photocatalytic experiments were repeated three times for sample G@Nb_2O_5 NFs and C@Nb_2O_5 NFs. After every photocatalytic reaction, the samples were obtained by centrifuging the solution. The collected samples were used in the next photocatalytic degradation experiment. From the results shown in Figure 4.5, it could be seen that the efficiency of C@Nb_2O_5 NFs exhibited almost no changes and the G@Nb_2O_5 NFs showed a slightly decreased efficiency in the second and third cycling run. However, the obtained efficiency of G@Nb_2O_5 NFs was still much higher than that of C@Nb_2O_5 NFs. And the stability of the C@Nb_2O_5 NFs could be mainly attributed to the uniformly coated thick carbon layers. The efficiency decrease for the G@Nb_2O_5 NFs might be related with the loss of the graphene nanoclusters during the centrifuging process.

Table 4.1 Comparison on degradation efficiency of popular photocatalysts modified by graphene or reduced graphene oxide

Composite	**Light Region**	**Degradation Efficiency**	**Morphology**
G@Nb_2O_5	Visible Light	95%/300min	Nanofibers
RGO-CdS[241]	Visible Light	90%/120min	Nanorods
CdS-GR[242]	Visible Light	80%/300min (Best efficiency in pmethoxybenzyl alcohol)	Nanoparticles
G-ZnO[243]	UV Light	80%/240min	Nanofibers
ZnO/graphene[244]	UV Light	95%/40min	Nanoparticles

RGO-ZnO[245]	Visible Light	100%/120min	Nanoparticles
GO-TiO_2[246]	Visible Light	25%/180min	Nanocrystals
Graphene@TiO_2[247]	Visible Light	70%/200min	Nanoparticles
TiO_2/C[238]	Visible light	84%/360min	Core-Shell Nanofibers
G-TiO_2[248]	UV Light	75%/180min	Nanoparitcles
G-TiO_2[249]	UV Light	91%/90min	Mesoporous Nanospheres
C-$Bi_{12}TiO_{20}$[250]	Visible Light	120min	Nanorods
SnO_2-Graphene[251]	Visible Light	100%/40min	Aerosol
Zn_2TiO_4@C[252]	UV Light	100%/40min	Core-Shell Nanofibers

The favourable photocatalytic activity of our sample was comparable with previous reports for similar systems like TiO_2, ZnO and CdS (in Table 4.1), showing great potential as a promising visible light photocatalyst.[224,242,243,247] Due to the limit of the relatively large diameter of the composite nanofibers, the efficiency was lower than some systems with much smaller dimensions, such as RGO-CdS nanorods, RGO-ZnO nanoparticles, C-$Bi_{12}TiO_{20}$ nanorods and G-SnO_2 aerosol.[224,241,245,250,251] We believed that the efficiency could be further enhanced by reducing the diameter of our nanofibers.

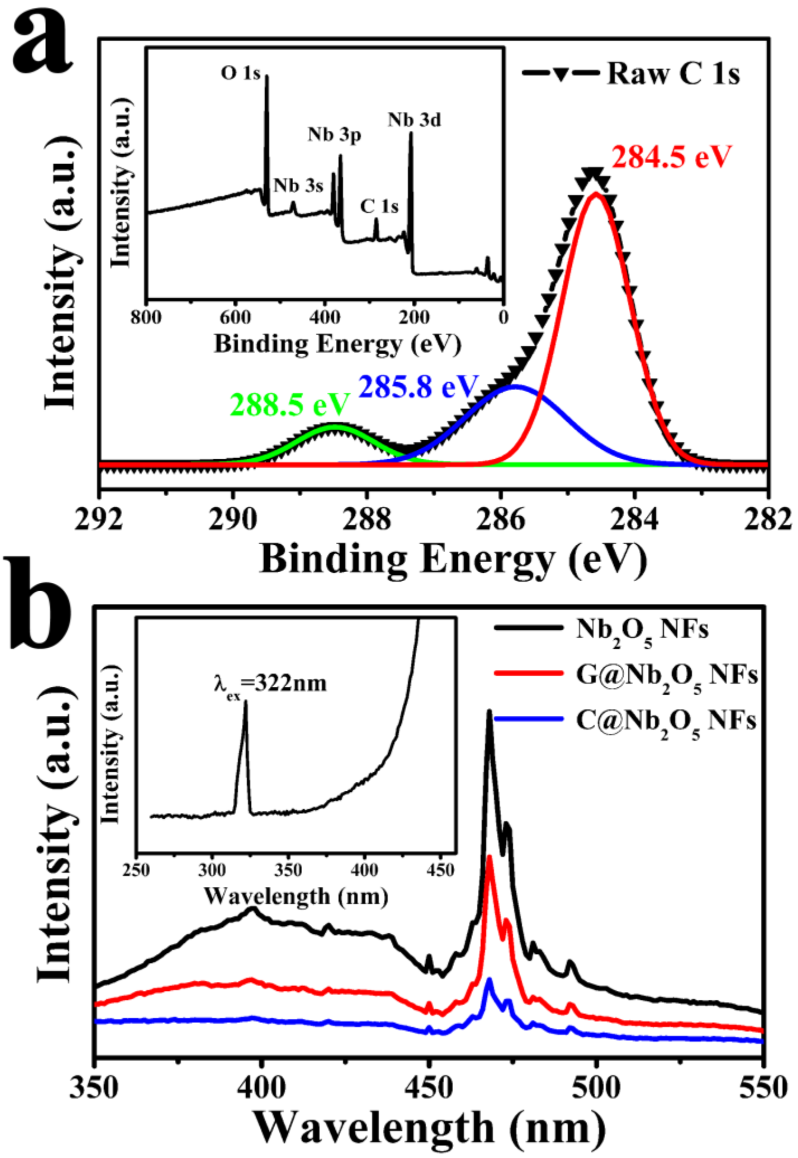

Figure 4.6 (a) XPS spectra of C 1s for G@Nb$_2$O$_5$ NFs, and the inset figure is the fully scanned spectra. (b) PL spectra for the three samples.

To better understand the aforementioned synergistic effect for the enhanced visible light photocatalytic activity, XPS analysis was also conducted to reveal the nature of contact between Nb$_2$O$_5$ and carbon. Figure 4.6a presents the XPS survey spectra of

G@Nb_2O_5 NFs (inset figure) and the enlarged high resolution XPS spectra of the C 1s region around 285 eV. As indicated in the inset spectra, all peaks could be identified to belong to Nb, O and C, suggesting the coexistences of these elements in the samples. For the C 1s region, the binding energy with a peak at 284.5 eV was attributed to the accumulation of graphite carbon.[225,253] In addition to the strong peak at 284.5 eV, two weak peaks were also observed at 285.8 eV and 288.5 eV, representing the characteristic signatures of the carbonate with oxygen bound species C-O and C=O, respectively.[216] Consequently, the XPS results suggested the formation of carbon-modified Nb_2O_5 nanofibers and the coated carbon species functionalized as a surface sensitizer to absorb visible light.[148] The C 1s result for C-Nb_2O_5 sample exhibited almost no changes, which is not shown here.

To clarify the deep reason for the enhanced activity, the contact issue should also be considered which had always been a key factor in the overall performance of a composite. In a carbon-metallic oxide system, the physiochemical nature of the contact could vary upon different sample preparing methods. For example, in TiO_2-carbon system, there are generally two kinds of carbon in the composite system. The first kind is doping, which means certain atoms in TiO_2 lattice are substituted by carbon atoms, thus a new energy band structure is achieved. The second one is surface modification (carbon coating), forming an electronic interaction which was responsible for the sensitization effect.[145,216] In our case, the Nb_2O_5 nanofibers were modified by the surface coated carbon. This structure not only ensures good connection but also helps to separate the photo-generated electrons and holes effectively. Figure 4.6b presents the PL spectroscopy of the three samples. As shown in the inset figure, an excitation light with wavelength at 325 nm was chosen and the bare Nb_2O_5 NFs exhibited the highest luminescence intensity, indicating more recombination of the photo-generated electron-hole pairs. By contrast, the recombination of the charge carriers was greatly inhibited in the carbon decorated samples which could be detected from the much lower emission intensity. Besides that, the PL emission intensity decreased with the increase of the thickness of the graphene layers. Therefore, it was reasonable to conclude that effective separation of the photo-generated electrons and holes pairs could be achieved by the deposition of graphene layers in vertical and parallel directions.

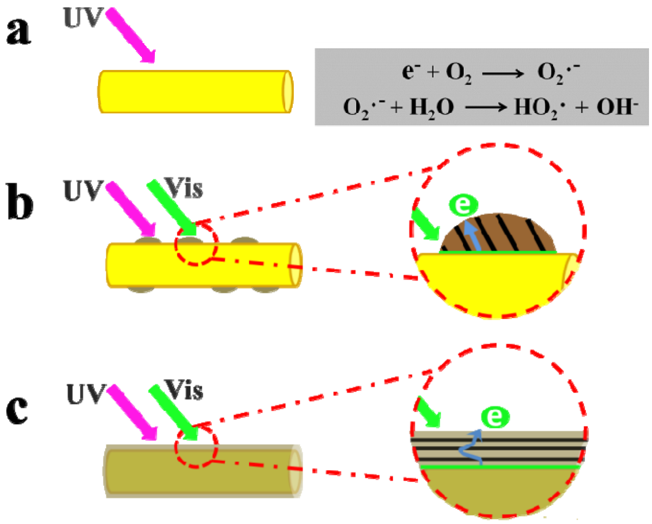

Figure 4.7 Proposed mechanisms for the visible light-induced photo-degradation of MO by the composite nanofibers.

With the structural information extracted above, mechanisms for the visible photocatalytic behaviour of our samples and the difference of activity between the G@Nb_2O_5 and C@Nb_2O_5 NFs were proposed. As shown in Figure 4.7, Nb_2O_5 NFs can only show UV-light photocatalytic activity via chemical reactions that would lead to the formation of chemically active radicals (e.g. $HO_2\cdot$), a mechanism already well documented. However, after coating Nb_2O_5 with carbon of different morphologies, G@Nb_2O_5 NFs and C@Nb_2O_5 NFs could absorb both UV and visible light, leading to the excitation of carbon and electrons being transferred to the conduction band of the Nb_2O_5, resulting in photocatalytic activity in the visible light region.[145,216,224,225] For our samples, the alignments of carbon layers were closely related to the carbon content. The possible mechanism for the carbon-content dependent photocatalytic performance (shown in Figure 4.4) of the composite can be proposed. On one hand, higher carbon content would lead to better absorption of visible light and hence, higher photocatalytic activity. On the other hand, however, the continuous carbon layer would reduce the exposure of Nb_2O_5 NFs to the light and would result in more barriers for the transfer of optical charges. Such repetition between two controversial effects has also been observed in other composite systems.[215] Apart from this factor, the alignment of the graphite layers was also an important reason why G@Nb_2O_5 NFs exhibited better photocatalytic activity than C@Nb_2O_5 NFs, which was clearly displayed in Figure 4.7b and 4.7c. It is well known that graphite layers are highly anisotropic materials - the charge mobility along the directions of graphene layers is much larger than that along its normal direction. In G@Nb_2O_5 NFs, graphene nanoclusters grew in such a way that the carbon sheets were nearly vertical aligned to the Nb_2O_5 NFs, while in C@Nb_2O_5 NFs, the carbon sheets were parallel to the Nb_2O_5 NFs. The electrons have to pass through the carbon sheet instead of passing along the sheet to react with the organic pollutant. Moreover, due to the high specific surface area of graphite layers, the MO molecules could be adsorbed on the surface. Thus, the vertical-aligned graphene layers on the nanofibers could not only make full use of the excellent in-plane conductivity of graphene, but also promote the effective contacts between MO molecular and Nb_2O_5/graphene content, leading to the acceleration of the photocatalytic reaction. The carbon-content dependent photocatalytic performance for composite samples prepared at various glucose concentrations (shown in Figure 4.4) could be well explained by the proposed mechanism.

4.5 Summary

In summary, niobium oxide nanofibers decorated with graphene nanoclusters were successfully synthesized via an electrospinning process followed by a hydrothermal treatment. The composite nanofibers displayed a fairly high photocatalytic activity in visible-light region, which had never been found in pure niobate nanostructures. Through analysis, it was found that G@Nb_2O_5 NFs exhibited favourable features in visible light absorption, charge separation and charge transfer during the photocatalytic process. The discontinuous coverage and nearly vertical alignment of graphite layers in G@Nb_2O_5 NFs were important structure factors leading to a high visible-light photocatalytic activity. Therefore, the graphene nanoclusters decorated

Nb_2O_5 nanostructures could be a potential candidate for applications of eliminating organic pollutants in waste water.

CHAPTER 5 DIRECT OBSERVATION OF CARBON NANOSTRUCTURE GROWTH ON HOST PARTICLES INSIDE TEM

In view of our studies on synthesis and applications of carbon-based nanocomposite, the carbon growth mechanism in nanocomposites is worthy of a further study. Therefore, we demonstrate in this chapter the direct observation on transition of amorphous carbon into graphene nanostructures at liquid-solid interfaces by using HRTEM. We found that the amorphous carbon first nucleate into nanoclusters at step-edges on Pt_3Co surface and then merge into graphene layers through a kinetic restructuring *via* oriented-attachment. This observation leads to a clear picture of the formation mechanism of few-layer graphene along the liquid-solid interface in the Pt_3Co-carbon system; and, to our best knowledge, this is for the first time that a dynamic and atom-precision monitoring of such interface could be achieved.

5.1 Introduction

Disclosing the mechanism of chemical reaction at atomic level is of great importance for the structural and outlook design of functional inorganic materials. The advancing in situ transmission electron microscope (TEM) technique now offers an exclusive approach towards direct observation of real-time process with atomic resolution.[160,254] Diversified in situ TEM techniques have enabled direct observations of solid phase reactions,[255,256,166,257] and have also made great contributions to solid-gas reactions (by using in situ cells as specimens).[258,161] These studies have provided accurate information on crystal growth and catalytic reaction via solid/solid and solid/gas interactions, and therefore offered valuable guidance in synthesizing novel nanomaterials and designing of new-fashioned catalysts. However, applying such in-situ TEM technique into liquid-solid reactions has been long hampered by difficulties in introducing liquids into high-vacuum TEM systems.[259] One possible solution to overcome this constraint would be to employ sealed liquid cells as TEM specimens (made up of Si_3N_4 or SiO_2)[260–262] yet not only this would involve a complex specimen packaging process to obtain a good cell, the electron transmittance of the resulted cells would also be poor due to the inevitably thick cell walls, thus, affecting the applicability of this method.

An example that may benefit from atomic resolution imaging of liquid-solid reactions could be carbon nanostructures. The most prevalent growth models for carbon materials are vapor-liquid-solid (VLS) mechanism and solid-liquid-solid (SLS) mechanism where the liquid intermediary (melting catalysts) decisively controls the growth of various nanostructures (such as nanotubes or graphene).[169,263] Unfortunately, previous research has only been able to focus on catalytic growth from gas-solid interfaces,[161,165,164,162,264,167] overlooking the fact that the direct observation of liquid-solid interfacial reactions is indeed the key of fully understanding the above growth model/process. Herein, we propose another solution to monitor the liquid-solid interfacial process with high resolution. We demonstrated it by in situ high-resolution TEM (HRTEM) observation of the ordering transition from amorphous carbon (a-C) to graphene layers on melting Pt_3Co surface. Pt_3Co alloy was chosen to facilitate our observation because of its high stability, low melting point and low saturated vapor pressure.[265,266] The Pt_3Co-carbon liquid-solid interface was realized by in situ heating of Pt_3Co nanoparticles supported on an a-C film upon their melting. To avoid sample drift in conventional high-temperature experiment so as to gain high resolution, the in situ observation was conducted on a JEM-2100F TEM equipped with a Protochips Aduro™ platform with heating E-Chip specimen support (the a-C film was pre-coated on the E-Chip) which is capable of providing ultra-high stability, low drift at high temperature, and accurate temperature control.

5.2 Experimental Section

5.2.1 Synthesis of Nanoparticles

Pt_3Co nanoparticles with an average diameter of ~9.5 nm were synthesized from the reduction of Pt^{4+} and Co^{2+} salts simultaneously with ethylene glycol at high temperature. Typically, 5.72 mg H_2PtCl_6 and 0.66 mg $CoCl_2$ were dissolved into 20 mL ethylene glycol (pH value was adjusted to 11 by adding NaOH) to form a homogeneous light-green solution. The solution was then transferred to a 30 mL Teflon-lined stainless steel autoclave and heated at 200 °C for 10 h. The black precipitates were then filtered and washed with deionized water, acetone and absolute alcohol alternatively to remove soluble species before drying at 70 °C in a vacuum oven overnight.

5.2.2 Design of TEM Observations

The in situ heating experiment described here was conducted on a Protochips Aduro^{TM} platform with heating E-Chip specimen support what provides atomic resolution at thermal ramp rates of up to 10^6 °C/s with highly accurate temperature control of specimen inside a TEM (Figure 5.1). The TEM sample was prepared for imaging by dispersing Pt_3Co nanoparticles onto a lacy carbon film supported by a ceramic membrane from a nanoparticle-ethanol suspension and was allowed to dry in air. TEM observation was conducted on a JEM 2100F field-emission transmission electron microscope operating at 200 kV, equipped with STEM and EDS. The sample was quickly heated to 350 °C and stayed at this temperature for ~10 minutes to remove any possible organic residuals before subsequent observations. During the observation, the image was recorded using a Gatan SC1000 ORIUS^{TM} CCD with a short exposure time (0.1 s), and the electron beam was blanked whenever possible to minimize beam effects on the nanoparticles.

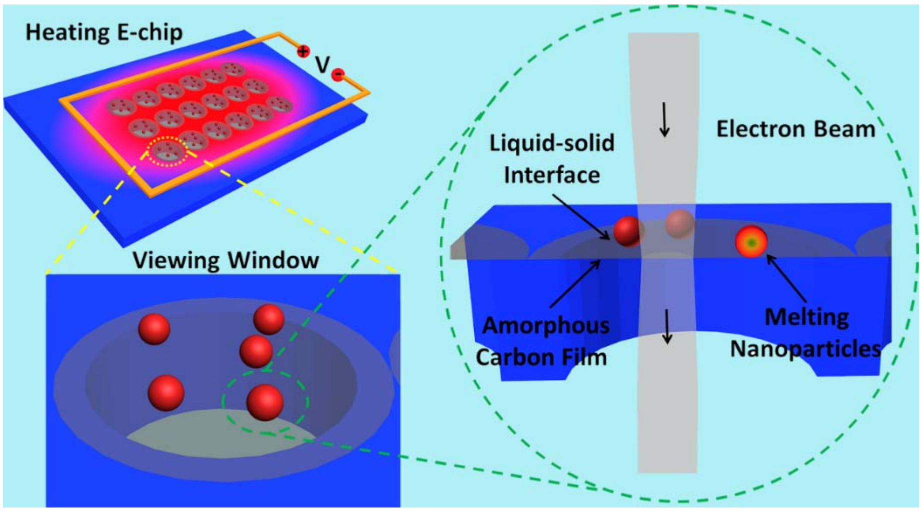

Figure 5.1 Schematic representation and operating principles of the experimental design, showing the heating E-chip, the viewing window and its cross-sectional configuration.

5.2.3 Density-functional Theory (DFT) Calculations

The relaxed progresses and calculations of self-consistent fields were all performed with Quantum ESPRESSO.[267] All structures have been relaxed with BFGS method with 1×1×1 k-points. A unit cell with 4 layers of atoms in which the uppermost layer is imperfect to simulate the steps. The energy change in diffusion progress was calculated with nudged elastic band method (NEB). The crystal plane index of the surface was (111), and the structure was the same as that of Pt_3Co. The lower two layers were fixed during the relaxed process to simulate a bulk crystal, and only the top two layers of atoms were allowed to travel to simulate the surface reconstruction of the steps and the attached carbon atom.

5.3 Experimental Results

5.3.1 Characterizations of Nanoparticles

The crystal structure of the as-synthesized nanoparticles was examined by means of XRD. The as-measured XRD pattern was shown in Figure 5.2, with that of bulk Pt_3Co crystal (cubic, JCPDS card No.: 29-0499, space group: $Pm\overline{3}m(221)$) attached as a reference. It can be seen that pure Pt particles reached diffraction peaks at 2θ of 39.6, 46.3 and 67.4 with d values of 2.26, 1.96 and 1.39 Å (corresponding to (111), (200), and (220) facets of Pt), respectively. However, diffraction peaks from Pt_3Co particles as shown in Figure 5.2 were found to have shifted in the XRD pattern towards the high degree angle region whereas diffraction peaks at 2θ of 40.5, 47.1 and 68.8 with d values of 2.22, 1.92 and 1.36 Å were assigned to Pt_3Co. Apparently, the lattice of Pt_3Co is smaller than that of Pt particles. This result could be attributed to the substitution of Pt with smaller Co atoms. The full width at half maximum (FWHM) of the diffraction peak of Pt_3Co at 40.5 was found to be 0.835 degree, thus the average diameter of the Pt_3Co particle was found to be approximately 10.0 nm based on Scherrer Equation. Using similar methods, the peak at 47.1 was 9.58 nm, and the peak at 68.8 was 9.35 nm. The average diameter of the as-synthesized nanoparticles was estimated to be ~9.5 nm.

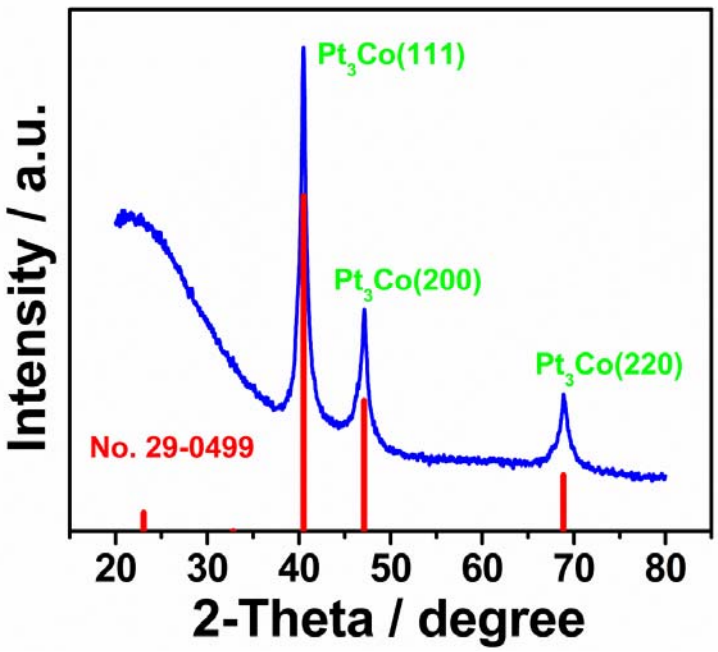

Figure 5.2 XRD profile of as-synthesized Pt_3Co nanoparticles.

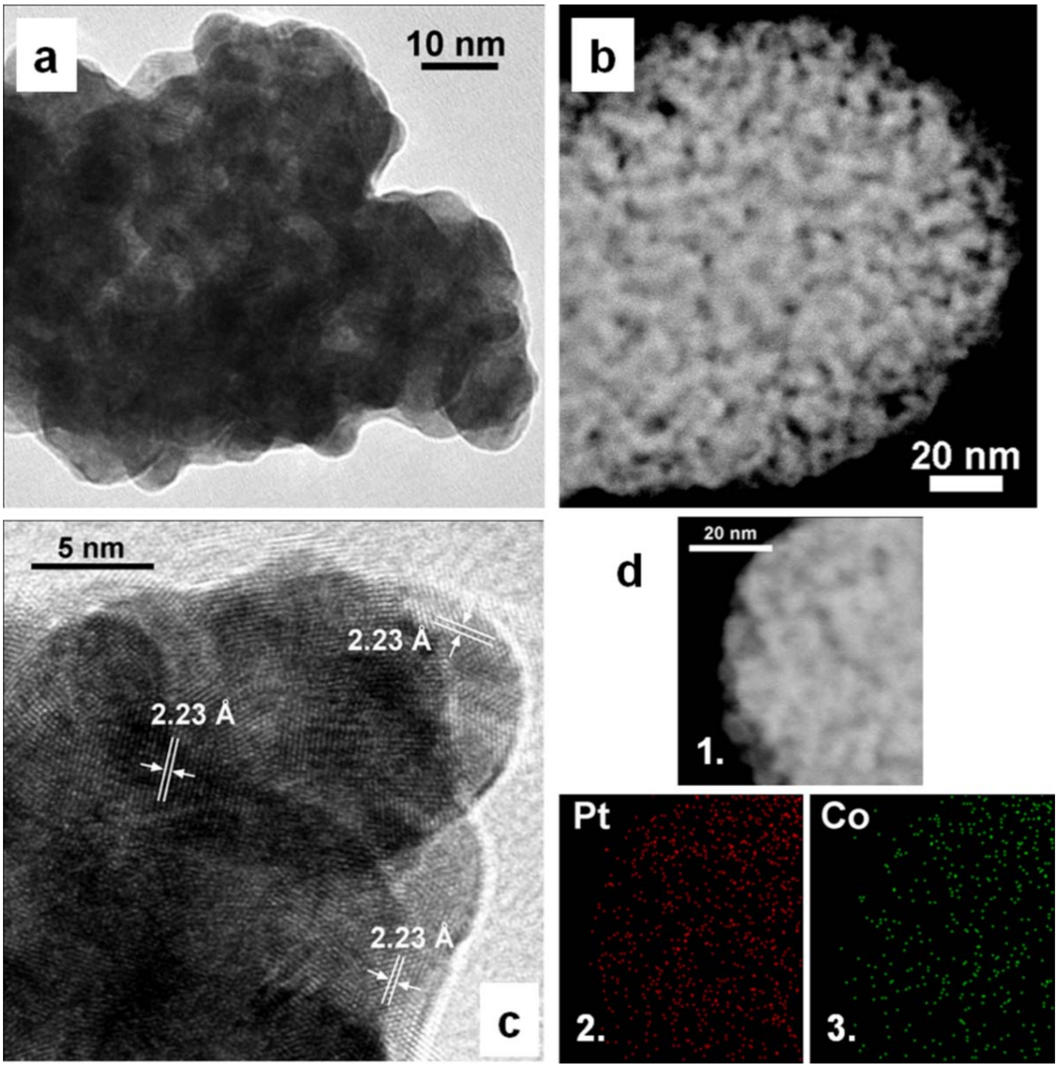

Figure 5.3 TEM characterizations of as-synthesized Pt_3Co nanoparticles. (a) Bright-field TEM images and (b) HAADF-STEM image of Pt_3Co nanoparticle clusters. (c) HRTEM image and (d) EDS elemental mapping of a small number of nanoparticles.

The bright-field TEM image (Figure 5.3a) and the HAADF STEM image (Figure 5.3b) show that most of the as-synthesized Pt_3Co nanoparticles are uniform in size and faceted in shape. An average size distribution of ~10 nm was identified, which is consistent with our XRD analysis. The HRTEM image of the representative nanoparticles is shown in Figure 5.3c**,** revealing a well-crystallized nature. Lattice fringes with a periodic lattice spacing of 0.223 nm corresponding to the Pt_3Co (111) plane are clearly visible and dominant among repeated particles. The dominance of the exposed (111) planes is in accordance with earlier results on nanosized metal particles.[268] Additionally, EDS elemental mapping **(**Figure 5.3d**)** suggests a homogenous distribution of Pt and Co elements with a rough atomic ratio of 3.

5.3.2 In-situ TEM Observations

5.3.2.1 Temperature-dependent Eutectic Behavior of Nanoparticles

In order to document the formation of carbon nanostructures on melting Pt_3Co properly, it would be essential to first study its melting behaviors due to limited data available in the literature. A survey on in situ sintering of Pt_3Co nanoparticles was therefore conducted in advance and the results were summarized in Figure 5.4. A cluster of Pt_3Co nanoparticles was chosen for examining the morphology transformation induced by increasing temperature in the present study. The following intervals are derived from the observed changes as the temperature increases.

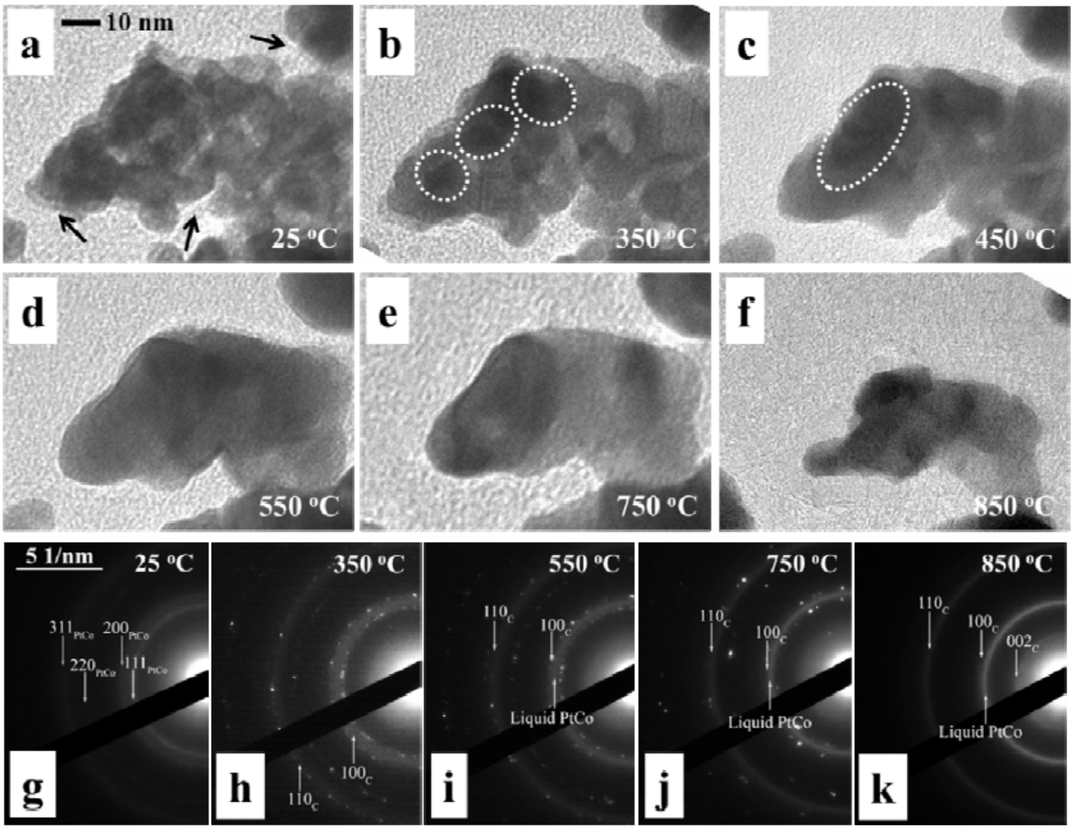

Figure 5.4 Image sequences showing typical dynamics during heating of Pt_3Co nanoparticles. (a-f) illustrate the evaporation of organic residuals, and the coalescing, and macroscopic melting of Pt_3Co nanocrystal agglomeration. The scale bar of (a) also applies to (b-f). (g-k) represent the corresponding selected-area electron diffraction (SAED) patterns upon image area at chosen temperatures. The scale bar of g also applies to (h-k).

I. Evaporation of organic residuals (25 °C – 350 °C).

To completely remove the organic residuals, i.e. to ensure a “clean” reaction environment for the following catalytic reaction, the sample was quickly heated to

350 ^{o}C and was kept at this temperature for about 10 minutes. In comparison with the image recorded at 25 ^{o}C (Figure 5.4a), it is rather obvious that the width of the agglomeration decreased when the temperature reached 350 ^{o}C while the edges of the nanoparticles became more visible (Figure 5.4b). These phenomena can be attributed to the vaporization of organic residuals between crystallites and the rearrangement of Pt_3Co nanoparticles located on the first layer adjacent to the supporting carbon film. Another interesting finding is that some organic passivating surface layers (~1 nm) could be identified through phase contrast imaging in Figure 5.4a (as indicated by black arrows)yet these layers all vanished in Figure 5.4b. This observation should verify the complete removal of organic residuals. Under such clean reaction environment, the configuration of the SAED patterns (Figure 5.4g & Figure 5.4h) remained mostly unchanged apart from some minor contrast enhancement, which can both be well indexed to cubic Pt_3Co and amorphous carbon as shown.

II. Coalescence of neighboring crystals via oriented attachment (350 ^{o}C – 550 ^{o}C).

It should be noted that patches of dark contrast (as indicated by white dashed ovals) could be found in Figure 5.4b. These patterns, known as Moiré interference patterns,[269,270] occur when two lattices overlap with a rotational mis-orientation. Several groups of Moiré fringes appeared abruptly between the adjacent crystals when the sample was heated to 350 ^{o}C as shown in Figure 5.4b. However, these fringes disappeared upon further heating to 450 °C (Figure 5.4c). It can also been seen that the contrast of the same area where the Moiré fringes used to appear at 350 °C in Figure 5.4c (as indicated by a white dashed oval) have become increasingly uniform, implying that the nanoparticles underwent a neighboring coalescing process via oriented attachment mechanism.[271,272]

III. Melting of Pt_3Co nanoclusters (550 °C – 850 °C).

As shown in Figure 5.4d, when the sample was heated to 550 °C, the corresponding SAED pattern (Figure 5.4i) show three halo rings. An analysis of the halo rings suggests that the two outer halo rings were due to the amorphous carbon film, whereas the inner one was resulted from the liquid Pt_3Co compound.[273] Meanwhile, the cubic Pt_3Co crystals represented by bright Debye-Scherrer rings continue to be visible, suggesting initial surface melting could have occurred at this stage. In the subsequent sintering process, the temperature was increased very slowly. When the temperature reached 750 °C as shown in Figure 5.4j, the series of Debye-Scherrer rings became much weaker, leaving some bright spots which indicate the occurrence of further melting towards the core-part within the crystals. As shown in Figure 5.4f and Figure 5.4k, the Debye-Scherrer rings vanish completely at 850 °C while the contrast of the halo ring from liquid Pt_3Co has become rather dominant in the SAED pattern, implying the nanoclusters are fully melted at this point. Interestingly, another halo ring has become so visible that it could be clearly indexed to the graphite (002) planes.

During the whole heating process, a continuous volume contraction (from Figure 5.4a to Figure 5.4f) was observed originated from the evaporation of organic residuals, coalescence of adjacent crystals, melting of particles, and gradual loss of interspaces.

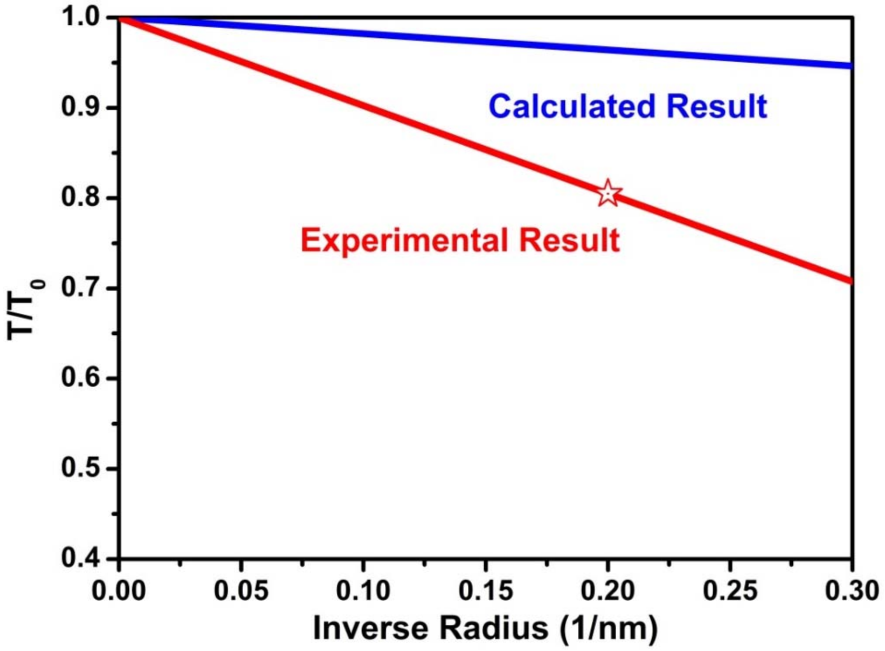

Figure 5.5 Normalized eutectic temperature T/T_0 versus inverse radius of Pt_3Co alloy nanoparticles.

The as-measured initial surface melting temperature (~550 °C) of as-synthesized Pt_3Co nanoparticles is much lower than bulk eutectic temperature (~750 °C). However, this is not surprising for Wang et al. have reported the surface melting of 8 nm pure Pt nanoparticles at ~600 °C.[274] Although research on suppression of eutectic temperature by alloying in In-Sn,[275] Pb-Bi,[276] and Ag-Pb[273] binary systems have been conducted; it is the first time that such treatment was introduced to a Pt-Co system in the present study.

Buffat and Borel developed a thermodynamic model to describe the melting behavior of small particles in pure substances,[277] which was further extended to work on the eutectic transition of a binary alloy particle.[273,278] In this model, the depression of melting temperature of small particles is derived from the phase equilibrium condition between the solid and liquid particles, leading to the following equation:

$$\frac{T}{T_0} = 1 - \frac{2}{r^{\mathrm{S}} L \rho^{\mathrm{S}}} [\gamma^{\mathrm{S}} - \gamma^{\mathrm{L}} (\frac{\rho^{\mathrm{S}}}{\rho^{\mathrm{L}}})^{2/3}]$$

where T and T_0 are the eutectic temperature of small particles and bulk sample, respectively; γ is the surface tension (the superscript "S" refers to solid phase, and "L" refers to liquid phase.); r corresponds to the particle radius; ρ is the mass density; and L is the latent heat of the eutectic transition. It is clear that there is a linear relationship between the eutectic temperature and the inverse radius of the particle.

The density of liquid and solid phases can be calculated as:

$$\rho = (w_{Pt}/\rho_{Pt} + w_{Co}/\rho_{Co})^{-1}$$

For Pt_3Co alloy, the weight fractions are: $w_{Pt} = 0.9085$, $w_{Co} = 0.0915$, so we can calculate the densities of the mixed phase: $\rho^S = 19.02$ and $\rho^L = 17.31$, and the unit is

10^3 kg/m^3. As the concentration of Co is low, the surface tension of the liquid and solid phases are estimated with pure Pt, i.e. $\gamma^S = 2.06$ J/m^2, and $\gamma^L = 1.75$ J/m^2.

The latent heat L can be calculated with this formula:

$$L = l_{0,Pt}\, w_{Pt} + l_{0,Co}\, w_{Co} + \Delta H_{mix}$$

The former two values are the latent heat of the two contents ($l_{0,Pt} = 113.7 \times 10^3$ J/kg and $l_{0,Co} = 274.9 \times 10^3$ J/kg), and ΔH_{mix} is the mixing enthalpy at the composition in experiments.

The mixing enthalpy of Co-Pt alloy is taken from ref. [279], and is calculated with spline interpolation method, as $\Delta H_{mix} = -9290$ J/mol, or -14.42×10^3 J/kg. So L = 114.0×10^3 J/kg.

With the known physical quantities, we now have:

$$\frac{T}{T_0} = 1 - \frac{1.79 \times 10^{-10}}{r^S}$$

Therefore we plot normalized eutectic temperature T/T_0 as a function of the reciprocal of the particle radius (1/nm), and the relationship is disclosed as shown in Figure 5.5 with a blue line. In comparison with the experimental result (the red line), it is obvious that the experimental result falls slightly below the calculated one. This is expected since the calculated result was obtained from the equilibrium state where the driving force of the eutectic transition ceases;[273] namely, the calculated line indeed acts as an upper limit of the practical eutectic measurement. Based on these discussions, our experimental observations are in good accordance with the theoretical results.

Throughout the experiment, it can be concluded that the initial surface melting of Pt_3Co nanoparticles occurred at around 550 °C. Then the particles continued to melt towards the core-part till ~850 °C, by which the alloy particles melted completely into liquid. The observed eutectic temperature is obviously lower than that of bulk Pt_3Co, a result of nanosized effect.[273] It should be noted that in the electron diffraction pattern at 850 °C (Figure 5.4k), an additional halo ring was observed which can be assigned to the graphite (002) planes with 0.336 nm d-spacing, suggesting the localized formation of considerable graphene layers. To understand the mechanism of carbon growth on a liquid-solid interface further, a series of experiments were conducted and the results are presented as follows.

5.3.2.2 Observations on Carbon Nanostructure Growth

In situ HRTEM image sequences were recorded against increasing temperatures and the remarkable intervals are shown in Figure 5.6 (a-d), aiming at the Pt_3Co-carbon interfaces as indicated by the white dashed box in Figure 5.6e. Initially, the HRTEM micrograph from 450 °C in Figure 5.6a reveals that well crystallized Pt_3Co nanoparticles were surrounded by a-C content. The Pt_3Co nanocrystals exhibit a faceted shape with clear periodic lattice fringes of 0.223 nm, corresponding to the

(111) planes of Pt_3Co. The temperature then rose to 550 ^oC when the surface of the Pt_3Co nanoparticles began melting as shown in Figure 5.6b. The outline of the Pt_3Co crystals was more or less retained although faint (111) fringes could still be identified in most regions. Meanwhile, the outside a-C was found to be slightly crystallized into quasi-0D nanoclusters with 0.336 nm graphite (002) planes exposed (as indicated by black arrows). More importantly, most carbon clusters were formed at the step-edges on the Pt_3Co surfaces, including either mono-atomic or multi-atomic step-edges as indicated by the white arrows shown in Figure 5.6 (b-d). A small number of carbon clusters isolated from the Pt_3Co surfaces were induced by the dissociated Pt_3Co clusters caused by the high mobility of melting surface layer.[167] As the temperature increased to 650 ^oC (Figure 5.6c), the Pt_3Co nanocrystals experienced an obvious reshaping towards spherical configurations, and the blurred lattice fringes could hardly be detected across the entire visible region due to further melting. Simultaneously, the carbon clusters around the Pt_3Co crystals aligned into larger 2D graphene sheets, with their basal (002) planes oriented parallel to the liquid-solid interface (as indicated by the dashed black ovals). A pronounced bending of the graphene layers towards the Pt_3Co step-edges was found repeatedly, confirming the origin of the carbon on this liquid-solid interface. Finally, the temperature went up to 850 ^oC when the Pt_3Co catalyst melted completely as shown in Figure 5.6d & Figure 5.6e, and a perfect layered graphite nanostructure was formed surrounding the whole Pt_3Co cluster by which underwent major volume contraction.

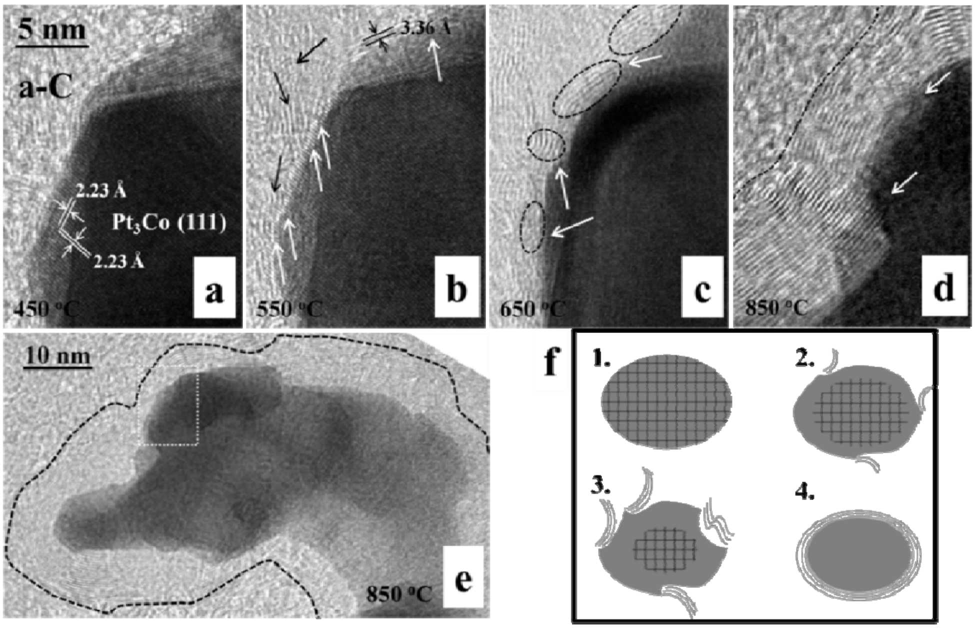

Figure 5.6 Image sequences showing the typical dynamics of formation of carbon nanostructures on melting Pt_3Co. (a-d) illustrate the carbon transformation process from amorphous carbon to quasi-0D nanoclusters, then 2D graphene, and finally 3D few-layered graphite nanostructures with increasing temperatures. The scale bar in (a) also applies to (b-d). (e) shows a panoramic micrograph of melting Pt_3Co cluster surrounded by 3D few-layered graphite at 850 °C. The dashed black line indicates external boundary of as-formed graphite nanostructures. (f) outlines the evolution.

The complete mechanism of the formation of carbon nanostructures on a liquid-solid interface was thus disclosed. The graphene nanostructure was formed on melting catalyst through edge-mediated nucleation in addition to further growth via oriented attachment (OA) [280] as outlined in Figure 5.6f. Initially, step-edges were dynamically introduced to the Pt_3Co surface upon melting, serving as nucleation centers for forming carbon nanoclusters because of the high reactivity of the step edges.[161,264] In contrast to gas-solid reactions, the as-formed carbon nanoclusters were highly mobile on the liquid-solid interface because of the high transport ability of surficial melting catalyst. Subsequently, these nanoclusters were more likely to encounter each other, and would eventually interact mutually to coalesce into 2D graphene layers by spontaneously aligning along the graphite (002) planes, known as typical OA process.[262,272] Further growth of carbon would involve transporting C clusters towards the interface and Pt_3Co atoms away from the interface. The process would eventually stop when the graphene layers have encapsulated the Pt_3Co surface to form a 3D carbon nanostructure. It should be noted that the formation of graphene layers in this process is led by the movement of the melting Pt_3Co outline caused by thermal-induced volume contraction. As a result, the process is not time-sensitive, while the final boundary of the carbon nanostructure coincides well with the original outline of the Pt_3Co cluster (see Figure 5.6e & Figure 5.4a).

5.3.3 DFT Calculation Results

In fact, defects (such as edges and dislocations) often trigger the growth of carbon crystal. Recent theoretical studies show that the formation of graphene layers should start from the edge of matrix,[281–284] and our observation agrees well with this claim. This process can be viewed as a kind of physical position selection process in growth. When the chemical environment on the edges was taken into account, certain differences between the Co atoms and the Pt atoms in the catalytic process could also be expected. To track the origin of this interfacial process, density-functional theory (DFT) calculations were made on the nucleation of carbon near the edge. The model structure is shown in Figure 5.7a, by which the deep green spheres represent Pt atoms, and the light blue spheres stand for Co atoms. We selected four specific positions A, B, C and D (with A and D being far away from the edge while B and C being connected to the edges) for the first carbon atom on the surface. We then analyzed the diffusion process at these four positions in order to determine the position of nucleation. It should be noted that B and C are connected to two different kinds of metal atoms, i.e. B is connected to a Co atom and C is connected to a Pt atom. Figure 5.7b shows the energy change in the diffusion of one carbon atom at these four positions (the energy of position A is set to zero). Generally, lower energy suggests a more stable state and lower potential barrier implies more efficient and effective diffusion. It can be seen from Figure 4.7b that position B has the lowest energy level of ~-0.5 eV, while the energy levels of positions A, C, and D are very similar to each other. The results suggest that if the first carbon is connected to a Co atom, the structure will possess least energy and thus, be most stable. The findings from the potential barriers also show that the diffusion from A to B is more efficient than that from A to C. Considering position B can also minimize the total amount of energy, we deduce that position B should be the nucleation position for the growth of graphite layers. In other words, the growth of graphite on Pt_3Co alloy surface will nucleate from Co atoms on edge steps, which could be regarded as a kind of chemical position selection effect of nucleation.

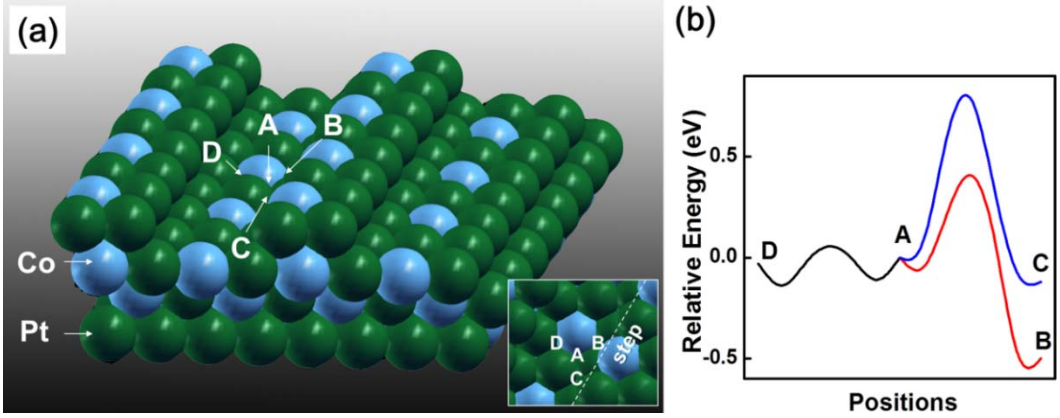

Figure 5.7 Illustration of the nucleation process on the Pt_3Co (111) surface modeled in density-functional theory calculations. (a) The model includes 2×2 units and specific positions of the first carbon atom; insert shows the top view. (b) Energy change in the diffusion process of the first carbon atom from A-B, A-C and A-D.

5.3.4 Discussion on the potential applications of our method

In our study, the amorphous carbon film was pre-coated on the heating E-chip by vacuum evaporation technique to realize the observation of Pt_3Co-C liquid-solid process. In fact, the carbon here can be changed to other amorphous content (such as Si et al.) through the same deposition technique, and the Pt_3Co nanoparticles can be replaced by other semiconductor/metallic nanostructures, to visualize purposed dynamic liquid-solid processes.

In case of monitoring reactions between crystalline materials with liquid intermediaries, inert polymeric supports can be chosen (such as PVF) so that two (or more) different materials in the form of nanoparticles/nanowires/nanotubes can be mixed and deposited on the polymer support for in situ heating and observation. In association with other TEM techniques such as HAADF-STEM (high angle annular dark-field scanning TEM), EDS (energy dispersive spectrum) elemental mapping and three-dimensional tomography, different nanoparticles or even different atoms can be identified in a dynamic process at high resolution.

In short, our as-developed method is all set to be applied in other liquid-solid processes with atomic precision and more interesting results can be expected from further works.

5.4 Summary

In summary, this study presents a combination of in situ HRTEM observations and DFT simulations to resolve graphene nucleation and growth on liquid-solid interface for the first time, offering valuable insights into Pt_3Co-C system with atomic precision. Carbon clusters were found to nucleate near Co atoms at the step-edges on the surface of Pt_3Co, a result of associated physical and chemical position selections. Further growth of graphene layers from clusters is of a kinetic nature, guided by classic OA theory. This unique simultaneous nucleation and merging process of carbon growth differ greatly from those in liquid-gas interactions where carbon fibers/tubes are developed gradually from single-defect due to a constant carbon supply from the environment. As the mechanism was thoroughly identified with simple TEM configuration as such, our developed technique should be of general importance for understanding liquid-solid reactions, and should inspire further attempt to tailor the growth of carbon nanostructures and other materials in future.

CHAPTER 6 CONCLUSIONS AND FUTURE OUTLOOK

6.1 Conclusions

In this thesis, we have successfully developed several carbon-based nanocomposites via various chemical approaches, and their performances in energy storage and environmental applications have also been thoroughly examined. To understand the growth mechanism of carbon nanostructures, we have further designed and conducted an in-situ TEM experiment to capture the dynamic process for documentation.

By combining the ball-milling process and solid-state carbothermal reductive reaction, we first synthesized a novel LVP/C composite with a new- “core/shell” configuration concept through integrating porous carbon nanoflakes on single-crystalline LVP microrods. The resulting composite showed superior rate capability and improved cycling stability upon evaluation as cathode material in lithium ion batteries. It should be noted that this novel composite displayed an exceptionally high tap density, implying a high volumetric capacity for its future applications.

To further improve the electrochemical performance of the LVP/C composite, especially for high-power usage, another composite architecture was designed and synthesized via surfactant-assisted hydrothermal reaction with carbothermal reduction technique. A nanocomposite composed of LVP nanospheres embedded in hierarchically porous carbon matrix exhibited significantly improved electrochemical performance, such as long-term stability upon cycling, superior rate capability, and high discharge capacity when compared to previous LVP-based cathode materials.

In pursuit of solving various air and water pollution issues, we also fabricated a nanocomposite via electrospinning technique followed by hydrothermal treatment. The material was composed of porous Nb_2O_5 nanofibers decorated with graphene nanoclusters on their surfaces, and was applied as visible light photocatalyst for the degradation of organic dyes in aqueous solution. Such composite structure has significantly extended the active region of Nb_2O_5 from UV region to UV-Vis region, and hence, showed greatly improved photocatalytic performance when compared with pure Nb_2O_5 and Nb_2O_5/carbon core-shell nanostructures.

In addition, to understand the growth mechanism of carbon nanostructures in carbon-based composites, we have made direct observations on the transition of amorphous carbon into graphene nanostructures at liquid-solid interfaces by using high resolution TEM equipped with a heating platform. We found that the amorphous carbon first nucleated into nanoclusters at step-edges on the host particle surface before merging into graphene layers through kinetic restructuring via oriented-attachment. This observation has led to a unprecedented clear picture of the formation mechanism of few-layer graphene along the liquid-solid interface.

6.2 Future Outlook

As presented in this thesis, a series of carbon-based nanocomposites (LVP/C and Nb_2O_5/C) have been designed and fabricated with corresponding chemical methods, and showed significantly enhanced performance in their respective application scenarios. However, as research on carbon-based nanocomposites for energy storage and environmental applications are still at an early stage, a number of fundamental questions remain to be addressed and below are some of the areas that require further research:

- For large-scale practical applications, a simple, reliable, cost-effective, eco-friendly method for synthesizing carbon-based nanocomposites would be much desirable. The wet chemical preparation routes employed in this thesis, including ball-milling with carbothermal reaction, hydrothermal-carbothermal reaction, and electrospinning with hydrothermal reaction, were all chosen upon this consideration. However, one main limitation with these methods is strict reaction conditions. It would be essential to further optimize the current wet chemical processes for mass industrial mass production.

- It is expected that the performance of carbon-based composites including LVP/C and Nb_2O_5/C will continue to improve in future yet the introduction of excess carbon could lead to a significant decrease of the active material content in the composite and affects the overall performance. To address this issue, the development of novel carbon coating methods, or the design of rational nanoarchitectures is needed in order to synthesize high-performance nanocomposite with less carbon.

- Researchers are always in search for new material systems to strive for better performance. For example, the newly emerged lithium-sulfur batteries, which possess a supreme energy density with a theoretical value up to ~2600 Wh kg^{-1} (calculated based on Li anode and S cathode), have received increasing attention as potential candidate for next-generation energy storage applications, opening up a new era for battery research. With the rapid advancement of organic science, we anticipate more high performance material systems will be discovered and synthesized for both energy storage and environmental applications in future.

.

REFERENCES

(1) Dunn, B.; Kamath, H.; Tarascon, J.-M. Electrical Energy Storage for the Grid: A Battery of Choices. *Science* **2011**, *334*, 928–935.

(2) Scrosati, B. Challenge of Portable Power. *Nature* **1995**, *373*, 557–558.

(3) Guo, Y.-G.; Hu, J.-S.; Wan, L.-J. Nanostructured Materials for Electrochemical Energy Conversion and Storage Devices. *Adv. Mater.* **2008**, *20*, 2878–2887.

(4) Ji, L.; Lin, Z.; Alcoutlabi, M.; Zhang, X. Recent Developments in Nanostructured Anode Materials for Rechargeable Lithium-Ion Batteries. *Energy Environ. Sci.* **2011**, *4*, 2682.

(5) Cheng, F.; Liang, J.; Tao, Z.; Chen, J. Functional Materials for Rechargeable Batteries. *Adv. Mater.* **2011**, *23*, 1695–1715.

(6) Chan, C. K.; Peng, H.; Liu, G.; McIlwrath, K.; Zhang, X. F.; Huggins, R. A.; Cui, Y. High-Performance Lithium Battery Anodes Using Silicon Nanowires. *Nat. Nanotechnol.* **2008**, *3*, 31–35.

(7) Magasinski, A.; Dixon, P.; Hertzberg, B.; Kvit, A.; Ayala, J.; Yushin, G. High-Performance Lithium-Ion Anodes Using a Hierarchical Bottom-up Approach. *Nat. Mater.* **2010**, *9*, 353–358.

(8) Idota, Y.; Kubota, T.; Matsufuji, A.; Maekawa, Y.; Miyasaka, T. Tin-Based Amorphous Oxide: A High-Capacity Lithium-Ion-Storage Material. *Science* **1997**, *276*, 1395–1397.

(9) Lee, K. T.; Jung, Y. S.; Oh, S. M. Synthesis of Tin-Encapsulated Spherical Hollow Carbon for Anode Material in Lithium Secondary Batteries. *J. Am. Chem. Soc.* **2003**, *125*, 5652–5653.

(10) Yu, Y.; Yan, C.; Gu, L.; Lang, X.; Tang, K.; Zhang, L.; Hou, Y.; Wang, Z.; Chen, M. W.; Schmidt, O. G.; *et al.* Three-Dimensional (3D) Bicontinuous Au/Amorphous-Ge Thin Films as Fast and High-Capacity Anodes for Lithium-Ion Batteries. *Adv. Energy Mater.* **2013**, *3*, 281–285.

(11) Abel, P. R.; Chockla, A. M.; Lin, Y.-M.; Holmberg, V. C.; Harris, J. T.; Korgel, B. A.; Heller, A.; Mullins, C. B. Nanostructured Si($_1$-x)Gex for Tunable Thin Film Lithium-Ion Battery Anodes. *ACS Nano* **2013**, *7*, 2249–2257.

(12) Chan, C. K.; Zhang, X. F.; Cui, Y. High Capacity Li Ion Battery Anodes Using Ge Nanowires. *Nano Lett.* **2008**, *8*, 307–309.

(13) Lou, X. W.; Wang, Y.; Yuan, C.; Lee, J. Y.; Archer, L. A. Template-Free Synthesis of SnO2 Hollow Nanostructures with High Lithium Storage Capacity. *Adv. Mater.* **2006**, *18*, 2325–2329.

(14) Shi, W.; Rui, X.; Zhu, J.; Yan, Q. Design of Nanostructured Hybrid Materials Based on Carbon and Metal Oxides for Li Ion Batteries. *J. Phys. Chem. C* **2012**, *116*, 26685–26693.

(15) Xu, C.; Zeng, Y.; Rui, X.; Xiao, N.; Zhu, J.; Zhang, W.; Chen, J.; Liu, W.; Tan, H.; Hng, H. H.; *et al.* Controlled Soft-Template Synthesis of Ultrathin C@FeS Nanosheets with High-Li-Storage Performance. *ACS Nano* **2012**, *6*, 4713–4721.

(16) Zhu, J.; Yin, Z.; Yang, D.; Sun, T.; Yu, H.; Hoster, H. E.; Hng, H. H.; Zhang, H.; Yan, Q. Hierarchical Hollow Spheres Composed of Ultrathin Fe2O3 Nanosheets for Lithium Storage and Photocatalytic Water Oxidation. *Energy Environ. Sci.* **2013**, *6*, 987.

(17) Huang, H.; Liu, Y.; Wang, J.; Gao, M.; Peng, X.; Ye, Z. Self-Assembly of Mesoporous CuO Nanosheets-CNT 3D-Network Composites for Lithium-Ion Batteries. *Nanoscale* **2013**, *5*, 1785–1788.

(18) Ellis, B. L.; Lee, K. T.; Nazar, L. F. Positive Electrode Materials for Li-Ion and Li-Batteries. *Chem. Mater.* **2010**, *22*, 691–714.

(19) Mizushima, K.; Jones, P. C.; Wiseman, P. J.; Goodenough, J. B. LixCoO2 (0<x<1): A New Cathode Material for Batteries of High Energy Density. *Mater. Res. Bull.* **1980**, *15*, 783–789.

(20) ANTOLINI, E. LiCoO2: Formation, Structure, Lithium and Oxygen Nonstoichiometry, Electrochemical Behaviour and Transport Properties. *Solid State Ionics* **2004**, *170*, 159–171.

(21) Yang, C.; Huang, J.; Huang, L.; Wang, G. Electrochemical Performance of LiCo1/3Mn1/3Ni1/3O2 Hollow Spheres as Cathode Material for Lithium Ion Batteries. *J. Power Sources* **2013**, *226*, 219–222.

(22) Thackeray, M. M.; David, W. I. F.; Bruce, P. G.; Goodenough, J. B. Lithium Insertion into Manganese Spinels. *Mater. Res. Bull.* **1983**, *18*, 461–472.

(23) Tang, W.; Hou, Y.; Wang, F.; Liu, L.; Wu, Y.; Zhu, K. LiMn2O4 Nanotube as Cathode Material of Second-Level Charge Capability for Aqueous Rechargeable Batteries. *Nano Lett.* **2013**, *13*, 2036–2040.

(24) Wu, Y.; Wen, Z.; Feng, H.; Li, J. Hollow Porous LiMn2O4 Microcubes as Rechargeable Lithium Battery Cathode with High Electrochemical Performance. *Small* **2012**, *8*, 858–862.

(25) Tarascon, J. M.; Wang, E.; Shokoohi, F. K.; McKinnon, W. R.; Colson, S. The Spinel Phase of LiMn2O4 as a Cathode in Secondary Lithium Cells. *J. Electrochem. Soc.* **1991**, *138*, 2859.

(26) Gummow, R. J.; de Kock, A.; Thackeray, M. M. Improved Capacity Retention in Rechargeable 4 V Lithium/lithium-Manganese Oxide (spinel) Cells. *Solid State Ionics* **1994**, *69*, 59–67.

(27) Deng, B.; Nakamura, H.; Yoshio, M. Capacity Fading with Oxygen Loss for Manganese Spinels upon Cycling at Elevated Temperatures. *J. Power Sources* **2008**, *180*, 864–868.

(28) Chung, K. Y.; Kim, K.-B. Investigations into Capacity Fading as a Result of a Jahn–Teller Distortion in 4V LiMn2O4 Thin Film Electrodes. *Electrochim. Acta* **2004**, *49*, 3327–3337.

(29) Santhanam, R.; Rambabu, B. Research Progress in High Voltage Spinel LiNi0.5Mn1.5O4 Material. *J. Power Sources* **2010**, *195*, 5442–5451.

(30) Yamada, A.; Iwane, N.; Harada, Y.; Nishimura, S.; Koyama, Y.; Tanaka, I. Lithium Iron Borates as High-Capacity Battery Electrodes. *Adv. Mater.* **2010**, *22*, 3583–3587.

(31) Barpanda, P.; Ati, M.; Melot, B. C.; Rousse, G.; Chotard, J.-N.; Doublet, M.-L.; Sougrati, M. T.; Corr, S. A.; Jumas, J.-C.; Tarascon, J.-M. A 3.90 V Iron-Based Fluorosulphate Material for Lithium-Ion Batteries Crystallizing in the Triplite Structure. *Nat. Mater.* **2011**, *10*, 772–779.

(32) Recham, N.; Chotard, J.-N.; Dupont, L.; Delacourt, C.; Walker, W.; Armand, M.; Tarascon, J.-M. A 3.6 V Lithium-Based Fluorosulphate Insertion Positive Electrode for Lithium-Ion Batteries. *Nat. Mater.* **2010**, *9*, 68–74.

(33) Rangappa, D.; Murukanahally, K. D.; Tomai, T.; Unemoto, A.; Honma, I. Ultrathin Nanosheets of Li2MSiO4 (M = Fe, Mn) as High-Capacity Li-Ion Battery Electrode. *Nano Lett.* **2012**, *12*, 1146–1151.

(34) Nytén, A.; Abouimrane, A.; Armand, M.; Gustafsson, T.; Thomas, J. O. Electrochemical Performance of Li2FeSiO4 as a New Li-Battery Cathode Material. *Electrochem. commun.* **2005**, *7*, 156–160.

(35) Lv, D.; Bai, J.; Zhang, P.; Wu, S.; Li, Y.; Wen, W.; Jiang, Z.; Mi, J.; Zhu, Z.; Yang, Y. Understanding the High Capacity of Li2FeSiO4: In Situ XRD/XANES Study Combined with First-Principles Calculations. *Chem. Mater.* **2013**, *25*, 2014–2020.

(36) Padhi, A. K.; Nanjundaswamy, K. S.; Goodenough, J. B. Phospho-Olivines as Positive-Electrode Materials for Rechargeable Lithium Batteries. *J. Electrochem. Soc.* **1997**, *144*, 1188.

(37) Carriazo, D.; Rossell, M. D.; Zeng, G.; Bilecka, I.; Erni, R.; Niederberger, M. Formation Mechanism of LiFePO4 Sticks Grown by a Microwave-Assisted Liquid-Phase Process. *Small* **2012**, *8*, 2231–2238.

(38) Cogswell, D. A.; Bazant, M. Z. Coherency Strain and the Kinetics of Phase Separation in LiFePO4 Nanoparticles. *ACS Nano* **2012**, *6*, 2215–2225.

(39) Kang, B.; Ceder, G. Battery Materials for Ultrafast Charging and Discharging. *Nature* **2009**, *458*, 190–193.

(40) Chung, S.-Y.; Bloking, J. T.; Chiang, Y.-M. Electronically Conductive Phospho-Olivines as Lithium Storage Electrodes. *Nat. Mater.* **2002**, *1*, 123–128.

(41) Wang, Y.; Wang, Y.; Hosono, E.; Wang, K.; Zhou, H. The Design of a LiFePO4/carbon Nanocomposite with a Core-Shell Structure and Its Synthesis by an in Situ Polymerization Restriction Method. *Angew. Chem. Int. Ed.* **2008**, *47*, 7461–7465.

(42) Wang, J.; Sun, X. Understanding and Recent Development of Carbon Coating on LiFePO4 Cathode Materials for Lithium-Ion Batteries. *Energy Environ. Sci.* **2012**, *5*, 5163.

(43) Wang, Y.; He, P.; Zhou, H. Olivine LiFePO4: Development and Future. *Energy Environ. Sci.* **2011**, *4*, 805–817.

(44) Chen, Z.; Qin, Y.; Amine, K.; Sun, Y.-K. Role of Surface Coating on Cathode Materials for Lithium-Ion Batteries. *J. Mater. Chem.* **2010**, *20*, 7606–7612.

(45) Fergus, J. W. Recent Developments in Cathode Materials for Lithium Ion Batteries. *J. Power Sources* **2010**, *195*, 939–954.

(46) Song, H.-K.; Lee, K. T.; Kim, M. G.; Nazar, L. F.; Cho, J. Recent Progress in Nanostructured Cathode Materials for Lithium Secondary Batteries. *Adv. Funct. Mater.* **2010**, *20*, 3818–3834.

(47) Andersson, A.; Thomas, J. The Source of First-Cycle Capacity Loss in LiFePO4. *J. Power Sources* **2001**, *97-98*, 498–502.

(48) Qian, J.; Zhou, M.; Cao, Y.; Ai, X.; Yang, H. Template-Free Hydrothermal Synthesis of Nanoembossed Mesoporous LiFePO4 Microspheres for High-Performance Lithium-Ion Batteries. *J. Phys. Chem. C* **2010**, *114*, 3477–3482.

(49) Dominko, R.; Goupil, J. M.; Bele, M.; Gaberscek, M.; Remskar, M.; Hanzel, D.; Jamnik, J. Impact of LiFePO4⁄C Composites Porosity on Their Electrochemical Performance. *J. Electrochem. Soc.* **2005**, *152*, A858.

(50) Doherty, C. M.; Caruso, R. A.; Smarsly, B. M.; Drummond, C. J. Colloidal Crystal Templating to Produce Hierarchically Porous LiFePO4 Electrode Materials for High Power Lithium Ion Batteries. *Chem. Mater.* **2009**, *21*, 2895–2903.

(51) Chung, S.-Y.; Chiang, Y.-M. Microscale Measurements of the Electrical Conductivity of Doped LiFePO4. *Electrochem. Solid-State Lett.* **2003**, *6*, A278.

(52) Liu, H.; Li, C.; Cao, Q.; Wu, Y. P.; Holze, R. Effects of Heteroatoms on Doped LiFePO4/C Composites. *J. Solid State Electrochem.* **2007**, *12*, 1017–1020.

(53) Abbate, M.; Lala, S. M.; Montoro, L. A.; Rosolen, J. M. Ti-, Al-, and Cu-Doping Induced Gap States in LiFePO4. *Electrochem. Solid-State Lett.* **2005**, *8*, A288.

(54) Ma, J.; Li, B.; Du, H.; Xu, C.; Kang, F. Effects of Tin Doping on Physicochemical and Electrochemical Performances of LiFe1−xSnxPO4/C (0≤x≤0.07) Composite Cathode Materials. *Electrochim. Acta* **2011**, *56*, 7385–7391.

(55) Whittingham, M. S. Lithium Batteries and Cathode Materials. *Chem. Rev.* **2004**, *104*, 4271–4302.

(56) Aricò, A. S.; Bruce, P.; Scrosati, B.; Tarascon, J.-M.; van Schalkwijk, W. Nanostructured Materials for Advanced Energy Conversion and Storage Devices. *Nat. Mater.* **2005**, *4*, 366–377.

(57) Wang, Y.; Cao, G. Developments in Nanostructured Cathode Materials for High-Performance Lithium-Ion Batteries. *Adv. Mater.* **2008**, *20*, 2251–2269.

(58) Liu, C.; Li, F.; Ma, L.-P.; Cheng, H.-M. Advanced Materials for Energy Storage. *Adv. Mater.* **2010**, *22*, E28–E62.

(59) Pivko, M.; Bele, M.; Tchernychova, E.; Logar, N. Z.; Dominko, R.; Gaberscek, M. Synthesis of Nanometric LiMnPO4 via a Two-Step Technique. *Chem. Mater.* **2012**, *24*, 1041–1047.

(60) Wolfenstine, J.; Allen, J. Ni3+/Ni2+ Redox Potential in LiNiPO4. *J. Power Sources* **2005**, *142*, 389–390.

(61) Saïdi, M. Y.; Barker, J.; Huang, H.; Swoyer, J. L.; Adamson, G. Electrochemical Properties of Lithium Vanadium Phosphate as a Cathode Material for Lithium-Ion Batteries. *Electrochem. Solid-State Lett.* **2002**, *5*, A149.

(62) Rui, X.; Yan, Q.; Skyllas-Kazacos, M.; Lim, T. M. Li3V2(PO4)3 Cathode Materials for Lithium-Ion Batteries: A Review. *J. Power Sources* **2014**, *258*, 19–38.

(63) Hu, M.; Pang, X.; Zhou, Z. Recent Progress in High-Voltage Lithium Ion Batteries. *J. Power Sources* **2013**, *237*, 229–242.

(64) Yin, S.-C.; Grondey, H.; Strobel, P.; Anne, M.; Nazar, L. F. Electrochemical Property: Structure Relationships in Monoclinic Li(3-y)V2(PO4)3. *J. Am. Chem. Soc.* **2003**, *125*, 10402–10411.

(65) Padhi, A. K.; Nanjundaswamy, K. S.; Masquelier, C.; Goodenough, J. B. Mapping of Transition Metal Redox Energies in Phosphates with NASICON Structure by Lithium Intercalation. *J. Electrochem. Soc.* **1997**, *144*, 2581.

(66) Gaubicher, J.; Wurm, C.; Goward, G.; Masquelier, C.; Nazar, L. Rhombohedral Form of Li3V2(PO4)3 as a Cathode in Li-Ion Batteries. *Chem. Mater.* **2000**, *12*, 3240–3242.

(67) Huang, H.; Yin, S.-C.; Kerr, T.; Taylor, N.; Nazar, L. F. Nanostructured Composites: A High Capacity, Fast Rate Li3V2(PO4)3/Carbon Cathode for Rechargeable Lithium Batteries. *Adv. Mater.* **2002**, *14*, 1525–1528.

(68) Cahill, L. S.; Chapman, R. P.; Britten, J. F.; Goward, G. R. (7)Li NMR and Two-Dimensional Exchange Study of Lithium Dynamics in Monoclinic Li3V2(PO4)3. *J. Phys. Chem. B* **2006**, *110*, 7171–7177.

(69) Verhoeven, V.; de Schepper, I.; Nachtegaal, G.; Kentgens, A.; Kelder, E.; Schoonman, J.; Mulder, F. Lithium Dynamics in LiMn2O4 Probed Directly by Two-Dimensional 7Li NMR. *Phys. Rev. Lett.* **2001**, *86*, 4314–4317.

(70) Sato, M.; Ohkawa, H.; Yoshida, K.; Saito, M.; Uematsu, K.; Toda, K. Enhancement of Discharge Capacity of Li3V2(PO4)3 by Stabilizing the Orthorhombic Phase at Room Temperature. *Solid State Ionics* **2000**, *135*, 137–142.

(71) Ohkawa, H.; Yoshida, K.; Saito, M.; Uematsu, K.; Toda, K.; Sato, M. Improvement of Discharge Capacity of .BETA.-Fe2(SO4)3-Type Li3V2(PO4)3 by Stabilizing High Temperature Orthorhombic Phase at Room Temperature. *Chem. Lett.* **1999**, 1017–1018.

(72) Membreño, N.; Xiao, P.; Park, K.-S.; Goodenough, J. B.; Henkelman, G.; Stevenson, K. J. In Situ Raman Study of Phase Stability of Α-Li3V2(PO4)3 upon Thermal and Laser Heating. *J. Phys. Chem. C* **2013**, *117*, 11994–12002.

(73) Patoux, S.; Wurm, C.; Morcrette, M.; Rousse, G.; Masquelier, C. A Comparative Structural and Electrochemical Study of Monoclinic Li3Fe2(PO4)3 and Li3V2(PO4)3. *J. Power Sources* **2003**, *119-121*, 278–284.

(74) BURBA, C.; FRECH, R. Vibrational Spectroscopic Studies of Monoclinic and Rhombohedral Li3V2(PO4)3. *Solid State Ionics* **2007**, *177*, 3445–3454.

(75) Morcrette, M.; Leriche, J.-B.; Patoux, S.; Wurm, C.; Masquelier, C. In Situ X-Ray Diffraction during Lithium Extraction from Rhombohedral and Monoclinic Li3V2(PO4)3. *Electrochem. Solid-State Lett.* **2003**, *6*, A80.

(76) Lu, Y.; Wang, L.; Song, J.; Zhang, D.; Xu, M.; Goodenough, J. B. Aluminum-Stabilized NASICON-Structured Li3V2(PO4)3. *J. Mater. Chem. A* **2013**, *1*, 68.

(77) Yin, S.-C.; Strobel, P. S.; Grondey, H.; Nazar, L. F. Li2.5V2(PO4)3 : A Room-Temperature Analogue to the Fast-Ion Conducting High-Temperature Γ-Phase of Li3V2(PO4)3. *Chem. Mater.* **2004**, *16*, 1456–1465.

(78) Yoon, J.; Muhammad, S.; Jang, D.; Sivakumar, N.; Kim, J.; Jang, W.-H.; Lee, Y.-S.; Park, Y.-U.; Kang, K.; Yoon, W.-S. Study on Structure and Electrochemical Properties of Carbon-Coated Monoclinic Li3V2(PO4)3 Using Synchrotron Based in Situ X-Ray Diffraction and Absorption. *J. Alloys Compd.* **2013**, *569*, 76–81.

(79) Yin, S.-C.; Grondey, H.; Strobel, P.; Huang, H.; Nazar, L. F. Charge Ordering in Lithium Vanadium Phosphates: Electrode Materials for Lithium-Ion Batteries. *J. Am. Chem. Soc.* **2003**, *125*, 326–327.

(80) Andersson, A. S.; Kalska, B.; Häggström, L.; Thomas, J. O. Lithium Extraction/insertion in LiFePO4: An X-Ray Diffraction and Mössbauer Spectroscopy Study. *Solid State Ionics* **2000**, *130*, 41–52.

(81) Li, Y.; Zhou, Z.; Ren, M.; Gao, X.; Yan, J. Electrochemical Performance of Nanocrystalline Li3V2(PO4)3/carbon Composite Material Synthesized by a Novel Sol–gel Method. *Electrochim. Acta* **2006**, *51*, 6498–6502.

(82) Pan, A.; Liu, J.; Zhang, J.-G.; Xu, W.; Cao, G.; Nie, Z.; Arey, B. W.; Liang, S. Nano-Structured Li3V2(PO4)3/carbon Composite for High-Rate Lithium-Ion Batteries. *Electrochem. commun.* **2010**, *12*, 1674–1677.

(83) Du, X.; He, W.; Zhang, X.; Yue, Y.; Liu, H.; Zhang, X.; Min, D.; Ge, X.; Du, Y. Enhancing the Electrochemical Performance of Lithium Ion Batteries Using Mesoporous Li3V2(PO4)3/C Microspheres. *J. Mater. Chem.* **2012**, *22*, 5960.

(84) Chang, C.; Xiang, J.; Shi, X.; Han, X.; Yuan, L.; Sun, J. Hydrothermal Synthesis of Carbon-Coated Lithium Vanadium Phosphate. *Electrochim. Acta* **2008**, *54*, 623–627.

(85) Wang, L.; Zhang, L.-C.; Lieberwirth, I.; Xu, H.-W.; Chen, C.-H. A Li3V2(PO4)3/C Thin Film with High Rate Capability as a Cathode Material for Lithium-Ion Batteries. *Electrochem. commun.* **2010**, *12*, 52–55.

(86) Zhou, X.; Liu, Y.; Guo, Y. Effect of Reduction Agent on the Performance of Li3V2(PO4)3/C Positive Material by One-Step Solid-State Reaction. *Electrochim. Acta* **2009**, *54*, 2253–2258.

(87) Zhong, S.; Wang, J.; Liu, L.; Liu, J.; Li, Y. Investigations on the Synthesis and Electrochemical Performance of Li3V2(PO4)3/C by Different Methods. *Ionics* **2009**, *16*, 117–121.

(88) Rui, X. H.; Li, C.; Liu, J.; Cheng, T.; Chen, C. H. The Li3V2(PO4)3/C Composites with High-Rate Capability Prepared by a Maltose-Based Sol–gel Route. *Electrochim. Acta* **2010**, *55*, 6761–6767.

(89) Rui, X. H.; Ding, N.; Liu, J.; Li, C.; Chen, C. H. Analysis of the Chemical Diffusion Coefficient of Lithium Ions in Li3V2(PO4)3 Cathode Material. *Electrochim. Acta* **2010**, *55*, 2384–2390.

(90) Wang, J.; Zhang, X.; Liu, J.; Yang, G.; Ge, Y.; Yu, Z.; Wang, R.; Pan, X. Long-Term Cyclability and High-Rate Capability of Li3V2(PO4)3/C Cathode

Material Using PVA as Carbon Source. *Electrochim. Acta* **2010**, *55*, 6879–6884.

(91) Jiang, T.; Pan, W.; Wang, J.; Bie, X.; Du, F.; Wei, Y.; Wang, C.; Chen, G. Carbon Coated Li3V2(PO4)3 Cathode Material Prepared by a PVA Assisted Sol–gel Method. *Electrochim. Acta* **2010**, *55*, 3864–3869.

(92) Qiao, Y. Q.; Tu, J. P.; Wang, X. L.; Gu, C. D. The Low and High Temperature Electrochemical Performances of Li3V2(PO4)3/C Cathode Material for Li-Ion Batteries. *J. Power Sources* **2012**, *199*, 287–292.

(93) Qiao, Y. Q.; Wang, X. L.; Xiang, J. Y.; Zhang, D.; Liu, W. L.; Tu, J. P. Electrochemical Performance of Li3V2(PO4)3/C Cathode Materials Using Stearic Acid as a Carbon Source. *Electrochim. Acta* **2011**, *56*, 2269–2275.

(94) Zheng, J.; Li, X.; Wang, Z.; Niu, S.; Liu, D.; Wu, L.; Li, L.; Li, J.; Guo, H. Novel Synthesis of LiFePO4–Li3V2(PO4)3 Composite Cathode Material by Aqueous Precipitation and Lithiation. *J. Power Sources* **2010**, *195*, 2935–2938.

(95) Wang, L.; Tang, Z.; Ma, L.; Zhang, X. High-Rate Cathode Based on Li3V2(PO4)3/C Composite Material Prepared via a Glycine-Assisted Sol–gel Method. *Electrochem. commun.* **2011**, *13*, 1233–1235.

(96) Fey, G. T.-K.; Muralidharan, P.; Lu, C.-Z.; Cho, Y.-D. Enhanced Electrochemical Performance and Thermal Stability of La2O3-Coated LiCoO2. *Electrochim. Acta* **2006**, *51*, 4850–4858.

(97) Huang, Y.; Chen, J.; Cheng, F.; Wan, W.; Liu, W.; Zhou, H.; Zhang, X. A Modified Al2O3 Coating Process to Enhance the Electrochemical Performance of Li(Ni1/3Co1/3Mn1/3)O2 and Its Comparison with Traditional Al2O3 Coating Process. *J. Power Sources* **2010**, *195*, 8267–8274.

(98) Liu, H.; Cheng, C.; Zhang, K. The Effect of ZnO Coating on LiMn2O4 Cycle Life in High Temperature for Lithium Secondary Batteries. *Mater. Chem. Phys.* **2007**, *101*, 276–279.

(99) Ting-Kuo Fey, G.; Lu, C.-Z.; Prem Kumar, T.; Chang, Y.-C. TiO2 Coating for Long-Cycling LiCoO2: A Comparison of Coating Procedures. *Surf. Coatings Technol.* **2005**, *199*, 22–31.

(100) Chang, W.; Choi, J.-W.; Im, J.-C.; Lee, J. K. Effects of ZnO Coating on Electrochemical Performance and Thermal Stability of LiCoO2 as Cathode Material for Lithium-Ion Batteries. *J. Power Sources* **2010**, *195*, 320–326.

(101) Zhai, J.; Zhao, M.; Wang, D.; Qiao, Y. Effect of MgO Nanolayer Coated on Li3V2(PO4)3/C Cathode Material for Lithium-Ion Battery. *J. Alloys Compd.* **2010**, *502*, 401–406.

(102) Kim, J.; Yoo, J.-K.; Jung, Y. S.; Kang, K. Li3V2(PO4)3/Conducting Polymer as a High Power 4 V-Class Lithium Battery Electrode. *Adv. Energy Mater.* **2013**, *3*, 1004–1007.

(103) Morgan, D.; Ceder, G.; Saïdi, M. .; Barker, J.; Swoyer, J.; Huang, H.; Adamson, G. Experimental and Computational Study of the Structure and Electrochemical Properties of Monoclinic LixM2(PO4)3 Compounds. *J. Power Sources* **2003**, *119-121*, 755–759.

(104) Chen, Y.; Zhao, Y.; An, X.; Liu, J.; Dong, Y.; Chen, L. Preparation and Electrochemical Performance Studies on Cr-Doped Li3V2(PO4)3 as Cathode Materials for Lithium-Ion Batteries. *Electrochim. Acta* **2009**, *54*, 5844–5850.

(105) Huang, J. S.; Yang, L.; Liu, K. Y.; Tang, Y. F. Synthesis and Characterization of Li3V(2−2x/3)Mgx(PO4)3/C Cathode Material for Lithium-Ion Batteries. *J. Power Sources* **2010**, *195*, 5013–5018.

(106) Dai, C.; Chen, Z.; Jin, H.; Hu, X. Synthesis and Performance of Li3(V1−xMgx)2(PO4)3 Cathode Materials. *J. Power Sources* **2010**, *195*, 5775–5779.

(107) Kuang, Q.; Zhao, Y.; An, X.; Liu, J.; Dong, Y.; Chen, L. Synthesis and Electrochemical Properties of Co-Doped Li3V2(PO4)3 Cathode Materials for Lithium-Ion Batteries. *Electrochim. Acta* **2010**, *55*, 1575–1581.

(108) Bini, M.; Ferrari, S.; Capsoni, D.; Massarotti, V. Mn Influence on the Electrochemical Behaviour of Li3V2(PO4)3 Cathode Material. *Electrochim. Acta* **2011**, *56*, 2648–2655.

(109) Wu, W.; Liang, J.; Yan, J.; Mao, W. Synthesis of Li3NixV2−x(PO4)3/C Cathode Materials and Their Electrochemical Performance for Lithium Ion Batteries. *J. Solid State Electrochem.* **2013**, *17*, 2027–2033.

(110) Sun, C.; Rajasekhara, S.; Dong, Y.; Goodenough, J. B. Hydrothermal Synthesis and Electrochemical Properties of Li3V2(PO4)3/C-Based Composites for Lithium-Ion Batteries. *ACS Appl. Mater. Interfaces* **2011**, *3*, 3772–3776.

(111) Yao, J.; Wei, S.; Zhang, P.; Shen, C.; Aguey-Zinsou, K.-F.; Wang, L. Synthesis and Properties of Li3V2−xCex(PO4)3/C Cathode Materials for Li-Ion Batteries. *J. Alloys Compd.* **2012**, *532*, 49–54.

(112) Liu, H.; Bi, S.; Wen, G.; Teng, X.; Gao, P.; Ni, Z.; Zhu, Y.; Zhang, F. Synthesis and Electrochemical Performance of Sn-Doped Li3V2(PO4)3/C Cathode Material for Lithium Ion Battery by Microwave Solid-State Technique. *J. Alloys Compd.* **2012**, *543*, 99–104.

(113) Mateyshina, Y. G.; Uvarov, N. F. Electrochemical Behavior of Li3−xM′xV2−yM″y(PO4)3 (M′=K, M″=Sc, Mg+Ti)/C Composite Cathode Material for Lithium-Ion Batteries. *J. Power Sources* **2011**, *196*, 1494–1497.

(114) Yan, J.; Yuan, W.; Tang, Z.-Y.; Xie, H.; Mao, W.-F.; Ma, L. Synthesis and Electrochemical Performance of Li3V2(PO4)3−xClx/C Cathode Materials for Lithium-Ion Batteries. *J. Power Sources* **2012**, *209*, 251–256.

(115) Fujishima, A.; Honda, K. Electrochemical Photolysis of Water at a Semiconductor Electrode. *Nature* **1972**, *238*, 37–38.

(116) Hoffmann, M. R.; Martin, S. T.; Choi, W.; Bahnemann, D. W. Environmental Applications of Semiconductor Photocatalysis. *Chem. Rev.* **1995**, *95*, 69–96.

(117) Kudo, A.; Miseki, Y. Heterogeneous Photocatalyst Materials for Water Splitting. *Chem. Soc. Rev.* **2009**, *38*, 253–278.

(118) Chen, X.; Shen, S.; Guo, L.; Mao, S. S. Semiconductor-Based Photocatalytic Hydrogen Generation. *Chem. Rev.* **2010**, *110*, 6503–6570.

(119) Ng, Y. H.; Ikeda, S.; Matsumura, M.; Amal, R. A Perspective on Fabricating Carbon-Based Nanomaterials by Photocatalysis and Their Applications. *Energy Environ. Sci.* **2012**, *5*, 9307.

(120) Ho, W.; Yu, J. C. Sonochemical Synthesis and Visible Light Photocatalytic Behavior of CdSe and CdSe/TiO2 Nanoparticles. *J. Mol. Catal. A Chem.* **2006**, *247*, 268–274.

(121) Tae Kwon, Y.; Yong Song, K.; In Lee, W.; Jin Choi, G.; Rag Do, Y. Photocatalytic Behavior of WO3-Loaded TiO2 in an Oxidation Reaction. *J. Catal.* **2000**, *191*, 192–199.

(122) Lo, S.-C.; Lin, C.-F.; Wu, C.-H.; Hsieh, P.-H. Capability of Coupled CdSe/TiO2 for Photocatalytic Degradation of 4-Chlorophenol. *J. Hazard. Mater.* **2004**, *114*, 183–190.

(123) Xu, Q. C.; Ng, Y. H.; Zhang, Y.; Loo, J. S. C.; Amal, R.; Tan, T. T. Y. A Three-Way Synergy of Triple-Modified Bi2WO6/Ag/N-TiO2 Nanojunction Film for Enhanced Photogenerated Charges Utilization. *Chem. Commun.* **2011**, *47*, 8641–8643.

(124) Barpuzary, D.; Khan, Z.; Vinothkumar, N.; De, M.; Qureshi, M. Hierarchically Grown Urchinlike CdS@ZnO and CdS@Al2O3 Heteroarrays for Efficient Visible-Light-Driven Photocatalytic Hydrogen Generation. *J. Phys. Chem. C* **2012**, *116*, 150–156.

(125) Yu, J.; Xiang, Q.; Zhou, M. Preparation, Characterization and Visible-Light-Driven Photocatalytic Activity of Fe-Doped Titania Nanorods and First-Principles Study for Electronic Structures. *Appl. Catal. B Environ.* **2009**, *90*, 595–602.

(126) Park, J. H.; Kim, S.; Bard, A. J. Novel Carbon-Doped TiO2 Nanotube Arrays with High Aspect Ratios for Efficient Solar Water Splitting. *Nano Lett.* **2006**, *6*, 24–28.

(127) Xiang, Q.; Yu, J.; Wang, W.; Jaroniec, M. Nitrogen Self-Doped Nanosized TiO2 Sheets with Exposed {001} Facets for Enhanced Visible-Light Photocatalytic Activity. *Chem. Commun.* **2011**, *47*, 6906–6908.

(128) Xiang, Q.; Yu, J.; Cheng, B.; Ong, H. C. Microwave-Hydrothermal Preparation and Visible-Light Photoactivity of Plasmonic Photocatalyst Ag-TiO2 Nanocomposite Hollow Spheres. *Chem. Asian J.* **2010**, *5*, 1466–1474.

(129) Yu, J.; Xiong, J.; Cheng, B.; Liu, S. Fabrication and Characterization of Ag–TiO2 Multiphase Nanocomposite Thin Films with Enhanced Photocatalytic Activity. *Appl. Catal. B Environ.* **2005**, *60*, 211–221.

(130) Yu, J.; Qi, L.; Jaroniec, M. Hydrogen Production by Photocatalytic Water Splitting over Pt/TiO2 Nanosheets with Exposed (001) Facets. *J. Phys. Chem. C* **2010**, *114*, 13118–13125.

(131) Lakadamyali, F.; Reisner, E. Photocatalytic H2 Evolution from Neutral Water with a Molecular Cobalt Catalyst on a Dye-Sensitised TiO2 Nanoparticle. *Chem. Commun.* **2011**, *47*, 1695–1697.

(132) GURUNATHAN, K. Photocatalytic Hydrogen Production by Dye-Sensitized Pt/SnO2 and Pt/SnO2/RuO2 in Aqueous Methyl Viologen Solution. *Int. J. Hydrogen Energy* **1997**, *22*, 57–62.

(133) Füldner, S.; Mild, R.; Siegmund, H. I.; Schroeder, J. A.; Gruber, M.; König, B. Green-Light Photocatalytic Reduction Using Dye-Sensitized TiO2 and Transition Metal Nanoparticles. *Green Chem.* **2010**, *12*, 400.

(134) Zhang, M.; Chen, C.; Ma, W.; Zhao, J. Visible-Light-Induced Aerobic Oxidation of Alcohols in a Coupled Photocatalytic System of Dye-Sensitized TiO2 and TEMPO. *Angew. Chemie* **2008**, *47*, 9730–9733.

(135) Xia, X.-H.; Jia, Z.-J.; Yu, Y.; Liang, Y.; Wang, Z.; Ma, L.-L. Preparation of Multi-Walled Carbon Nanotube Supported TiO2 and Its Photocatalytic Activity in the Reduction of CO2 with H2O. *Carbon N. Y.* **2007**, *45*, 717–721.

(136) Zhang, H.; Lv, X.; Li, Y.; Wang, Y.; Li, J. P25-Graphene Composite as a High Performance Photocatalyst. *ACS Nano* **2010**, *4*, 380–386.

(137) Kim, S.; Lim, S. K. Preparation of TiO2-Embedded Carbon Nanofibers and Their Photocatalytic Activity in the Oxidation of Gaseous Acetaldehyde. *Appl. Catal. B Environ.* **2008**, *84*, 16–20.

(138) Dey, N. K.; Kim, M. J.; Kim, K.-D.; Seo, H. O.; Kim, D.; Kim, Y. D.; Lim, D. C.; Lee, K. H. Adsorption and Photocatalytic Degradation of Methylene Blue over TiO2 Films on Carbon Fiber Prepared by Atomic Layer Deposition. *J. Mol. Catal. A Chem.* **2011**, *337*, 33–38.

(139) Peralta-Hernández, J. M.; Manríquez, J.; Meas-Vong, Y.; Rodríguez, F. J.; Chapman, T. W.; Maldonado, M. I.; Godínez, L. A. Photocatalytic Properties of Nano-Structured TiO2-Carbon Films Obtained by Means of Electrophoretic Deposition. *J. Hazard. Mater.* **2007**, *147*, 588–593.

(140) Mu, J.; Shao, C.; Guo, Z.; Zhang, Z.; Zhang, M.; Zhang, P.; Chen, B.; Liu, Y. High Photocatalytic Activity of ZnO-Carbon Nanofiber Heteroarchitectures. *ACS Appl. Mater. Interfaces* **2011**, *3*, 590–596.

(141) Robel, I.; Bunker, B. A.; Kamat, P. V. Single-Walled Carbon Nanotube-CdS Nanocomposites as Light-Harvesting Assemblies: Photoinduced Charge-Transfer Interactions. *Adv. Mater.* **2005**, *17*, 2458–2463.

(142) Torimoto, T.; Ito, S.; Kuwabata, S.; Yoneyama, H. Effects of Adsorbents Used as Supports for Titanium Dioxide Loading on Photocatalytic Degradation of Propyzamide. *Environ. Sci. Technol.* **1996**, *30*, 1275–1281.

(143) Wang, W.; Serp, P.; Kalck, P.; Faria, J. L. Visible Light Photodegradation of Phenol on MWNT-TiO2 Composite Catalysts Prepared by a Modified Sol–gel Method. *J. Mol. Catal. A Chem.* **2005**, *235*, 194–199.

(144) Mai, L.; Huang, C.; Wang, D.; Zhang, Z.; Wang, Y. Effect of C Doping on the Structural and Optical Properties of Sol–gel TiO2 Thin Films. *Appl. Surf. Sci.* **2009**, *255*, 9285–9289.

(145) Zhang, L.-W.; Fu, H.-B.; Zhu, Y.-F. Efficient TiO 2 Photocatalysts from Surface Hybridization of TiO2 Particles with Graphite-like Carbon. *Adv. Funct. Mater.* **2008**, *18*, 2180–2189.

(146) Williams, G.; Seger, B.; Kamat, P. V. TiO2-Graphene Nanocomposites. UV-Assisted Photocatalytic Reduction of Graphene Oxide. *ACS Nano* **2008**, *2*, 1487–1491.

(147) Lightcap, I. V; Kosel, T. H.; Kamat, P. V. Anchoring Semiconductor and Metal Nanoparticles on a Two-Dimensional Catalyst Mat. Storing and Shuttling Electrons with Reduced Graphene Oxide. *Nano Lett.* **2010**, *10*, 577–583.

(148) Ge, S.; Jia, H.; Zhao, H.; Zheng, Z.; Zhang, L. First Observation of Visible Light Photocatalytic Activity of Carbon Modified Nb2O5 Nanostructures. *J. Mater. Chem.* **2010**, *20*, 3052.

(149) Prado, A. G. S.; Bolzon, L. B.; Pedroso, C. P.; Moura, A. O.; Costa, L. L. Nb2O5 as Efficient and Recyclable Photocatalyst for Indigo Carmine Degradation. *Appl. Catal. B Environ.* **2008**, *82*, 219–224.

(150) Torres, J. D.; Faria, E. A.; SouzaDe, J. R.; Prado, A. G. S. Preparation of Photoactive Chitosan–niobium (V) Oxide Composites for Dye Degradation. *J. Photochem. Photobiol. A Chem.* **2006**, *182*, 202–206.

(151) Esteves, A.; Oliveira, L. C. A.; Ramalho, T. C.; Goncalves, M.; Anastacio, A. S.; Carvalho, H. W. P. New Materials Based on Modified Synthetic Nb2O5 as Photocatalyst for Oxidation of Organic Contaminants. *Catal. Commun.* **2008**, *10*, 330–332.

(152) Lin, H.-Y.; Huang, H.-C.; Wang, W.-L. Preparation of Mesoporous In–Nb Mixed Oxides and Its Application in Photocatalytic Water Splitting for Hydrogen Production. *Microporous Mesoporous Mater.* **2008**, *115*, 568–575.

(153) Xing, J.; Shan, Z.; Li, K.; Bian, J.; Lin, X.; Wang, W.; Huang, F. Photocatalytic Activity of Nb2O5/SrNb2O6 Heterojunction on the Degradation of Methyl Orange. *J. Phys. Chem. Solids* **2008**, *69*, 23–28.

(154) Li, X.; Kikugawa, N.; Ye, J. Nitrogen-Doped Lamellar Niobic Acid with Visible Light-Responsive Photocatalytic Activity. *Adv. Mater.* **2008**, *20*, 3816–3819.

(155) Ullah, R.; Sun, H.; Ang, H. M.; Tadé, M. O.; Wang, S. Comparative Investigation of Photocatalytic Degradation of Toluene on Nitrogen Doped Ta2O5 and Nb2O5 Nanoparticles. *Ind. Eng. Chem. Res.* **2013**, *52*, 3320–3328.

(156) Lin, H.-Y.; Yang, H.-C.; Wang, W.-L. Synthesis of Mesoporous Nb2O5 Photocatalysts with Pt, Au, Cu and NiO Cocatalyst for Water Splitting. *Catal. Today* **2011**, *174*, 106–113.

(157) Wang, R.; Zhu, Y.; Qiu, Y.; Leung, C.-F.; He, J.; Liu, G.; Lau, T.-C. Synthesis of Nitrogen-Doped KNbO3 Nanocubes with High Photocatalytic Activity for Water Splitting and Degradation of Organic Pollutants under Visible Light. *Chem. Eng. J.* **2013**, *226*, 123–130.

(158) Asahi, R.; Morikawa, T.; Ohwaki, T.; Aoki, K.; Taga, Y. Visible-Light Photocatalysis in Nitrogen-Doped Titanium Oxides. *Science* **2001**, *293*, 269–271.

(159) Matsui, H.; Kira, K.; Karuppuchamy, S.; Yoshihara, M. The Electronic Behaviors of Visible Light Sensitive Nb2O5/Cr2O3/carbon Clusters Composite Materials. *Curr. Appl. Phys.* **2009**, *9*, 592–597.

(160) Stach, E. Real-Time Observations with Electron Microscopy. *Mater. Today* **2008**, *11*, 50–58.

(161) Helveg, S.; López-Cartes, C.; Sehested, J.; Hansen, P. L.; Clausen, B. S.; Rostrup-Nielsen, J. R.; Abild-Pedersen, F.; Nørskov, J. K. Atomic-Scale Imaging of Carbon Nanofibre Growth. *Nature* **2004**, *427*, 426–429.

(162) Lin, M.; Ying Tan, J. P.; Boothroyd, C.; Loh, K. P.; Tok, E. S.; Foo, Y.-L. Direct Observation of Single-Walled Carbon Nanotube Growth at the Atomistic Scale. *Nano Lett.* **2006**, *6*, 449–452.

(163) Hofmann, S.; Sharma, R.; Ducati, C.; Du, G.; Mattevi, C.; Cepek, C.; Cantoro, M.; Pisana, S.; Parvez, A.; Cervantes-Sodi, F.; *et al.* In Situ Observations of Catalyst Dynamics during Surface-Bound Carbon Nanotube Nucleation. *Nano Lett.* **2007**, *7*, 602–608.

(164) Rodríguez-Manzo, J. A.; Terrones, M.; Terrones, H.; Kroto, H. W.; Sun, L.; Banhart, F. In Situ Nucleation of Carbon Nanotubes by the Injection of Carbon Atoms into Metal Particles. *Nat. Nanotechnol.* **2007**, *2*, 307–311.

(165) Yoshida, H.; Takeda, S.; Uchiyama, T.; Kohno, H.; Homma, Y. Atomic-Scale in-Situ Observation of Carbon Nanotube Growth from Solid State Iron Carbide Nanoparticles. *Nano Lett.* **2008**, *8*, 2082–2086.

(166) Meyer, J. C.; Girit, C. O.; Crommie, M. F.; Zettl, A. Imaging and Dynamics of Light Atoms and Molecules on Graphene. *Nature* **2008**, *454*, 319–322.

(167) Peng, Z.; Somodi, F.; Helveg, S.; Kisielowski, C.; Specht, P.; Bell, A. T. High-Resolution in Situ and Ex Situ TEM Studies on Graphene Formation and Growth on Pt Nanoparticles. *J. Catal.* **2012**, *286*, 22–29.

(168) Rosmi, M. S.; Yusop, M. Z.; Kalita, G.; Yaakob, Y.; Takahashi, C.; Tanemura, M. Visualizing Copper Assisted Graphene Growth in Nanoscale. *Sci. Rep.* **2014**, *4*, 7563.

(169) Page, A. J.; Ohta, Y.; Irle, S.; Morokuma, K. Mechanisms of Single-Walled Carbon Nanotube Nucleation, Growth, and Healing Determined Using QM/MD Methods. *Acc. Chem. Res.* **2010**, *43*, 1375–1385.

(170) Wu, X.-L.; Jiang, L.-Y.; Cao, F.-F.; Guo, Y.-G.; Wan, L.-J. LiFePO4 Nanoparticles Embedded in a Nanoporous Carbon Matrix: Superior Cathode Material for Electrochemical Energy-Storage Devices. *Adv. Mater.* **2009**, *21*, 2710–2714.

(171) Liu, Y.; Chen, B.; Cao, F.; Zhao, X.; Yuan, J. Synthesis of Nanoarchitectured LiNi0.5Mn0.5O2 Spheres for High-Performance Rechargeable Lithium-Ion Batteries via an in Situ Conversion Route. *J. Mater. Chem.* **2011**, *21*, 10437–10441.

(172) Lee, H.-W.; Muralidharan, P.; Ruffo, R.; Mari, C. M.; Cui, Y.; Kim, D. K. Ultrathin Spinel LiMn2O4 Nanowires as High Power Cathode Materials for Li-Ion Batteries. *Nano Lett.* **2010**, *10*, 3852–3856.

(173) Han, J.-T.; Goodenough, J. B. 3-V Full Cell Performance of Anode Framework TiNb2O7 /Spinel LiNi0.5Mn1.5O4. *Chem. Mater.* **2011**, *23*, 3404–3407.

(174) Pan, A.; Liu, J.; Zhang, J.-G.; Xu, W.; Cao, G.; Nie, Z.; Arey, B. W.; Liang, S. Nano-Structured Li3V2(PO4)3/carbon Composite for High-Rate Lithium-Ion Batteries. *Electrochem. Commun.* **2010**, *12*, 1674–1677.

(175) Yin, S.-C.; Grondey, H.; Strobel, P.; Anne, M.; Nazar, L. F. Electrochemical Property: Structure Relationships in Monoclinic Li(3-y)V2(PO4)3. *J. Am. Chem. Soc.* **2003**, *125*, 10402–10411.

(176) Huang, H.; Yin, S.-C.; Kerr, T.; Taylor, N.; Nazar, L. F. Nanostructured Composites: A High Capacity, Fast Rate Li3V2(PO4)3/Carbon Cathode for Rechargeable Lithium Batteries. *Adv. Mater.* **2002**, *14*, 1525–1528.

(177) Zhang, X.; Guo, H.; Li, X.; Wang, Z.; Wu, L. High Tap-Density Li3V2(PO4)3/C Composite Material Synthesized by Sol Spray-Drying and Post-Calcining Method. *Electrochim. Acta* **2012**, *64*, 65–70.

(178) Du, X.; He, W.; Zhang, X.; Yue, Y.; Liu, H.; Zhang, X.; Min, D.; Ge, X.; Du, Y. Enhancing the Electrochemical Performance of Lithium Ion Batteries

Using Mesoporous Li3V2(PO4)3/C Microspheres. *J. Mater. Chem.* **2012**, *22*, 5960–5969.

(179) Cho, A. R.; Son, J. N.; Aravindan, V.; Kim, H.; Kang, K. S.; Yoon, W. S.; Kim, W. S.; Lee, Y. S. Carbon Supported, Al Doped-Li3V2(PO4)3 as a High Rate Cathode Material for Lithium-Ion Batteries. *J. Mater. Chem.* **2012**, *22*, 6556–6560.

(180) Liu, H.; Gao, P.; Fang, J.; Yang, G. Li3V2(PO4)3/graphene Nanocomposites as Cathode Material for Lithium Ion Batteries. *Chem. Commun.* **2011**, *47*, 9110–9112.

(181) Wang, C.; Liu, H.; Yang, W. An Integrated Core–shell Structured Li3V2(PO4)3@C Cathode Material of LIBs Prepared by a Momentary Freeze-Drying Method. *J. Mater. Chem.* **2012**, *22*, 5281–5285.

(182) Sun, C.; Rajasekhara, S.; Dong, Y.; Goodenough, J. B. Hydrothermal Synthesis and Electrochemical Properties of Li3V2(PO4)3/C-Based Composites for Lithium-Ion Batteries. *ACS Appl. Mater. Interfaces* **2011**, *3*, 3772–3776.

(183) Deng, C.; Zhang, S.; Yang, S. Y.; Gao, Y.; Wu, B.; Ma, L.; Fu, B. L.; Wu, Q.; Liu, F. L. Effects of Ti and Mg Codoping on the Electrochemical Performance of Li3V2(PO4)3 Cathode Material for Lithium Ion Batteries. *J. Phys. Chem. C* **2011**, *115*, 15048–15056.

(184) Chen, Y.; Zhao, Y.; An, X.; Liu, J.; Dong, Y.; Chen, L. Preparation and Electrochemical Performance Studies on Cr-Doped Li3V2(PO4)3 as Cathode Materials for Lithium-Ion Batteries. *Electrochim. Acta* **2009**, *54*, 5844–5850.

(185) Morgan, D.; Ceder, G.; Saïdi, M. .; Barker, J.; Swoyer, J.; Huang, H.; Adamson, G. Experimental and Computational Study of the Structure and Electrochemical Properties of Monoclinic LixM2(PO4)3 Compounds. *J. Power Sources* **2003**, *119-121*, 755–759.

(186) Ren, M. M.; Zhou, Z.; Gao, X. P.; Peng, W. X.; Wei, J. P. Core-Shell Li3V2(PO4)3@C Composites as Cathode Materials for Lithium-Ion Batteries. *J. Phys. Chem. C* **2008**, *112*, 5689–5693.

(187) Qiao, Y. Q.; Wang, X. L.; Zhou, Y.; Xiang, J. Y.; Zhang, D.; Shi, S. J.; Tu, J. P. Electrochemical Performance of Carbon-Coated Li3V2(PO4)3 Cathode Materials Derived from Polystyrene-Based Carbon-Thermal Reduction Synthesis. *Electrochim. Acta* **2010**, *56*, 510–516.

(188) Chang, C.; Xiang, J.; Shi, X.; Han, X.; Yuan, L.; Sun, J. Hydrothermal Synthesis of Carbon-Coated Lithium Vanadium Phosphate. *Electrochim. Acta* **2008**, *54*, 623–627.

(189) Rui, X. H.; Jin, Y.; Feng, X. Y.; Zhang, L. C.; Chen, C. H. A Comparative Study on the Low-Temperature Performance of LiFePO4/C and Li3V2(PO4)3/C Cathodes for Lithium-Ion Batteries. *J. Power Sources* **2011**, *196*, 2109–2114.

(190) Fu, P.; Zhao, Y.; Dong, Y.; Hou, X. Synthesis of High Tap Density Li3V2(PO4)3 Cathode Materials Using Mixed Lithium Precursors. *J. Phys. Chem. Solids* **2010**, *71*, 394–399.

(191) Chen, Z.; Dahn, J. R. Reducing Carbon in LiFePO4/C Composite Electrodes to Maximize Specific Energy, Volumetric Energy, and Tap Density. *J. Electrochem. Soc.* **2002**, *149*, A1184–A1189.

(192) Wang, M.; Yang, Y.; Zhang, Y. Synthesis of Micro-Nano Hierarchical Structured LiFePO4/C Composite with Both Superior High-Rate Performance and High Tap Density. *Nanoscale* **2011**, *3*, 4434–4439.

(193) Ferrari, A.; Robertson, J. Interpretation of Raman Spectra of Disordered and Amorphous Carbon. *Phys. Rev. B* **2000**, *61*, 14095–14107.

(194) Chen, J.; Whittingham, M. Hydrothermal Synthesis of Lithium Iron Phosphate. *Electrochem. commun.* **2006**, *8*, 855–858.

(195) Sun, Y.-K.; Oh, S.-M.; Park, H.-K.; Scrosati, B. Micrometer-Sized, Nanoporous, High-Volumetric-Capacity LiMn0.85Fe0.15PO4 Cathode Material for Rechargeable Lithium-Ion Batteries. *Adv. Mater.* **2011**, *23*, 5050–5054.

(196) Xu, R.; Pang, W.; Yu, J.; Huo, Q.; Chen, J. *Chemistry of Zeolites and Related Porous Materials*; John Wiley & Sons, Ltd: Chichester, UK, 2007.

(197) Liu, H.; Yang, G.; Zhang, X.; Gao, P.; Wang, L.; Fang, J.; Pinto, J.; Jiang, X. Kinetics of Conventional Carbon Coated-Li3V2(PO4)3 and Nanocomposite Li3V2(PO4)3/graphene as Cathode Materials for Lithium Ion Batteries. *J. Mater. Chem.* **2012**, *22*, 11039–11047.

(198) Fei, L.; Lu, W.; Sun, L.; Wang, J.; Wei, J.; Chan, H. L. W.; Wang, Y. Highly Entangled Carbon Nanoflakes on Li3V2(PO4)3 Microrods for Improved Lithium Storage Performance. *RSC Adv.* **2013**, *3*, 1297.

(199) Ravet, N.; Chouinard, Y.; Magnan, J. F.; Besner, S.; Gauthier, M.; Armand, M. Electroactivity of Natural and Synthetic Triphylite. *J. Power Sources* **2001**, *97-98*, 503–507.

(200) Chen, Q.; Zhang, T.; Qiao, X.; Li, D.; Yang, J. Li3V2(PO4)3/C Nanofibers Composite as a High Performance Cathode Material for Lithium-Ion Battery. *J. Power Sources* **2013**, *234*, 197–200.

(201) Duan, W.; Hu, Z.; Zhang, K.; Cheng, F.; Tao, Z.; Chen, J. Li3V2(PO4)3@C Core-Shell Nanocomposite as a Superior Cathode Material for Lithium-Ion Batteries. *Nanoscale* **2013**, *5*, 6485–6490.

(202) Mai, L.; Li, S.; Dong, Y.; Zhao, Y.; Luo, Y.; Xu, H. Long-Life and High-Rate Li3V2(PO4)3/C Nanosphere Cathode Materials with Three-Dimensional Continuous Electron Pathways. *Nanoscale* **2013**, *5*, 4864–4869.

(203) Zhang, L.-L.; Liang, G.; Peng, G.; Zou, F.; Huang, Y.-H.; Croft, M. C.; Ignatov, A. Significantly Improved Electrochemical Performance in

Li3V2(PO4)3/C Promoted by SiO2 Coating for Lithium-Ion Batteries. *J. Phys. Chem. C* **2012**, *116*, 12401–12408.

(204) Fei, L.; Yuan, J.; Hu, Y.; Wu, C.; Wang, J.; Wang, Y. Visible Light Responsive Perovskite BiFeO3 Pills and Rods with Dominant {111}c Facets. *Cryst. Growth Des.* **2011**, *11*, 1049–1053.

(205) Barker, J.; Gover, R. K. B.; Burns, P.; Bryan, A. The Effect of Al Substitution on the Electrochemical Insertion Properties of the Lithium Vanadium Phosphate, Li3V2(PO4)3. *J. Electrochem. Soc.* **2007**, *154*, A307–A313.

(206) Muraliganth, T.; Vadivel Murugan, A.; Manthiram, A. Facile Synthesis of Carbon-Decorated Single-Crystalline Fe3O4 Nanowires and Their Application as High Performance Anode in Lithium Ion Batteries. *Chem. Commun.* **2009**, 7360–7362.

(207) Wu, C. Z.; Xie, Y.; Lei, L. Y.; Hu, S. Q.; OuYang, C. Z. Synthesis of New-Phased VOOH Hollow “Dandelions” and Their Application in Lithium-Ion Batteries. *Adv. Mater.* **2006**, *18*, 1727–1732.

(208) Sawatzky, G.; Post, D. X-Ray Photoelectron and Auger Spectroscopy Study of Some Vanadium Oxides. *Phys. Rev. B* **1979**, *20*, 1546–1555.

(209) Yoneyama, H.; Yamashita, Y.; Tamura, H. Heterogeneous Photocatalytic Reduction of Dichromate on N-Type Semiconductor Catalysts. *Nature* **1979**, *282*, 817–818.

(210) Chen, X.; Mao, S. S. Titanium Dioxide Nanomaterials: Synthesis, Properties, Modifications, and Applications. *Chem. Rev.* **2007**, *107*, 2891–2959.

(211) Linsebigler, A. L.; Lu, G.; Yates, J. T. Photocatalysis on TiO2 Surfaces: Principles, Mechanisms, and Selected Results. *Chem. Rev.* **1995**, *95*, 735–758.

(212) Xu, X.; Yang, G.; Liang, J.; Ding, S.; Tang, C.; Yang, H.; Yan, W.; Yang, G.; Yu, D. Fabrication of One-Dimensional Heterostructured TiO2@SnO2 with Enhanced Photocatalytic Activity. *J. Mater. Chem. A* **2014**, *2*, 116.

(213) Sakthivel, S.; Kisch, H. Daylight Photocatalysis by Carbon-Modified Titanium Dioxide. *Angew. Chemie* **2003**, *42*, 4908–4911.

(214) Zhang, L.; Jing, D.; She, X.; Liu, H.; Yang, D.; Lu, Y.; Li, J.; Zheng, Z.; Guo, L. Heterojunctions in G-C3N4/TiO2(B) Nanofibres with Exposed (001) Plane and Enhanced Visible-Light Photoactivity. *J. Mater. Chem. A* **2014**, *2*, 2071.

(215) Zhang, Y.; Fei, L.; Jiang, X.; Pan, C.; Wang, Y. Engineering Nanostructured Bi2WO6-TiO2 Toward Effective Utilization of Natural Light in Photocatalysis. *J. Am. Ceram. Soc.* **2011**, *94*, 4157–4161.

(216) Zhao, L.; Chen, X.; Wang, X.; Zhang, Y.; Wei, W.; Sun, Y.; Antonietti, M.; Titirici, M.-M. One-Step Solvothermal Synthesis of a Carbon@TiO2 Dyade Structure Effectively Promoting Visible-Light Photocatalysis. *Adv. Mater.* **2010**, *22*, 3317–3321.

(217) An, X.; Yu, J. C.; Wang, Y.; Hu, Y.; Yu, X.; Zhang, G. WO3 Nanorods/graphene Nanocomposites for High-Efficiency Visible-Light-Driven Photocatalysis and NO2 Gas Sensing. *J. Mater. Chem.* **2012**, *22*, 8525.

(218) Li, H.; Liu, R.; Liu, Y.; Huang, H.; Yu, H.; Ming, H.; Lian, S.; Lee, S.-T.; Kang, Z. Carbon Quantum dots/Cu2O Composites with Protruding Nanostructures and Their Highly Efficient (near) Infrared Photocatalytic Behavior. *J. Mater. Chem.* **2012**, *22*, 17470.

(219) Li, H.; He, X.; Kang, Z.; Huang, H.; Liu, Y.; Liu, J.; Lian, S.; Tsang, C. H. A.; Yang, X.; Lee, S.-T. Water-Soluble Fluorescent Carbon Quantum Dots and Photocatalyst Design. *Angew. Chemie* **2010**, *49*, 4430–4434.

(220) Ming, H.; Ma, Z.; Liu, Y.; Pan, K.; Yu, H.; Wang, F.; Kang, Z. Large Scale Electrochemical Synthesis of High Quality Carbon Nanodots and Their Photocatalytic Property. *Dalt. Trans.* **2012**, *41*, 9526–9531.

(221) Zhang, H.; Huang, H.; Ming, H.; Li, H.; Zhang, L.; Liu, Y.; Kang, Z. Carbon Quantum dots/Ag3PO4 Complex Photocatalysts with Enhanced

Photocatalytic Activity and Stability under Visible Light. *J. Mater. Chem.* **2012**, *22*, 10501.

(222) Zhang, N.; Zhang, Y.; Xu, Y.-J. Recent Progress on Graphene-Based Photocatalysts: Current Status and Future Perspectives. *Nanoscale* **2012**, *4*, 5792–5813.

(223) Han, L.; Wang, P.; Dong, S. Progress in Graphene-Based Photoactive Nanocomposites as a Promising Class of Photocatalyst. *Nanoscale* **2012**, *4*, 5814–5825.

(224) Zhang, P.; Shao, C.; Zhang, Z.; Zhang, M.; Mu, J.; Guo, Z.; Liu, Y. TiO2@carbon Core/shell Nanofibers: Controllable Preparation and Enhanced Visible Photocatalytic Properties. *Nanoscale* **2011**, *3*, 2943–2949.

(225) Zhang, P.; Shao, C.; Zhang, Z.; Zhang, M.; Mu, J.; Guo, Z.; Sun, Y.; Liu, Y. Core/shell Nanofibers of TiO2@carbon Embedded by Ag Nanoparticles with Enhanced Visible Photocatalytic Activity. *J. Mater. Chem.* **2011**, *21*, 17746.

(226) CARNITI, P.; GERVASINI, A.; BIELLA, S.; AUROUX, A. Niobic Acid and Niobium Phosphate as Highly Acidic Viable Catalysts in Aqueous Medium: Fructose Dehydration Reaction. *Catal. Today* **2006**, *118*, 373–378.

(227) Chen, X.; Yu, T.; Fan, X.; Zhang, H.; Li, Z.; Ye, J.; Zou, Z. Enhanced Activity of Mesoporous Nb2O5 for Photocatalytic Hydrogen Production. *Appl. Surf. Sci.* **2007**, *253*, 8500–8506.

(228) Kominami, H.; Oki, K.; Kohno, M.; Onoue, S.; Kera, Y.; Ohtani, B. Novel Solvothermal Synthesis of Niobium(v) Oxide Powders and Their Photocatalytic Activity in Aqueous Suspensions. *J. Mater. Chem.* **2001**, *11*, 604–609.

(229) Ohuchi, T.; Miyatake, T.; Hitomi, Y.; Tanaka, T. Liquid Phase Photooxidation of Alcohol over Niobium Oxide without Solvents. *Catal. Today* **2007**, *120*, 233–239.

(230) Liu, Z.; Sun, D. D.; Guo, P.; Leckie, J. O. An Efficient Bicomponent TiO2/SnO2 Nanofiber Photocatalyst Fabricated by Electrospinning with a Side-by-Side Dual Spinneret Method. *Nano Lett.* **2007**, *7*, 1081–1085.

(231) Zhan, S.; Chen, D.; Jiao, X.; Tao, C. Long TiO2 Hollow Fibers with Mesoporous Walls: Sol-Gel Combined Electrospun Fabrication and Photocatalytic Properties. *J. Phys. Chem. B* **2006**, *110*, 11199–11204.

(232) Greiner, A.; Wendorff, J. H. Electrospinning: A Fascinating Method for the Preparation of Ultrathin Fibers. *Angew. Chemie* **2007**, *46*, 5670–5703.

(233) Li, D.; Xia, Y. Electrospinning of Nanofibers: Reinventing the Wheel? *Adv. Mater.* **2004**, *16*, 1151–1170.

(234) Berger, C.; Song, Z.; Li, X.; Wu, X.; Brown, N.; Naud, C.; Mayou, D.; Li, T.; Hass, J.; Marchenkov, A. N.; *et al.* Electronic Confinement and Coherence in Patterned Epitaxial Graphene. *Science* **2006**, *312*, 1191–1196.

(235) Stankovich, S.; Dikin, D. A.; Dommett, G. H. B.; Kohlhaas, K. M.; Zimney, E. J.; Stach, E. A.; Piner, R. D.; Nguyen, S. T.; Ruoff, R. S. Graphene-Based Composite Materials. *Nature* **2006**, *442*, 282–286.

(236) Qi, S.; Zuo, R.; Liu, Y.; Wang, Y. Synthesis and Photocatalytic Activity of Electrospun Niobium Oxide Nanofibers. *Mater. Res. Bull.* **2013**, *48*, 1213–1217.

(237) Guo, Y.; Wang, H.; He, C.; Qiu, L.; Cao, X. Uniform Carbon-Coated ZnO Nanorods: Microwave-Assisted Preparation, Cytotoxicity, and Photocatalytic Activity. *Langmuir* **2009**, *25*, 4678–4684.

(238) Zhang, P.; Shao, C.; Zhang, Z.; Zhang, M.; Mu, J.; Guo, Z.; Liu, Y. TiO2@carbon Core/shell Nanofibers: Controllable Preparation and Enhanced Visible Photocatalytic Properties. *Nanoscale* **2011**, *3*, 2943–2949.

(239) Han, M.; Özyilmaz, B.; Zhang, Y.; Kim, P. Energy Band-Gap Engineering of Graphene Nanoribbons. *Phys. Rev. Lett.* **2007**, *98*, 206805.

(240) Son, Y.-W.; Cohen, M. L.; Louie, S. G. Energy Gaps in Graphene Nanoribbons. *Phys. Rev. Lett.* **2006**, *97*, 216803.

(241) An, X.; Yu, X.; Yu, J. C.; Zhang, G. CdS Nanorods/reduced Graphene Oxide Nanocomposites for Photocatalysis and Electrochemical Sensing. *J. Mater. Chem. A* **2013**, *1*, 5158.

(242) Zhang, N.; Zhang, Y.; Pan, X.; Fu, X.; Liu, S.; Xu, Y.-J. Assembly of CdS Nanoparticles on the Two-Dimensional Graphene Scaffold as Visible-Light-Driven Photocatalyst for Selective Organic Transformation under Ambient Conditions. *J. Phys. Chem. C* **2011**, *115*, 23501–23511.

(243) An, S.; Joshi, B. N.; Lee, M. W.; Kim, N. Y.; Yoon, S. S. Electrospun Graphene-ZnO Nanofiber Mats for Photocatalysis Applications. *Appl. Surf. Sci.* **2014**, *294*, 24–28.

(244) Xu, T.; Zhang, L.; Cheng, H.; Zhu, Y. Significantly Enhanced Photocatalytic Performance of ZnO via Graphene Hybridization and the Mechanism Study. *Appl. Catal. B Environ.* **2011**, *101*, 382–387.

(245) Li, B.; Cao, H. ZnO@graphene Composite with Enhanced Performance for the Removal of Dye from Water. *J. Mater. Chem.* **2011**, *21*, 3346.

(246) Chen, C.; Cai, W.; Long, M.; Zhou, B.; Wu, Y.; Wu, D.; Feng, Y. Synthesis of Visible-Light Responsive Graphene oxide/TiO2 Composites with P/n Heterojunction. *ACS Nano* **2010**, *4*, 6425–6432.

(247) Zhao, D.; Sheng, G.; Chen, C.; Wang, X. Enhanced Photocatalytic Degradation of Methylene Blue under Visible Irradiation on graphene@TiO2 Dyade Structure. *Appl. Catal. B Environ.* **2012**, *111-112*, 303–308.

(248) Zhou, K.; Zhu, Y.; Yang, X.; Jiang, X.; Li, C. Preparation of graphene–TiO2 Composites with Enhanced Photocatalytic Activity. *New J. Chem.* **2011**, *35*, 353.

(249) Zhang, J.; Zhu, Z.; Tang, Y.; Feng, X. Graphene Encapsulated Hollow TiO2 Nanospheres: Efficient Synthesis and Enhanced Photocatalytic Activity. *J. Mater. Chem. A* **2013**, *1*, 3752.

(250) Hou, J.; Jiao, S.; Zhu, H.; Kumar, R. V. Carbon-Modified Bismuth Titanate Nanorods with Enhanced Visible-Light-Driven Photocatalytic Property. *CrystEngComm* **2011**, *13*, 4735.

(251) Zhuang, S.; Xu, X.; Feng, B.; Hu, J.; Pang, Y.; Zhou, G.; Tong, L.; Zhou, Y. Photogenerated Carriers Transfer in Dye-Graphene-SnO2 Composites for Highly Efficient Visible-Light Photocatalysis. *ACS Appl. Mater. Interfaces* **2014**, *6*, 613–621.

(252) Zhang, P.; Shao, C.; Zhang, M.; Guo, Z.; Mu, J.; Zhang, Z.; Zhang, X.; Liang, P.; Liu, Y. Controllable Synthesis of Zn2TiO4@carbon Core/shell Nanofibers with High Photocatalytic Performance. *J. Hazard. Mater.* **2012**, *229-230*, 265–272.

(253) Dai, Y.; Sun, Y.; Yao, J.; Ling, D.; Wang, Y.; Long, H.; Wang, X.; Lin, B.; Zeng, T. H.; Sun, Y. Graphene-Wrapped TiO2 Nanofibers with Effective Interfacial Coupling as Ultrafast Electron Transfer Bridges in Novel Photoanodes. *J. Mater. Chem. A* **2014**, *2*, 1060.

(254) Golberg, D.; Costa, P. M. F. J.; Wang, M.-S.; Wei, X.; Tang, D.-M.; Xu, Z.; Huang, Y.; Gautam, U. K.; Liu, B.; Zeng, H.; *et al.* Nanomaterial Engineering and Property Studies in a Transmission Electron Microscope. *Adv. Mater.* **2012**, *24*, 177–194.

(255) Zewail, A. H. Four-Dimensional Electron Microscopy. *Science* **2010**, *328*, 187–193.

(256) Radmilovic, V.; Ophus, C.; Marquis, E. A.; Rossell, M. D.; Tolley, A.; Gautam, A.; Asta, M.; Dahmen, U. Highly Monodisperse Core-Shell Particles Created by Solid-State Reactions. *Nat. Mater.* **2011**, *10*, 710–715.

(257) Wen, C.-Y.; Reuter, M. C.; Bruley, J.; Tersoff, J.; Kodambaka, S.; Stach, E. A.; Ross, F. M. Formation of Compositionally Abrupt Axial Heterojunctions in Silicon-Germanium Nanowires. *Science* **2009**, *326*, 1247–1250.

(258) Hansen, P. L.; Wagner, J. B.; Helveg, S.; Rostrup-Nielsen, J. R.; Clausen, B. S.; Topsøe, H. Atom-Resolved Imaging of Dynamic Shape Changes in Supported Copper Nanocrystals. *Science* **2002**, *295*, 2053–2055.

(259) De Jonge, N.; Ross, F. M. Electron Microscopy of Specimens in Liquid. *Nat. Nanotechnol.* **2011**, *6*, 695–704.

(260) Yuk, J. M.; Park, J.; Ercius, P.; Kim, K.; Hellebusch, D. J.; Crommie, M. F.; Lee, J. Y.; Zettl, A.; Alivisatos, A. P. High-Resolution EM of Colloidal Nanocrystal Growth Using Graphene Liquid Cells. *Science* **2012**, *336*, 61–64.

(261) Liao, H.-G.; Cui, L.; Whitelam, S.; Zheng, H. Real-Time Imaging of Pt3Fe Nanorod Growth in Solution. *Science* **2012**, *336*, 1011–1014.

(262) Li, D.; Nielsen, M. H.; Lee, J. R. I.; Frandsen, C.; Banfield, J. F.; De Yoreo, J. J. Direction-Specific Interactions Control Crystal Growth by Oriented Attachment. *Science* **2012**, *336*, 1014–1018.

(263) Gorbunov, A.; Jost, O.; Pompe, W.; Graff, A. Solid–liquid–solid Growth Mechanism of Single-Wall Carbon Nanotubes. *Carbon* **2002**, *40*, 113–118.

(264) Pohl, D.; Schäffel, F.; Rümmeli, M.; Mohn, E.; Täschner, C.; Schultz, L.; Kisielowski, C.; Rellinghaus, B. Understanding the Metal-Carbon Interface in FePt Catalyzed Carbon Nanotubes. *Phys. Rev. Lett.* **2011**, *107*, 185501.

(265) Salgado, J.; Antolini, E.; Gonzalez, E. Carbon Supported PtCo Electrocatalyst Prepared by the Formic Acid Method for the Oxygen Reduction Reaction in Polymer Electrolyte Fuel Cells. *J. Power Sources* **2005**, *141*, 13–18.

(266) Stamenkovic, V. R.; Mun, B. S.; Arenz, M.; Mayrhofer, K. J. J.; Lucas, C. A.; Wang, G.; Ross, P. N.; Markovic, N. M. Trends in Electrocatalysis on

Extended and Nanoscale Pt-Bimetallic Alloy Surfaces. *Nat. Mater.* **2007**, *6*, 241–247.

(267) Giannozzi, P.; Baroni, S.; Bonini, N.; Calandra, M.; Car, R.; Cavazzoni, C.; Ceresoli, D.; Chiarotti, G. L.; Cococcioni, M.; Dabo, I.; *et al.* QUANTUM ESPRESSO: A Modular and Open-Source Software Project for Quantum Simulations of Materials. *J. Physics. Condens. Matter* **2009**, *21*, 395502.

(268) Wang, Z. L. Transmission Electron Microscopy of Shape-Controlled Nanocrystals and Their Assemblies. *J. Phys. Chem. B* **2000**, *104*, 1153–1175.

(269) Warner, J. H.; Rümmeli, M. H.; Gemming, T.; Büchner, B.; Briggs, G. A. D. Direct Imaging of Rotational Stacking Faults in Few Layer Graphene. *Nano Lett.* **2009**, *9*, 102–106.

(270) Singh, A.; Dickinson, C.; Ryan, K. M. An Insight into the 3D Architecture and Quasicrystal Symmetry of Multilayer Nanorod Assemblies from Moiré Interference Patterns. *ACS Nano* **2012**, *6*, 3339–3345.

(271) Zhang, Q.; Liu, S.-J.; Yu, S.-H. Recent Advances in Oriented Attachment Growth and Synthesis of Functional Materials: Concept, Evidence, Mechanism, and Future. *J. Mater. Chem.* **2009**, *19*, 191–207.

(272) Zhang, J.; Huang, F.; Lin, Z. Progress of Nanocrystalline Growth Kinetics Based on Oriented Attachment. *Nanoscale* **2010**, *2*, 18–34.

(273) Chen, C. L.; Lee, J.-G.; Arakawa, K.; Mori, H. Quantitative Analysis on Size Dependence of Eutectic Temperature of Alloy Nanoparticles in the Ag–Pb System. *Appl. Phys. Lett.* **2011**, *98*, 083108.

(274) Wang, Z. L.; Petroski, J. M.; Green, T. C.; El-Sayed, M. A. Shape Transformation and Surface Melting of Cubic and Tetrahedral Platinum Nanocrystals. *J. Phys. Chem. B* **1998**, *102*, 6145–6151.

(275) Lee, J.; Mori, H.; Yasuda, H. Alloy Phase Formation in Nanometer-Sized Particles in the In-Sn System. *Phys. Rev. B* **2002**, *65*, 132106.

(276) Jesser, W.; Shneck, R.; Gile, W. Solid-Liquid Equilibria in Nanoparticles of Pb-Bi Alloys. *Phys. Rev. B* **2004**, *69*, 144121.

(277) Buffat, P.; Borel, J.-P. Size Effect on the Melting Temperature of Gold Particles. *Phys. Rev. A* **1976**, *13*, 2287–2298.

(278) Chen, C. L.; Lee, J.-G.; Arakawa, K.; Mori, H. Comparative Study on Size Dependence of Melting Temperatures of Pure Metal and Alloy Nanoparticles. *Appl. Phys. Lett.* **2011**, *99*, 013108.

(279) Chen, X.; Li, H.; Ding, X.; Rogl, P.; Podloucky, P. A New Thermodynamic Calculation Method for Binary Alloys: Part I: Statistical Calculation of Excess Functions. *J. Mater. Sci. Technol.* **2002**, *18*, 237–241.

(280) Penn, R. L.; Banfield, J. F. Imperfect Oriented Attachment: Dislocation Generation in Defect-Free Nanocrystals. *Science* **1998**, *281*, 969–971.

(281) Gao, J.; Yip, J.; Zhao, J.; Yakobson, B. I.; Ding, F. Graphene Nucleation on Transition Metal Surface: Structure Transformation and Role of the Metal Step Edge. *J. Am. Chem. Soc.* **2011**, *133*, 5009–5015.

(282) Shu, H.; Chen, X.; Tao, X.; Ding, F. Edge Structural Stability and Kinetics of Graphene Chemical Vapor Deposition Growth. *ACS Nano* **2012**, *6*, 3243–3250.

(283) Chen, H.; Zhu, W.; Zhang, Z. Contrasting Behavior of Carbon Nucleation in the Initial Stages of Graphene Epitaxial Growth on Stepped Metal Surfaces. *Phys. Rev. Lett.* **2010**, *104*, 186101.

(284) Saadi, S.; Abild-Pedersen, F.; Helveg, S.; Sehested, J.; Hinnemann, B.; Appel, C. C.; Nørskov, J. K. On the Role of Metal Step-Edges in Graphene Growth. *J. Phys. Chem. C* **2010**, *114*, 11221–11227.